

## Small scale very high speed slotless permanent magnet motors

Présentée le 10 janvier 2020

à la Faculté des sciences et techniques de l'ingénieur  
Laboratoire d'actionneurs intégrés  
Programme doctoral en robotique, contrôle et systèmes intelligents

pour l'obtention du grade de Docteur ès Sciences

par

**Guillaume Paul-André BURNAND**

Acceptée sur proposition du jury

Dr R. Boulic, président du jury  
Prof. Y. Perriard, directeur de thèse  
Prof. E. Lomonova, rapporteuse  
Dr L. Burdet, rapporteur  
Prof. A. Skrivervik, rapporteuse



À mes parents et à la mémoire de mon père.





# Remerciements

Par ces quelques lignes, je tiens à remercier celles et ceux qui ont contribué, de près ou de loin, à la réussite de ma thèse.

En premier lieu, je souhaite naturellement remercier le Professeur Yves Perriard, qui m'a offert l'opportunité d'effectuer ma thèse au Laboratoire d'Actionneurs Intégrés. Un immense merci Yves pour ta confiance et tes nombreux conseils. Un grand merci également à Yoan et Douglas qui m'ont suivi l'un après l'autre durant ces presque 4 années de travail. Je ne saurais oublier les seniors du laboratoire, Paolo, Alexis, Christian et Magda, sans qui les choses ne fonctionneraient pas aussi sereinement. Merci aux collègues, Dan, Daniel, Xinchang, Cécile, Jasha, Florian, Jonathan, Louis, Pato, Raphaël, Sean aka S-Dawg, Morgan, Valentin, David, Adrien, Xiaotao, Francesco, Camilo, Pooneh, Sofia et Trung, ainsi que tous les stagiaires et les étudiants, pour votre soutien, nos échanges et la bonne humeur du labo.

Je remercie les membres du jury d'avoir accepté l'invitation et d'avoir donné de leur temps pour l'évaluation et les corrections qu'ils ont apportées.

Je tiens tout particulièrement à remercier la société Electromag SA, son directeur Monsieur Vincent Comte et son responsable de la R&D le Dr Luc Burdet, ainsi que toute l'équipe qui s'est investie dans le projet. Il s'agit de Fabien, Eugène, Alix et Martin. Notre fructueuse collaboration a donné naissance à cette thèse et a très largement contribué à sa réussite. En effet, la société a notamment procédé à la fabrication des prototypes de moteur.

Enfin, je remercie du fond du cœur ma famille et mes amis pour leurs soutiens et leurs encouragements. Merci également à Wendy pour la relecture scrupuleuse de la thèse. Finalement, un immense merci à toi Gaëlle, mon amour, pour m'avoir soutenu, mais aussi avoir partagé les bons moments.

Merci à tous!

*Neuchâtel, le 9 décembre 2019*

Guillaume Burnand



# Résumé

Ce travail de recherche a été initié par un projet industriel visant à modéliser et fabriquer un moteur de petite dimension à très haute vitesse. Les moteurs électriques à très haute vitesse offrent l'avantage de réduire la taille d'un système. En effet, à puissance mécanique égale, le fait d'augmenter la vitesse de rotation permet de diminuer le couple électromagnétique et par conséquent la taille du moteur. Lorsqu'un système possède déjà des dispositifs fonctionnant à très haute vitesse, il devient intéressant de les combiner avec une machine électrique. L'utilisation d'entraînement direct à très haute vitesse permet de supprimer les transmissions mécaniques, réduisant la maintenance et les coûts. De pair avec la très haute vitesse, la réduction en taille des moteurs est au bénéfice d'applications où le poids et l'encombrement sont des facteurs limitants. Utilisés comme outils à main, ces moteurs offrent des solutions pour l'oto-rhino-laryngologie ou la chirurgie dentaire.

Grâce à leur liberté de forme, les bobinages dans l'entrefer possèdent d'importantes capacités d'amélioration. Avec les nouvelles technologies de fabrication, la conception de ces bobinages peut être repensée. Les performances des moteurs électriques peuvent donc être améliorées en adoptant de nouvelles formes et topologies.

La thèse est ainsi orientée selon deux axes : elle donne d'une part des modèles multiphysiques qui servent au dimensionnement et à l'optimisation de moteurs synchrones à aimants permanent à très haute vitesse et de petites dimensions ; d'autre part elle propose une solution innovante pour une nouvelle topologie de bobinage dans l'entrefer, augmentant significativement les performances des moteurs électriques.

De par leur nature, les moteurs à très haute vitesse sont poussés à l'extrême : ils subissent de fortes contraintes mécaniques dans les matériaux du rotor et les paliers, sont sujets aux vitesses critiques, fonctionnent souvent à haute température et dans des environnements difficiles et, à cause des hautes fréquences électriques, sont le siège d'importantes pertes fer et cuivre. De plus, leur dimensionnement dépend fortement de leur application et n'est pas aisé à généraliser. En conséquence, ces moteurs requièrent des modèles multiphysiques robustes et fiables. Dans cette thèse, une série complète de modèles mécaniques et électromagnétiques sont présentés. Vis-à-vis des modèles numériques, les modèles analytiques apportent une meilleure compréhension des phénomènes physiques intrinsèques aux moteurs et nécessitent moins de temps de calcul lors de l'optimisation.

En particulier, un modèle analytique 3D est développé pour le calcul des contraintes mécaniques dans le rotor, qui différencie les rotors en forme de cylindre ou de disque et les rotors

---

à aimants creux ou pleins, avec considération des effets thermiques. De même, un modèle analytique est présenté pour le calcul des pertes par courants de Foucault induits dans un bobinage à conducteurs rectangulaires par le champ magnétique de l'aimant.

Tous les modèles analytiques précédemment cités sont employés dans un contexte de dimensionnement et d'optimisation de moteurs sans dents à aimants permanent à très haute vitesse et de petites dimensions avec roulement à billes. À l'aide d'un algorithme d'optimisation approprié, de contraintes sur les dimensions maximales et un point de fonctionnement donné, des dimensionnements optimaux sont obtenus pour différentes vitesses de rotation. La contribution originale vient de la comparaison des fils de Litz et des fils rectangulaires ainsi que des rotors à aimant plein et creux utilisés dans les moteurs sans dents à très haute vitesse et de petites dimensions.

La validation expérimentale des modèles se fait grâce à un prototype de moteur de 400 krpm et 12.7 mm de diamètre qui a été testé jusqu'à 475 krpm. Le prototype fabriqué permet également de démontrer la faisabilité de construction des moteurs de petite dimension. Une méthode expérimentale astucieuse est mise en place dans le but de séparer les différentes composantes de pertes dues à la rotation du rotor. Ainsi, chaque modèle est obtenu et/ou validé séparément.

Finalement, ce travail de recherche met l'accent sur la modélisation et l'optimisation d'une nouvelle topologie de bobinage dans l'entrefer. En remettant en question les méthodes traditionnelles de fabrication des bobinages, il est démontré que l'utilisation de fils à section non constante et une forme optimisée des spires mènent à une amélioration significative des performances du bobinage, et donc du moteur. Un prototype du nouveau bobinage est réalisé et permet de valider le modèle théorique.

**Mots clefs :** *Moteurs synchrones à aimants permanents sans dents, Moteurs à très haute vitesse, Moteurs de petites dimensions, Modélisation analytique multiphysique, Dimensionnement, Optimisation, Bobinages dans l'entrefer, Validation expérimentale*

# Abstract

This research work has been triggered by an industrial project aimed at modelling and manufacturing of a small scale very high speed motor. Very high speed electrical motors offer the main advantage of reducing the size of a system. Indeed, at constant output mechanical power, increasing the rotational speed enables to decrease the electromagnetic torque, hence the size of the motor. When a system already possesses very high speed devices, it becomes attractive to combine them with an electrical machine. To get rid of mechanical drives, direct drives with very high speed electrical motors entail a reduction of the maintenance and the costs. Combined with very high speed, the miniaturisation of motors benefits limited weight and space applications. Used as hand tools, they provide solutions for otorhinolaryngology or dental surgery.

Because they can be freely arranged in the airgap, slotless windings represent a substantial capacity for enhancement. Thanks to new manufacturing technologies, the design of windings can be rethought. Different shapes and topologies can be embraced leading to improved performances for electrical motors.

The aim of this thesis is consequently twofold: to give multiphysics models enabling the design and the optimisation of small scale very high speed permanent magnet synchronous motors, and to propose an innovative solution for a new type of slotless winding topology entailing the performances of electrical motors.

By essence, very high speed motors are pushed to their limits: they experience high mechanical stresses in the materials of the rotor and the bearings, are subject to critical speeds, operate sometimes at high temperature and harsh environments and, due to high electrical frequencies, produce significant iron and winding losses. Furthermore, their design strongly depends on the application and is arduous to generalise. As a result, robust and reliable multiphysics models have to be established. In this thesis, a very complete set of both mechanical and electromagnetic analytical models is presented. Analytical models are preferred to numerical models as they bring more insight in understanding physical phenomena occurring in the motors and require less computational effort for optimisation.

In particular, a 3D analytical rotor mechanical stresses model distinguishing between cylinder and disc shaped rotors and hollow and solid magnet rotors with the consideration of thermal stresses is developed. Similarly, an analytical model for the computation of induced eddy current losses by the magnetic field of the permanent magnet in rectangular conductors is devised.

---

All the aforementioned analytical models are used in the context of the design and the optimisation of small scale very high speed slotless permanent magnet motors with ball bearings. With an appropriate optimisation algorithm, fixed constraints on the maximal size and the operating point, optimal designs are obtained for several rotational speeds. Particularly, an original contribution comes from the comparison of Litz-wire and rectangular wires as well as hollow and solid magnet rotors used in small scale very high speed slotless motors.

In order to experimentally validate the models, a 400 krpm-12.7 mm diameter prototype is manufactured and tested up to 475 krpm. In addition, it demonstrates the feasibility of miniaturised very high speed motors. An astute experimental method is implemented in order to separate the losses components related to the rotation of the rotor. Therefore, every model can be obtained and/or validated independently.

Finally, the research work emphasis on the modelling and the optimisation of a novel slotless winding topology. By challenging the traditional way of manufacturing windings, the use of nonconstant wire sections and an optimised shape enables the performances of the winding, and thereby the motor, to be significantly improved. A prototype of the new winding topology is manufactured and leads to the validation of the theoretical model.

**Keywords:** *Slotless permanent magnet synchronous motors, Very high speed motors, Small scale motors, Multiphysics analytical modelling, Design, Optimisation, Slotless windings, Experimental validation*

# Contents

<b>Remerciements</b>	<b>i</b>
<b>Résumé</b>	<b>iii</b>
<b>Abstract</b>	<b>v</b>
<b>List of figures</b>	<b>xi</b>
<b>List of tables</b>	<b>xv</b>
<b>1 Introduction</b>	<b>1</b>
1.1 Background and motivation . . . . .	1
1.1.1 The need for very high speed . . . . .	1
1.1.2 The need for miniaturisation . . . . .	2
1.1.3 Enhancement of slotless windings . . . . .	3
1.1.4 Context of the thesis . . . . .	3
1.2 Outline of the thesis . . . . .	3
<b>2 State of the art</b>	<b>7</b>
2.1 Introduction . . . . .	8
2.2 Very high speed electrical machines review . . . . .	9
2.2.1 Type of machine . . . . .	10
2.2.2 Bearing technology . . . . .	10
2.2.3 Applications . . . . .	11
2.2.4 Comparative study . . . . .	12
2.3 Losses . . . . .	13
2.3.1 Location and classification . . . . .	13
2.3.2 Power balance . . . . .	13
2.3.3 Losses specific to very high speed . . . . .	15
2.4 Limitation and design . . . . .	16
2.5 Windings . . . . .	17
2.5.1 Slotless windings . . . . .	17
2.5.2 Potential for improvement . . . . .	17
2.6 Previous academic works . . . . .	19
2.7 Conclusion . . . . .	19
	vii

<b>3</b>	<b>Mechanical modelling</b>	<b>21</b>
3.1	Introduction . . . . .	22
3.2	Rotor stresses . . . . .	23
3.2.1	Geometry and mechanical properties . . . . .	23
3.2.2	Stresses in the rotor . . . . .	25
3.2.3	Failure criterion . . . . .	28
3.2.4	Validation of the model . . . . .	30
3.2.5	Limitation of the model . . . . .	31
3.3	Modal analysis . . . . .	34
3.3.1	Vibration modes . . . . .	34
3.3.2	Critical speeds . . . . .	34
3.3.3	Equation of motion . . . . .	35
3.3.4	Computation of critical speeds . . . . .	35
3.4	Windage losses . . . . .	37
3.5	Ball bearing losses . . . . .	40
3.6	Conclusion . . . . .	40
<b>4</b>	<b>Electromagnetic modelling</b>	<b>41</b>
4.1	Introduction . . . . .	42
4.2	Geometry and electromagnetic properties . . . . .	43
4.3	Magnetic quantities . . . . .	44
4.3.1	Vector potential . . . . .	44
4.3.2	Magnetic flux density . . . . .	45
4.3.3	Magnetic flux linkage and back EMF voltage . . . . .	47
4.3.4	Electromagnetic torque . . . . .	48
4.3.5	Validation of the models . . . . .	48
4.4	Winding losses . . . . .	50
4.4.1	Component due to the current . . . . .	51
4.4.2	Component due to the permanent magnet for round wires . . . . .	51
4.4.3	Component due to the permanent magnet for rectangular wires . . . . .	53
4.5	Iron losses . . . . .	57
4.6	Rotor losses . . . . .	58
4.7	Conclusion . . . . .	59
<b>5</b>	<b>Design and optimisation</b>	<b>61</b>
5.1	Introduction . . . . .	62
5.2	Models and design . . . . .	63
5.2.1	Mechanical models . . . . .	63
5.2.2	Electromagnetic models . . . . .	63
5.2.3	Power balance . . . . .	67
5.3	Optimisation framework . . . . .	67
5.3.1	Objective function . . . . .	67
5.3.2	Design variables . . . . .	68



5.3.3	Constraints and fixed parameters . . . . .	68
5.3.4	Optimisation algorithm . . . . .	70
5.4	Comparison of conductors at several rotational speeds . . . . .	70
5.4.1	Fixed parameters specific to the case study . . . . .	70
5.4.2	Results . . . . .	70
5.5	Comparison of solid and hollow magnet rotors . . . . .	73
5.5.1	Results . . . . .	73
5.6	Synthesis . . . . .	75
5.7	Conclusion . . . . .	76
<b>6</b>	<b>Experimental validation</b>	<b>77</b>
6.1	Introduction . . . . .	78
6.2	Construction of the prototype . . . . .	79
6.3	Measurements . . . . .	81
6.3.1	Resistance . . . . .	81
6.3.2	Inductance . . . . .	81
6.3.3	No-load losses . . . . .	82
6.3.4	Back EMF and torque constant . . . . .	82
6.3.5	Critical speeds . . . . .	83
6.4	Measurement technique to separate the losses . . . . .	84
6.4.1	Setup and tests . . . . .	84
6.4.2	Results . . . . .	88
6.4.3	Power balance . . . . .	90
6.5	Conclusion . . . . .	91
<b>7</b>	<b>Towards a new winding topology</b>	<b>93</b>
7.1	Introduction . . . . .	95
7.2	Winding topology . . . . .	96
7.2.1	Preliminary considerations . . . . .	96
7.2.2	Geometry and parameters . . . . .	97
7.3	Modelling . . . . .	98
7.3.1	Torque constant . . . . .	98
7.3.2	Back EMF constant . . . . .	99
7.3.3	Resistance . . . . .	100
7.3.4	Motor constant . . . . .	101
7.3.5	Winding factor . . . . .	102
7.4	Optimisation . . . . .	103
7.4.1	Objective function . . . . .	103
7.4.2	Optimisation framework . . . . .	103
7.4.3	Results . . . . .	103
7.4.4	3D FEM validation . . . . .	106
7.5	Prototype and measurements . . . . .	107
7.5.1	Realisation of the prototype . . . . .	107

## Contents

---

7.5.2	Experimental validation . . . . .	108
7.6	Implementation in rotating and linear machines . . . . .	110
7.7	Conclusion . . . . .	111
<b>8</b>	<b>Conclusion and outlook</b>	<b>113</b>
8.1	Original contributions . . . . .	114
8.2	Outlook . . . . .	116
<b>A</b>	<b>Kelvin functions</b>	<b>117</b>
A.1	Kelvin functions of the first kind . . . . .	117
A.2	Derivatives of Kelvin functions of the first kind . . . . .	117
<b>B</b>	<b>Calculation of the gradient of the potential</b>	<b>119</b>
<b>C</b>	<b>Drawing of the laser-cutting coil</b>	<b>121</b>
	<b>Nomenclature</b>	<b>123</b>
	<b>Bibliography</b>	<b>145</b>
	<b>Curriculum Vitae</b>	<b>147</b>

# List of Figures

1.1	Electrically assisted turbocharger for automotive applications [1]. . . . .	2
1.2	Electrical hand tool requiring a small scale electrical motor [2]. . . . .	2
1.3	The 400 krpm 40 W 12.7 mm diameter 28 mm length motor prototype. . . . .	4
1.4	The novel slotless winding topology. . . . .	5
2.1	Nominal rotational speed with respect to nominal mechanical power for high speed and very high speed electrical machines in terms of their types. . . . .	9
2.2	Nominal rotational speed with respect to nominal mechanical power for high speed and very high speed electrical machines in terms of their bearing technologies. . . . .	10
2.3	Nominal rotational speed with respect to nominal mechanical power for high speed and very high speed electrical machines in terms of their applications. . . . .	12
2.4	Power diagram (motor) and locations of the losses in a machine (inspired from [3]).	14
2.5	Most common types of slotless windings from [4]. . . . .	17
2.6	Illustrations of the possibilities to improve windings. . . . .	18
3.1	Cross-section giving the geometry and the dimensions of the rotor stresses model.	23
3.2	Meshed ANSYS 3D FEM model for the computation of rotor stresses. . . . .	30
3.3	Validation of the stresses components in the rotor. . . . .	32
3.4	Von Mises stress at standstill in ANSYS (scale in MPa). . . . .	33
3.5	Validation of the von Mises stress in the rotor. . . . .	33
3.6	Representation of the vibration modes. . . . .	34
3.7	Modeling of the ball bearings and the rotor in ANSYS for the computation of critical speeds. . . . .	35
3.8	Campbell diagram obtained by ANSYS 3D FEM. . . . .	36
3.9	Critical speeds computed by ANSYS 3D FEM. . . . .	36
3.10	Cross-section giving the geometry for the windage losses model. . . . .	37
3.11	Windage losses for the prototype according to Mack's model. . . . .	39
4.1	Cross-section giving the geometry and the dimensions of electromagnetic models. The rotor is made of a one pole pair ( $p = 1$ ) diametrically magnetised cylindrical permanent magnet and the stator is slotless. . . . .	43
4.2	Equipotential lines of the axial component of the vector potential in the airgap. The mechanical angle of the rotor is worth $\frac{\pi}{2}$ . . . . .	45

## List of Figures

---

4.3	Isolines of the radial component of the magnetic flux density in the airgap. The mechanical angle of the rotor is worth $\frac{\pi}{2}$ . . . . .	46
4.4	Isolines of the tangential component of the magnetic flux density in the airgap. The mechanical angle of the rotor is worth $\frac{\pi}{2}$ . . . . .	46
4.5	3D FEM model with non-mesh coils in Altair Flux. . . . .	48
4.6	Comparison of the magnetic flux in one coil between analytical and 3D FEM models. . . . .	49
4.7	Comparison of the electromagnetic torque in one coil between analytical and 3D FEM models. . . . .	49
4.8	Skin depth of copper versus typical frequencies encountered in very high speed machines. . . . .	51
4.9	Cross-section giving the geometry and the dimensions of the model for the computation of eddy current losses in the winding induced by the rotation of the PM. The PM has one pole pair and is diametrically magnetised. . . . .	53
4.10	Induced current density in the wire with respect to several values of the angle of the rotor at 400 krpm. . . . .	55
4.11	Transient 2D FEM model highlighting the induced current density in half a coil of 29 turns due to the rotation of the PM (Altair Flux). . . . .	56
4.12	Comparison of the eddy current losses induced in the winding by the rotation of the PM between analytical and 2D FEM models. . . . .	56
5.1	Sketch of a coil. . . . .	64
5.2	Normalised dimensions of the motors. . . . .	72
5.3	Distribution of losses in the motors. . . . .	73
6.1	Pictures of the VHS prototype employed for the experimental validation of the models. . . . .	79
6.2	Measurements of the phase-to-phase inductance and resistance taking into account the power supply cable. . . . .	81
6.3	No-load losses with respect to the rotational speed up to 475 krpm. . . . .	82
6.4	Back EMF voltage over time at 250 krpm on the oscilloscope. . . . .	83
6.5	RMS back EMF voltage with respect to the rotational speed. . . . .	83
6.6	Modulus of the unbalance of the shaft with respect to the rotational speed. . . .	84
6.7	Rotational speed (deceleration) over time for the 4 tests. . . . .	85
6.8	Vacuum chamber ( $P < 1$ mbar). . . . .	85
6.9	Measurement of ball bearing losses (Test 3). . . . .	86
6.10	Coupling bench. . . . .	86
6.11	Measurement of iron losses due to the field of the PM (Test 4). . . . .	87
6.12	Measurements of losses components due to the rotation of the rotor. . . . .	89
6.13	Sum of all the individual losses models compared to the measurements (Test 1) of all losses due to the rotation of the rotor. . . . .	90
6.14	Losses due to the stator currents. . . . .	91

7.1	A 3-phase 6-coil slotless winding used as comparison. . . . .	96
7.2	The new slotless winding topology. . . . .	97
7.3	Results after optimisation of the new windings. Red circles highlight the difference between the heights of the wire at the location of end-windings. . . . .	104
7.4	Resistance for one coil with respect to the axial distance $z_{\text{bend}}$ . . . . .	106
7.5	Motor constant with respect to the axial distance $z_{\text{bend}}$ . . . . .	106
7.6	3D FEM model of the new winding topology with a non-mesh coil in Altair Flux. . . . .	107
7.7	Comparison of the electromagnetic torque in one coil between analytical and 3D FEM models. . . . .	107
7.8	Manufacturing of the new winding prototype. . . . .	108
7.9	Experimental validation of the coil torque constant for one coil $k'_t$ with respect to the rotational speed. . . . .	109
7.10	Implementation of the new winding topology. . . . .	110



## List of Tables

2.1	Characteristics of existing prototypes and commercialised machines close to the targeted region. All are PMSM and have ball bearings. . . . .	12
3.1	Plane strain and plane stress conditions. . . . .	25
3.2	Simulation parameters used for the validation of the rotor stresses model. . . .	30
5.1	Fixed parameters and constraints for the optimisation. . . . .	69
5.2	Parameters for the genetic algorithm. . . . .	69
5.3	Optimisation results of motors with Litz-wire or rectangular wire at several rotational speeds. . . . .	71
5.4	Optimisation results of motors with hollow or solid magnet rotors at several rotational speeds. . . . .	74
6.1	Parameters and dimensions of the VHS prototype. . . . .	80
6.2	Constants for the model of ball bearing and iron losses. . . . .	90
7.1	Parameters and dimensions of the motor used for the theoretical and experimental validation of the new winding topology model. . . . .	104
7.2	Results of the optimisation. . . . .	105
7.3	Average wire widths measurements of the new winding prototype. . . . .	109





# 1 Introduction

## 1.1 Background and motivation

### 1.1.1 The need for very high speed

One of the purposes of increasing speed is that, for a given power, the size of the machine can be reduced, increasing the power density. This is consistent with the fact that the diameter of the rotor has to diminish while the rotational speed increases to withstand centrifugal forces.

Intrinsically, some applications require very high rotational speeds. For instance, micro milling and micro drilling need rotational speeds of several hundreds of thousands revolutions per minute. Indeed, the smaller the machining tool, the higher the rotational speed to maintain an appropriate cutting speed in a given material. One can also mention beam choppers used in optical systems to modulate light beams at frequencies in the range of kHz [5].

When a system already possesses very high speed devices, it becomes attractive to combine them with an electrical machine. In the case of automotive, a very high speed electrical machine can be mounted on the shaft of a turbocharger as pictured in Figure 1.1. As a result, the electrical machine acts as a motor when the automotive lacks power (at low speed), and as a generator at high engine load when there is too much pressure in the exhaust [6]. This becomes an electrically assisted turbocharger.

One of the solutions to store mechanical energy is the use of flywheels [7]. Given that the kinetic energy contained in a rotating inertia scales with the square of the rotational speed, it is interesting to increase the latter. Flywheels can be coupled to electrical machines and used in many applications such as electric cars or satellites. Still in the context of energy, very high speed electrical machines can also be used for portable power generation when connected to a micro gas turbine to replace batteries [8].

Another benefit of very high speed machines is to eliminate gear boxes by using direct drive systems. This leads to an improved efficiency and a better reliability [6]. This also simplifies the construction of the system and, as a result, reduces the costs [9].

### 1.1.2 The need for miniaturisation

As previously mentioned, the reduction of the size of a machine is consistent with the very high speeds for mechanical reasons. Small scale very high speed electrical machines find their place in low weight applications such as in aircraft [10]. Used as hand tools, they also facilitate access to narrow spaces for otorhinolaryngology or dental surgery, as illustrated in Figure 1.2.

Lower dimensions also mean lower material costs. Nowadays, there is a clear tendency to decrease the size of motors and increase the power density while keeping the efficiency as high as possible. However, there is currently no available solutions for small scale very high speed electrical motors.



Figure 1.1 – Electrically assisted turbocharger for automotive applications [1].



Figure 1.2 – Electrical hand tool requiring a small scale electrical motor [2].

### 1.1.3 Enhancement of slotless windings

Recent developments in slotless windings have been performed these past years. Due to the many possible shapes and topologies they can embrace, slotless windings represent a substantial potential for improvement. Indeed, windings are a key part of electrical machines and their enhancement directly affects the performances of electrical machines. Thanks to nonconstant wire sections and an optimised shape, it can be demonstrated that the motor constant is significantly increased compared to traditional windings. With the help of constantly improving additive manufacturing technologies, new means of designing and manufacturing electrical machines now seem possible.

### 1.1.4 Context of the thesis

The thesis ensues from the CTI/KTI project no 18684.1 PFIW IW in collaboration with a Swiss industrial partner.

## 1.2 Outline of the thesis

The thesis is structured as follows:

- *Chapter 2 - State of the art*

The chapter covers the current available solutions for the study and the development of very high speed electrical machines, giving examples of applications. Through a review of 49 very high speed electrical machines and a discussion about specific losses related with very high speed, conclusions can be drawn and choices can be made, laying the background of the thesis. The possibilities of enhancement of slotless windings, which have a direct impact on the performances of the machines, are also part of the chapter. Indeed, recent research on the use of nonconstant wire sections and optimised shape, joined with new manufacturing techniques, indicate significant opportunities of improvement for slotless windings.

- *Chapter 3 - Mechanical modelling*

Because of very high rotational speeds, mechanical modelling is inherent to the design of very high speed applications. The rotor and the bearings are amongst the most critical parts to design. The chapter is devoted to the modelling of mechanical stresses in the rotor (to avoid failure due to centrifugal forces), critical speeds (to avoid vibration) and mechanical losses. The latter can reach a significant amount of the total losses and thus require reliable and accurate models. This is particularly true for windage losses models, as many of them exist and all give different estimations.

- *Chapter 4 - Electromagnetic modelling*

The chapter deals with the electromagnetic modelling of slotless permanent magnet machines. From the determination of the vector potential in the airgap, further relevant quantities can be derived. One can cite the magnetic flux density in the airgap, the back EMF voltage or the electromagnetic torque. An emphasis on the losses produced by the electrical stator currents and the magnetic field of the permanent magnet is made. In particular, an innovative analytical model for the computation of induced eddy current losses by the field of the permanent magnet in rectangular conductors is presented.

- *Chapter 5 - Design and optimisation*

The chapter tackles the design and the multiphysics optimisation of small scale motors. It combines the models established in Chapters 3 and 4, leading to optimal designs under given constraints on the size and the operating point. The original contribution comes from the comparison of Litz-wire and rectangular wires, as well as hollow and solid magnet rotors in very high speed slotless permanent magnet motors.

- *Chapter 6 - Experimental validation*

Most of the models obtained so far are experimentally validated in the chapter. To do so, a 400 krpm 40 W 12.7 mm diameter 28 mm length motor prototype is manufactured as pictured in Figure 1.3. An astute measurement technique is developed and enables the separation of losses components related to the rotation of the rotor. Consequently, every model can be obtained and/or validated independently. Notably, the analytical model for the computation of induced eddy current losses by the field of the permanent magnet in rectangular conductors is validated. Additionally, an existing empirical windage losses model for small scale motors is also validated.

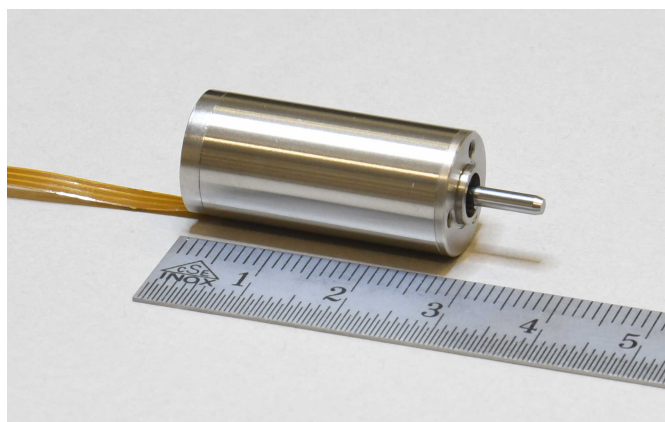


Figure 1.3 – The 400 krpm 40 W 12.7 mm diameter 28 mm length motor prototype.

- *Chapter 7 - Towards a new winding topology*

The chapter is dedicated to the study, the modelling and the optimisation of a novel slotless winding topology. Thanks to the use of nonconstant wire sections and an optimised shape, the performances of the winding, and consequently the motor, can be significantly increased. In addition to the theoretical validation made by 3D FEM, a prototype of the winding is realised for the experimental validation, as illustrated in Figure 1.4.

- *Chapter 8 - Conclusion and perspectives*

Finally, the chapter summarises the main contributions of the thesis and suggests perspectives for further research in the domain of very high speed electrical machines and slotless windings.

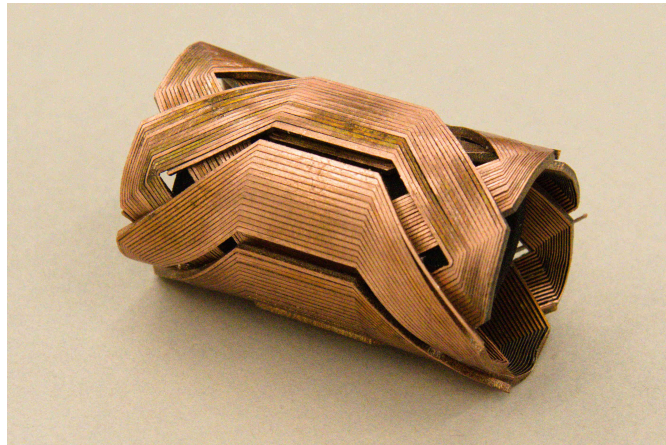


Figure 1.4 – The novel slotless winding topology.



## 2 State of the art

### Contents

---

<b>2.1 Introduction . . . . .</b>	<b>8</b>
<b>2.2 Very high speed electrical machines review . . . . .</b>	<b>9</b>
2.2.1 Type of machine . . . . .	10
2.2.2 Bearing technology . . . . .	10
2.2.3 Applications . . . . .	11
2.2.4 Comparative study . . . . .	12
<b>2.3 Losses . . . . .</b>	<b>13</b>
2.3.1 Location and classification . . . . .	13
2.3.2 Power balance . . . . .	13
2.3.3 Losses specific to very high speed . . . . .	15
<b>2.4 Limitation and design . . . . .</b>	<b>16</b>
<b>2.5 Windings . . . . .</b>	<b>17</b>
2.5.1 Slotless windings . . . . .	17
2.5.2 Potential for improvement . . . . .	17
<b>2.6 Previous academic works . . . . .</b>	<b>19</b>
<b>2.7 Conclusion . . . . .</b>	<b>19</b>

---

### 2.1 Introduction

The present state of the art enables laying the groundwork for the development of a 400 krpm 40 W 12.7 mm diameter 28 mm length electrical motor. It is later referred to as targeted motor. Applications of such a miniaturised machine can be medical, dental and machining hand tools, micro gas turbines, micro compressor or beam choppers among others. The review of the current technologies aims at better understanding the issues related to very high speed (VHS) machines. It presents a concise catalogue of the available solutions in order to reach the objectives and justifies the choices made with a scientific approach. It also sets the basis necessary to the reader to embark on the following chapters with ease.

Section 2.2 presents a review of very high speed electrical machines. Sorting the machines by their nominal speed versus nominal mechanical power in a graph enables to draw conclusions on the types of machine, the bearings and the applications that can be used. A definition of *very high speed* can be made out thanks to that classification. It also enables to make a comparative study on the nominal power, the nominal speed and the size of existing machines with the targeted motor.

The losses encountered in very high speed machines are covered in Section 2.3. They are one of the major concerns during the design. They result in energy dissipation that increases the temperature of the machine. Their sources and locations are detailed with the help of a power balance diagram. An emphasis on the losses specific to very high speed is then carried out and entails refining the earlier chosen solutions.

A discussion on the limitation and the design of VHS machines is proposed in Section 2.4. It puts forward some of the major constraints encountered by VHS machines: heating, mechanical stress in the rotor, critical speeds, bearings and electrical considerations. As will be realised further on, these machines are always pushed to their limits. Furthermore, they are multiphysical by nature and thus require a very complete and reliable modelling.

Section 2.5 covers the topic of slotless windings by presenting their advantages but also their distinct potential of improvement. Indeed, recent research has focused on the enhancement of such windings thanks to their freedom of shape and topology. In addition, the current development of additive manufacturing processes suggests that their manufacturing could be revised. Based on these considerations, the thesis proposes an innovative solution of slotless windings using nonconstant section wires and an optimised shape.

Finally, Section 2.6 lists the previous academic works upon which the present thesis is built.



## 2.2 Very high speed electrical machines review

From a general point of view, *electrical machines* are defined as devices able to transform energy from one form to another where at least one of them is electrical [11]. In particular, when the electrical energy is transformed into mechanical energy, electrical machines are classified as *motors*. And when the mechanical energy is transformed into electrical energy, electrical machines are classified as *generators*. In the thesis, the term *machines* refers to both electrical rotating motors and generators.

There are several ways to distinguish between high speed (HS) and very high speed (VHS) machines. The machines are not only defined by their rotational speed but also by their operating power [12]. Indeed, the rotational speed alone is not always sufficient. Sometimes, the tangential speed or tip speed at the outer radius of the rotor is used [9]. Nevertheless, large hydro generators can reach high tip speeds, and yet are not considered as high speed machines. A common rule is to set a numerical limit between HS and VHS machines [6]. The nominal speed-nominal mechanical power coordinate of the machines is plotted on a logarithmic graph (see Figure 2.1 for instance). Afterwards, a regression of the points is made and this line symbolises the limit between the high speed and the very high speed regions. This limit depends on the currently available technologies and, as a result, is not fixed [13].

Recent reviews have been undertaken on HS and VHS machines [6,9,14]. Most of the machines listed in Figures 2.1 to 2.3 are based on theses reviews and additional ones have been found in [15–22]. This gives a total of 49 commercialised machines and prototypes. Demonstrators, MEMS and machines that have not reached the targeted speed are not included in the figures. Despite the author's effort to draw up a complete and impartial inventory, it is possible that some relevant machines are missing.

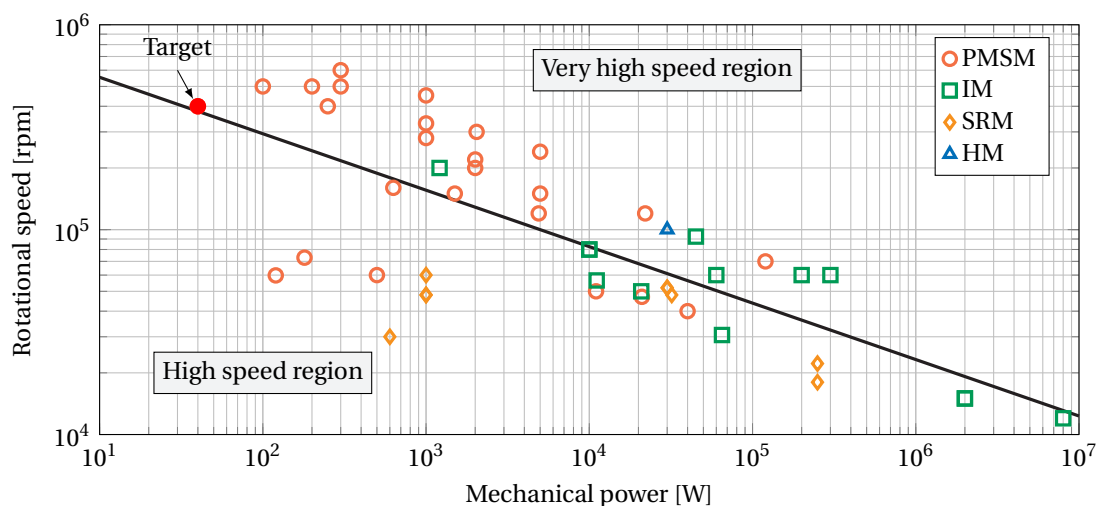


Figure 2.1 – Nominal rotational speed with respect to nominal mechanical power for high speed and very high speed electrical machines in terms of their types.

### 2.2.1 Type of machine

Figure 2.1 lists the machines in terms of their types: permanent magnet synchronous machines (PMSM), induction machines (IM), switched reluctance machines (SRM) and homopolar machines (HM). The machines running under 10 krpm are not represented and it can be mentioned that a broad majority of these are field excitation synchronous machines for power generation [9].

It should be noted that above a rotational speed of 100 krpm, the broad majority is PMSM. When the rotational speed increases, the diameter of the rotor has to decrease to withstand centrifugal forces. By reducing the size of permanent magnet machines, the magnetic flux density remains unchanged [11]. Conversely, in an electrically excited machine (IM, SRM or HM), the magnetic field decreases with the size, because the nominal current scales proportionally with the size [10]. In addition, machines with permanent magnets (PMs) have a higher power density, which is essential for miniaturised solutions. Although an IM is reported at 200 krpm, these machines are preferred at lower speed but higher mechanical power. Homopolar machines are usually employed in flywheels [23]. In this case, it should be mentioned that the targeted motor needs permanent magnets.

### 2.2.2 Bearing technology

Figure 2.2 sorts the machines in terms of their bearing technologies. Again, above 100 krpm the majority of machines has ball bearings. There is a border at 10 kW that divides more or less ball and magnetic bearings. A few machines supported by air bearings and magnetic bearings are located close to the region of interest. Oil bearing machines are employed for heavy rotors and therefore, the mechanical power is much higher than the one of the targeted motor.

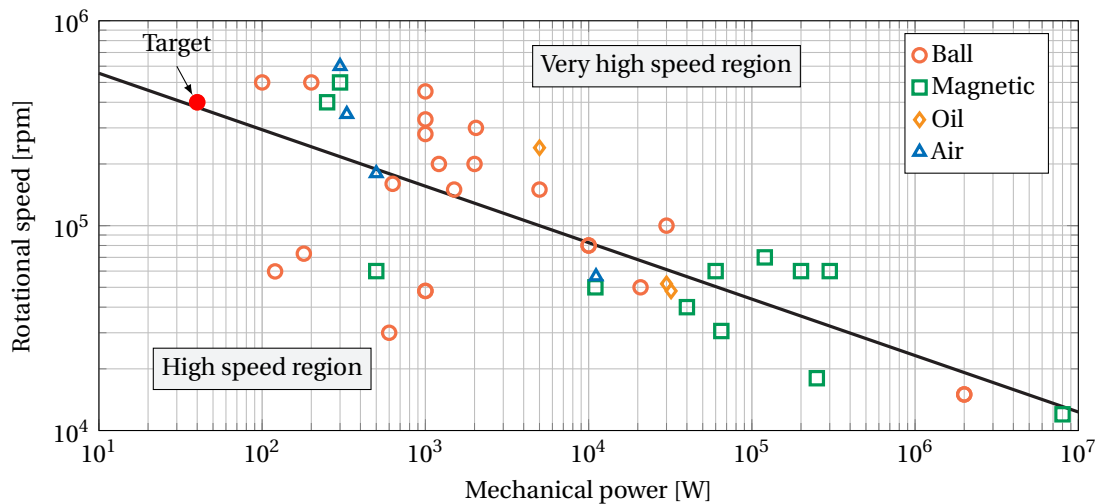


Figure 2.2 – Nominal rotational speed with respect to nominal mechanical power for high speed and very high speed electrical machines in terms of their bearing technologies.

Magnetic bearings are complex mechatronics systems including sensors, sophisticated control electronics and control algorithms [24, 25]. Although they can operate in vacuum, feature no wear and therefore have a long lifespan, such systems are generally space consuming. Owing to their complexity, magnetic bearings are almost exclusively used in niche applications.

Air bearings with grooves [26] or foils [27] have more or less the same advantages as magnetic bearings in the sense that they are contactless bearings. Again, they are very complex to design and expensive to manufacture. Furthermore, no commercial solutions small enough for the targeted machine are available.

The main advantage of ball bearings is possibly their simplicity in comparison with the other bearings presented above, in the sense that they are self-acting. They are compact, sturdy and cheap. On the other hand, they are penalised by their lifespan. It depends on the load, the temperature, the lubrication, the environment (vacuum, chemicals), the balancing of the rotor and the speed.

Various factors can limit the maximal admissible speed of ball bearings. It is worth mentioning the contact stresses between the ball and the raceways, the size of the balls, the temperature, the retainer or the lubricant. It is clear that reducing the size of the balls enables to increase the maximal speed, but it will also increase the noise and reduce the load capability [28].

Ceramic (hybrid) angular contact ball bearings are known to be the most appropriate for very high rotational speed [29, 30]. Nevertheless, a rotational speed of 500 krpm has been reported in [31] using radial ball bearings. Thus, the solution of ball bearings is selected.

### 2.2.3 Applications

Very high speed rotating machines are used in various applications [6–10, 23, 32]:

- pumps (vacuum), compressors (fuel cell) and fans,
- gas turbines,
- turbochargers (automotive),
- machine tools,
- hand tools and drills for dental and medical applications,
- flywheels,
- gyroscopes,
- optics (beam choppers).

The list is of course non exhaustive. Figure 2.3 identifies the machines in terms of their applications. The targeted motor lies in the micro gas turbines and machine tools region.

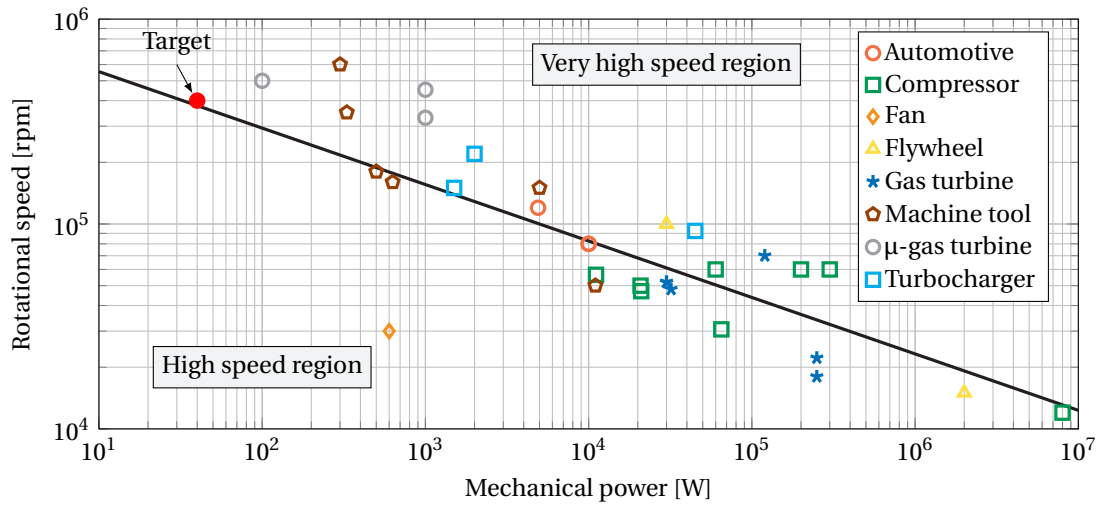


Figure 2.3 – Nominal rotational speed with respect to nominal mechanical power for high speed and very high speed electrical machines in terms of their applications.

#### 2.2.4 Comparative study

In order to identify the competition and the characteristics of the existing machines close to the targeted motor (i.e. 400 krpm-40 W), a comparative study has been performed. In Table 2.1, the targeted motor is compared with 5 others. They all have ball bearings and all are PMSM. Their nominal power and nominal speed are reported, as well as their external dimensions.

None of them fit with the required dimensions. Consequently, the challenge is to design and manufacture a motor running at very high speed while keeping its dimensions reduced. It will result in a miniaturised solution of a VHS machine that can be implemented in medical, dental and machining hand tools, micro gas turbines, or beam choppers for instance.

Manufacturer or university	EPFL	ETHZ	ETHZ	Celeroton AG	Celeroton AG	e+a AG
$P_{mec}$ [W]	40	1000	100	1000	200	2040
$N$ [krpm]	400	330	500	280	500	300
$d_{mot}$ [mm]	12.7	25 <sup>1</sup>	16 <sup>1</sup>	46	22	40
$L_{mot}$ [mm]	30	30 <sup>2</sup>	15 <sup>2</sup>	58.5	28.5	45
Reference	[33]	[34]	[35]	[19]	[19]	[15]

<sup>1</sup> Stator diameter without the housing.

<sup>2</sup> Active length.

Table 2.1 – Characteristics of existing prototypes and commercialised machines close to the targeted region. All are PMSM and have ball bearings.

## 2.3 Losses

### 2.3.1 Location and classification

There are of 2 kinds of losses: mechanical and electrical. Figure 2.4 is a power diagram (in the case of a motor) of all significant losses encountered in PMSM with ball bearings. Losses in the power electronic converter, the connecting wires and the mechanical load are not taken into account. A drawing of a typical PMSM helps to locate the sources and the locations of the losses.

Some losses are directly related to the stator currents, whereas others are related to the rotation of the rotor. The stator currents create Joule losses  $P_{\text{Joule}}$  in the winding. Additionally, they produce time-varying magnetic fields that induce skin effect losses  $P_{\text{skin}}$  and proximity effect losses  $P_{\text{prox}}$  in the winding. The same magnetic field is also responsible for stator iron losses  $P_{\text{ironI}}$  (hysteresis and eddy current losses) and eddy current losses in the rotor  $P_{\text{rot}}$ . For the latter, only the harmonics of the magnetic field, that are asynchronous with the rotation of the rotor, produce losses.

The rotation of the rotor causes 2 sources of mechanical losses, namely windage losses  $P_{\text{windage}}$  and ball bearing losses  $P_{\text{bearings}}$ . Finally, the rotation of the PM leads to a magnetic field that induces eddy current losses in the winding  $P_{\text{windingPM}}$  and iron losses in the stator sheets  $P_{\text{ironPM}}$  (hysteresis and eddy current losses).

### 2.3.2 Power balance

According to Figure 2.4, the mechanical power of a motor is

$$P_{\text{mec}} = P_{\text{el}} - \Sigma P, \quad (2.1)$$

with  $\Sigma P$  being the sum of all the losses given by

$$\Sigma P = P_{\text{Joule}} + P_{\text{skin}} + P_{\text{prox}} + P_{\text{ironI}} + P_{\text{rot}} + P_{\text{windage}} + P_{\text{bearings}} + P_{\text{ironPM}} + P_{\text{windingPM}}. \quad (2.2)$$

In every electrical machine, an intermediary form of energy is encountered, that is electromagnetic energy. Thus, the electromagnetic power can be obtained either by

$$P_{\text{em}} = P_{\text{el}} - (P_{\text{Joule}} + P_{\text{skin}} + P_{\text{prox}}), \quad (2.3)$$

or

$$P_{\text{em}} = P_{\text{mec}} + P_{\text{ironI}} + P_{\text{rot}} + P_{\text{windage}} + P_{\text{bearings}} + P_{\text{ironPM}} + P_{\text{windingPM}}. \quad (2.4)$$

Finally, the efficiency of a motor is defined by

$$\eta = \frac{P_{\text{mec}}}{P_{\text{el}}} = \frac{P_{\text{el}} - \Sigma P}{P_{\text{el}}}. \quad (2.5)$$

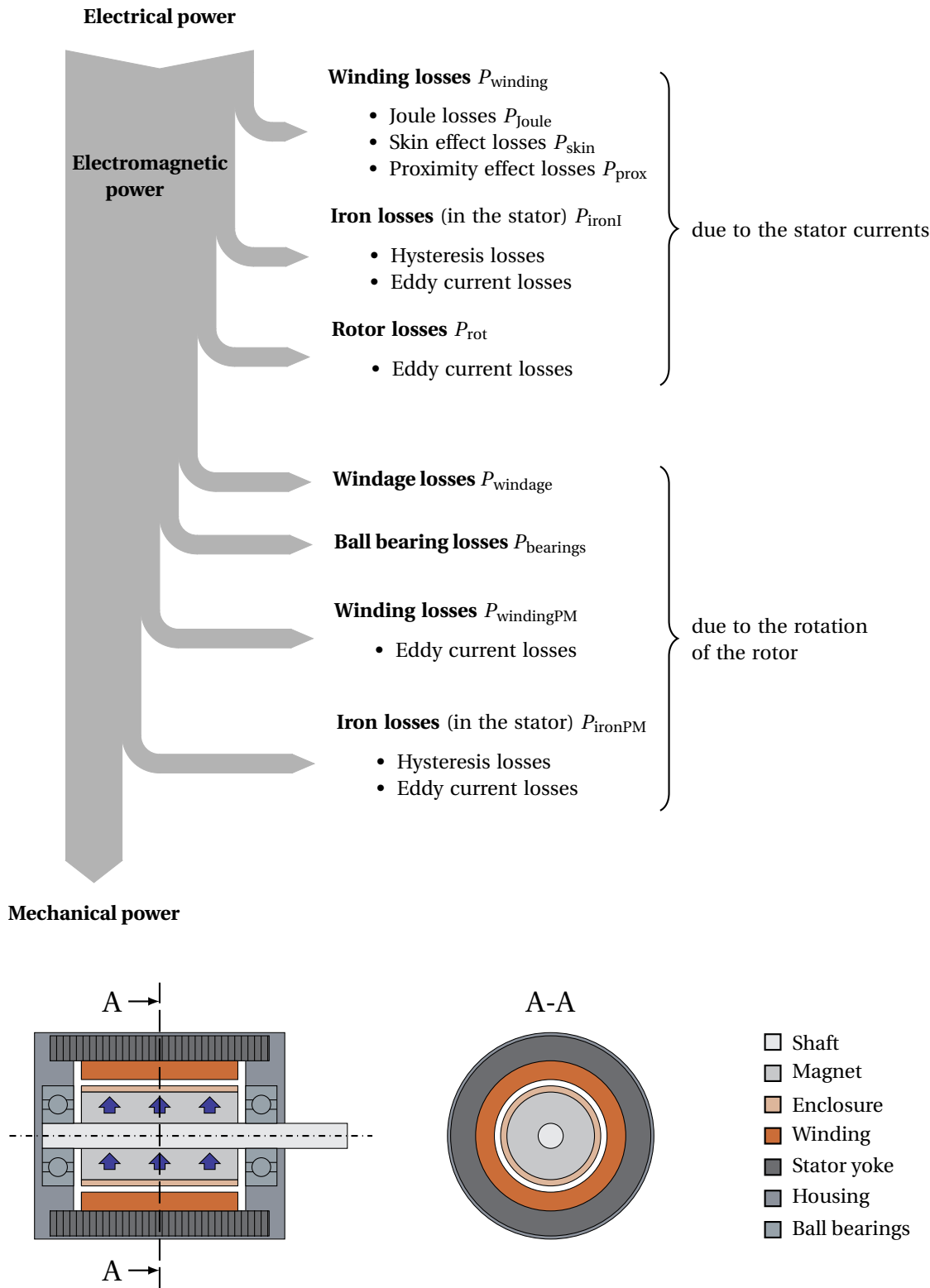


Figure 2.4 – Power diagram (motor) and locations of the losses in a machine (inspired from [3]).

### 2.3.3 Losses specific to very high speed

Although all the aforementioned losses appear in every PMSM with ball bearings, some of these losses become very prominent because of the very high rotational speed and the corresponding electrical frequency.

Windage and ball bearing losses represent a very significant percentage of the total losses, between them reaching 75% in a 500 krpm-100 W PMSM in [31]. Windage losses result from viscous friction of the fluid in the airgap between the rotor and the stator. Friction occurs between the balls, the rings and the lubricant in ball bearings. Unfortunately, the modelling of both losses is extremely complex. For ball bearing losses, some FEM models exist such as the one in [36]. Nevertheless, ball bearing losses depend mainly on the mechanical load, but also on the temperature, the unbalance of the rotor and the ageing of the bearings [35]. Therefore, they are barely considered as design variables, except that their size defines the diameter of the shaft and the minimal diameter of the winding. Nonetheless, ball bearing losses can be measured like demonstrated in [37].

Most of the time, windage losses are assessed by empirical models [38] or by FEM [39, 40]. The first ones are preferred because of their ease. Nonetheless, many empirical models have been devised during the years and all give various estimations of the losses. Consequently, it is imperative to validate experimentally the one that corresponds to the application [12].

Rotor losses induced by eddy currents can become a major issue in VHS machines in the sense that rotors are particularly difficult to cool down. The rise in temperature that they provoke can lead to the demagnetisation of the PMs and additional thermal stresses in the rotor. The most effective solution to reduce this issue is to use slotless stators [41]. Not only does the absence of teeth eliminate the cogging torque and thus the vibration, it also reduces drastically induced rotor losses, as the magnetic field in the airgap is much lower and has lower magnitude of harmonics. Slotted machines are advantageous for lower speed machines, because the magnetic field in the airgap is higher at equal stator current, producing a higher torque [42, 43]. Slotless windings have a low inductance, limiting the back EMF voltage and thus, are widely used for VHS machines [44]. Finally, slotless stators are easier to construct.

The high electrical frequencies (typically in the range of [1-10] kHz) related to very high speeds have a non-negligible influence on electrical losses. It is worth mentioning the skin and proximity effect losses in the winding. Fortunately, these losses can be reduced to insignificant values by using tiny section conductors, like Litz-wire. Obviously, in order to limit the frequency, only single pole pair magnets are used in VHS machines.

Finally, most of electrical losses in very high speed slotless PMSM come from the rotating field of the PM creating losses in the winding and the stator iron. Indeed, in these machines, the magnetic flux density is overwhelmingly caused by the PM. The previously mentioned reduction of the section of conductors goes in the sense of a diminution of these losses in the winding. Plus, the absence of stator teeth definitely reduces the iron losses.

### 2.4 Limitation and design

By essence, VHS machines are pushed to their limits: they experience high mechanical stresses in the materials of the rotor and the bearings, critical speeds, high operating temperatures and the miniaturisation makes the design intricate. Moreover, they are intrinsically multiphysical. The modelling comprises mechanical, thermal, fluid dynamics, electromagnetism, acoustics and material science among others. Lastly, the limitation of all the aforementioned losses is among the main challenges.

One of the difficulty encountered with VHS machines is heating. Indeed, at constant power and efficiency, scaling down the size of the machine results in an increase of losses per surface unit. Therefore, cooling systems often have to be considered.

Another limiting aspect is the maximum mechanical stress supported by the rotor. A given rotor material and diameter constraint the maximal allowed speed. To achieve a sufficient power density, sintered rare-earth permanent magnets (NdFeB or SmCo) are used in electrical machines [45]. Unfortunately, these materials have a low ultimate tensile strength and would brake under the centrifugal forces due to the very high rotational speed. To avoid that, PMs are surrounded by prestressed enclosures or sleeves, typically using material such as titanium, Inconel<sup>®</sup>, glass or carbon fibre [6].

A further sensitive issue is bearings. In VHS applications, bearings are critical and influence the noise, the vibration, the maximal operating speed and the lifespan. Because of the very high speed, it is common that VHS machines break through critical speeds. As a result, a modal analysis is required to ensure that critical speeds do not lie in the operating speed range.

Even though many constraints appear to be mechanical, the fact remains that electrical constraints are present. Due to high electrical frequencies, iron losses can become important. Therefore, appropriate materials have to be selected to limit this phenomenon. The most frequently employed materials are iron-based amorphous and nanocrystalline alloys, which feature low losses at high frequency [46].

The design of VHS machines is closely linked to their applications [9]. The size, the thermal and mechanical constraints can be so different from one case to another that it is difficult to generalise. They have to be designed by considering a systemic approach if the application is *a priori* known. As a result, the models representing the motor should be as robust and reliable as possible.

Despite all these limitations, it is still possible to design and manufacture such machines, but it requires an important modelling work in most of the domains.



## 2.5 Windings

### 2.5.1 Slotless windings

The most common types of slotless windings are pictured in Figure 2.5. The winding in Figure 2.5a is called a skewed or Faulhaber-type winding, the one in Figure 2.5b is a rhombic or Maxon-type winding and the one in Figure 2.5c is a diamond shape winding. Because they lie in the airgap, they are sometimes called self-supporting windings [47]. Similarly to slotted windings, the conductors can be stacked on several layers [48]. The section of conductors is traditionally either round or rectangular. Rectangular section conductors features a better filling factor and a better radial thermal conductivity than round section wires, as there is less space between the turns.

Given that slotless windings are surrounded by air, they consequently have a lower inductance than slotted windings. This leads to higher current ripple, which creates additional iron losses. External inductances can be connected to reduce this phenomenon. Finally, slotless windings are more appropriate for VHS machines as they have a lower back EMF constant, limiting the voltage required by the power electronic converter. Sometimes used in VHS applications, toroidal windings [49] are not suitable for small scale machines mainly because they increase the diameter of the machines.

### 2.5.2 Potential for improvement

As previously mentioned, a transitional form of energy is involved in every electrical machine: electromagnetic energy. Windings participate directly in this process of transformation and are therefore fundamental components. Their improvement leads directly to significant increases of the performances in a machine. Finally, they directly impact the efficiency of a machine, as they are responsible for the creation of losses (see Section 2.3).

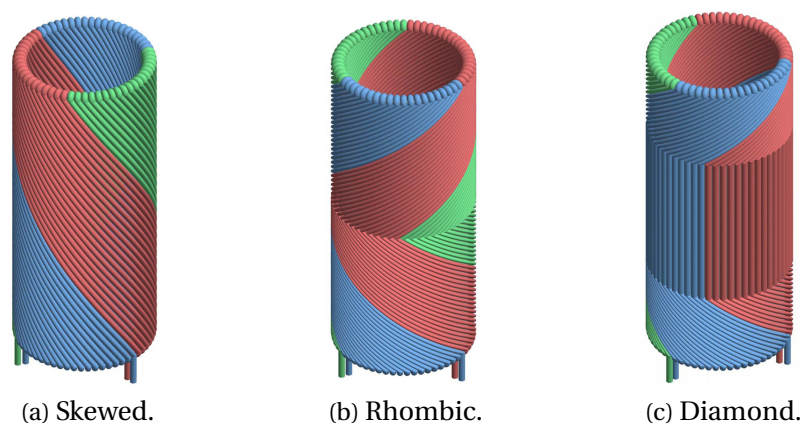
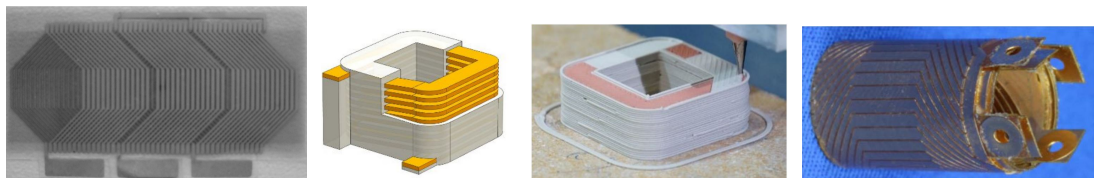


Figure 2.5 – Most common types of slotless windings from [4].

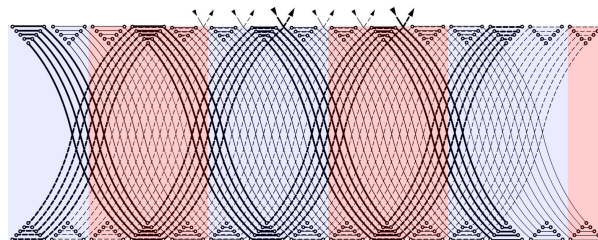
One of the main interests of slotless windings is the numerous possible shapes and topologies they can embrace. Unlike slotted windings forced to follow the direction of slots, slotless windings can be freely arranged in the airgap. This represents an opportunity for optimisation.

Yet, only little research has been performed in this domain so far. One can cite a slotless winding manufactured with 3D screen printing by Lindner *et al.* as visible in Figure 2.6a [50]. One of the key aspects in this research was the use of nonconstant wires section, possibly achieved by additive manufacturing. However, the shape has not been optimised. Bräuer *et al.* (from the same research team) have also proposed the idea of printing hollow conductors for cooling purposes, with the same printing technology [51]. More recently, slotted windings have also been investigated by Lorenz *et al.* as visible in Figure 2.6b [52, 53]. Dehez *et al.* have investigated a flexible PCB winding for slotless machines with nonconstant track widths as pictured in Figure 2.6c [54]. They have also demonstrated in [55] the significant increase of the performances of a motor, thanks to an optimal track shape as depicted in Figure 2.6d.

Recent research has focused on additive manufacturing for electrical machines or components [52, 53, 56, 57] and has shown potential in this domain. Thanks to these emerging possibilities, such as selective laser melting (SLM), electron beam melting (EBM) [58, 59], 3D screen printing [51, 60], or more conventional ones, like wire-cut electrical discharge machining (WEDM) [61] or laser cutting, innovation can be considered in the design and manufacturing of slotless windings. These new technologies intend to challenge the traditional way of manufacturing windings. Indeed, most of the windings are made with isolated wire of constant section. However, it has been demonstrated that the performances of a motor can be significantly increased by optimising the shape of the winding and by selecting nonconstant wire sections.



(a) Screen printed slotless winding [50]. (b) Screen printed slotted winding [53]. (c) PCB winding [54].



(d) Optimised PCB winding [55].

Figure 2.6 – Illustrations of the possibilities to improve windings.

## **2.6 Previous academic works**

Given that VHS machines have been the subject of research for some time, the present thesis built upon previous academic works :

- Larssonneur with the study of active magnetic bearings (1990) [62],
- Saari with a remarkable work on the classification of empirical windage losses models (1998) [38],
- Zwyssig with the investigation and experimental validation of a 500 krpm-100 W electrical motor with ball bearings and the development of a control electronic (2006) [63],
- Pfister with the theoretical study and the experimental validation of a 200 krpm-2 kW electrical motor with ball bearings (2010) [3],
- Borisavljević with the development and the validation of a high speed electrical motor with aerostatic bearings for micro mechanical machining (2011 and 2013) [12, 64].

## **2.7 Conclusion**

The state of the art lays the basis for VHS machines. Thanks to a review of 49 commercial machines and prototypes, the type of machine and bearings, as well as the potential applications have been discussed. A comparative study has demonstrated that the targeted motor, i.e. a 400 krpm 40 W 12.7 mm diameter 28 mm length, has no counterparts in terms of miniaturisation, whether it is a prototype or a commercialised machine. The losses and the limitation of VHS machines have been tackled, and it is inferred that a robust modelling is necessary for their design.

From the state of the art, it can be concluded that the targeted motor has to be:

- a PMSM with a retaining sleeve around a one pole pair magnet,
- slotless, thus it requires a slotless winding,
- with ball bearings.

Finally, the potential of improvement for slotless windings has been discussed. With the help of nonconstant wires section, an optimised shape and nontraditional manufacturing processes, the performances of electrical machines can be significantly increased.



## 3 Mechanical modelling

### Contents

---

<b>3.1 Introduction</b>	<b>22</b>
<b>3.2 Rotor stresses</b>	<b>23</b>
3.2.1 Geometry and mechanical properties	23
3.2.2 Stresses in the rotor	25
3.2.3 Failure criterion	28
3.2.4 Validation of the model	30
3.2.5 Limitation of the model	31
<b>3.3 Modal analysis</b>	<b>34</b>
3.3.1 Vibration modes	34
3.3.2 Critical speeds	34
3.3.3 Equation of motion	35
3.3.4 Computation of critical speeds	35
<b>3.4 Windage losses</b>	<b>37</b>
<b>3.5 Ball bearing losses</b>	<b>40</b>
<b>3.6 Conclusion</b>	<b>40</b>

---

Publications of the author related to this chapter:

- Guillaume Burnand, Douglas Martins Araujo, and Yves Perriard. Very-high-speed permanent magnet motors: Mechanical rotor stresses analytical model. In *IEEE International Electric Machines and Drives Conference (IEMDC)*, pages 1–7. IEEE, May 2017.
- Guillaume Burnand, Douglas Martins Araujo, Christian Koechli, and Yves Perriard. Validation by measurements of a windage losses model for very-high-speed machines. In *20th International Conference on Electrical Machines and Systems (ICEMS)*, pages 1–4. IEEE, August 2017.

### 3.1 Introduction

Mechanical modelling is inherent to the design of VHS machines. The rotor, including the bearings, is one of the most critical parts to design. The aspects to be considered are the mechanical strength of the rotating parts, the critical speeds and the losses.

Rotating parts have to be designed so that the rotational velocity, but also the temperature, will not plastically deform them, leading to an unbalancing or even worse, a mechanical break. This applies especially to permanent magnets, which are the most fragile part of the rotor and require a retaining sleeve. Research has already been performed on the design of VHS permanent magnet rotors [12, 62, 65–68]. Based on [3, 69], a very complete analytical model that evaluates the stresses everywhere in the rotor, and guarantees the mechanical strength is developed in Section 3.2. It differs from other models by including:

- the computation of the axial stress components leading to a 3D model,
- the computation of stresses in the shaft,
- the distinction between cylinder and disc shaped rotors,
- the distinction between hollow and solid magnet rotors,
- the consideration of thermal stresses.

VHS machines commonly run at overcritical speeds (faster than the first critical speed). Therefore, it is important that critical speeds do not lie near the operating rotational speed range. They would create vibration, noise and reduce the accuracy of the driven load. In Section 3.3, 3D FEM is used to model the rotor and the bearings and to compute the critical speeds. The results are later compared with measurements in Chapter 6, in order to validate the model.

Finally, mechanical losses, which are divided into windage and ball bearing losses, represent a substantial part of the total losses in VHS machines. Indeed, in low speed machines, mechanical losses are of no or little significance, whereas they can reach up to 75% of the total losses in VHS machines [31]. Consequently, windage and ball bearing losses have to be known very precisely. Windage losses are very complex phenomena based on fluid dynamics theory. For that reason, most of analytical windage losses models are empirical [38]. Many of them exist and give variation estimations of the losses. As a result, the chosen model must be validated regarding the application of the machine [12]. An existing model is presented in Section 3.4 and experimentally validated in Chapter 6.

As for ball bearing losses, it is very complicated to predict them with models for VHS operations, thereby they are most of the time measured [3]. In Section 3.5, an empirical model is proposed, which is used along with an experimental technique able to separate the losses in Chapter 6.

## 3.2 Rotor stresses

### 3.2.1 Geometry and mechanical properties

#### Geometry of the rotor

The model considers a hollow magnet rotor composed of a shaft, a permanent magnet and an enclosure as illustrated in Figure 3.1. The index s stands for shaft, m for magnet, e for enclosure, i for inner and o for outer. Given the geometry of the rotor, cylindrical coordinates are used. It may happen (for manufacturing reasons) that the shaft does not pass through the magnet. In that case, it is a solid magnet rotor. Thereafter, the model is adapted by tending the inner radius of the magnet  $r_{mi}$  to zero in the following equations.

#### Mechanical parameters

The materials composing the rotor are defined by their mechanical properties:

- Young's modulus:  $E$  [Pa]
- Poisson's ratio:  $\nu$  [-]
- Coefficient of thermal expansion (CTE):  $c$  [ $1/^\circ\text{C}$ ]
- Density:  $\rho$  [ $\text{kg m}^{-3}$ ]

They are assumed to be isotropic, homogenous and in the elastic domain.

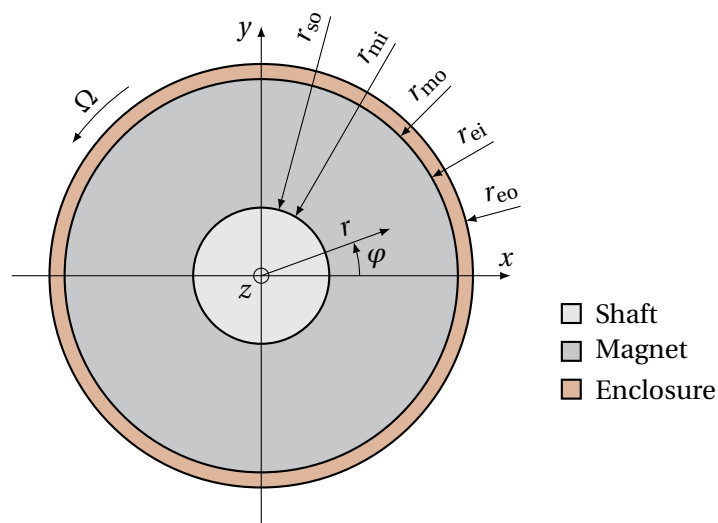


Figure 3.1 – Cross-section giving the geometry and the dimensions of the rotor stresses model.

### Chapter 3. Mechanical modelling

---

The last two parameters contained in the model are:

- Temperature:  $T$  [°C]
- Rotational speed:  $\Omega$  [rad/s]

The temperature is considered homogeneous in the rotor.

#### Plane strain and plane stress conditions

The stress  $\sigma$  is represented by its radial component  $\sigma_r$  and its tangential component  $\sigma_\varphi$ . Due to the axisymmetry of the problem, the stress components depend on  $r$  only. In the case where one dimension is small compared to the others (i.e. disc shaped rotors), the plane stress condition [69] is used:

- Axial stress:  $\sigma_z = 0$  [Pa]
- Axial strain:  $\varepsilon_z \neq 0$  [-]

Conversely, if one dimension is large in comparison to the others (i.e. cylinder shaped rotors), the plane strain condition [69] is made:

- Axial stress:  $\sigma_z \neq 0$  [Pa]
- Axial strain:  $\varepsilon_z = 0$  [-]

In plane strain condition, since no axial strain is allowed, thermal axial constraints will appear due to the expansion of materials. This axial component has to be considered [62], otherwise the total stress would be underestimated [70]. In plane strain condition, the axial stress, taking into account the variation of temperature  $\Delta T$ , is obtained by

$$\sigma_z = \nu(\sigma_r + \sigma_\varphi) - Ec\Delta T. \quad (3.1)$$

In addition, the parameters of the materials are modified [12], but only for the computation of radial and tangential stress components, as

$$\nu^* = \frac{\nu}{1 - \nu}, \quad (3.2)$$

$$E^* = \frac{E}{1 - \nu^2}, \quad (3.3)$$

$$c^* = c(1 + \nu). \quad (3.4)$$

Table 3.1 summarises the difference between plane strain and plane stress conditions.



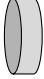

	Plane stress	Plane strain
Shape		
$\varepsilon_z$	$\neq 0$	$= 0$
$\sigma_z$	$= 0$	$= \nu(\sigma_r + \sigma_\phi) - Ec\Delta T$
$\sigma_r, \sigma_\phi, \sigma_c, u, e$	$\nu, E, c$	$\nu^*, E^*, c^*$

Table 3.1 – Plane strain and plane stress conditions.

### 3.2.2 Stresses in the rotor

#### Differential equation

A thick-walled cylinder rotating at a constant angular velocity  $\Omega$  is governed by the following differential equation [69]

$$\frac{d^2 u}{dr^2} + \frac{1}{r} \frac{du}{dr} - \frac{u}{r^2} = -\left(\frac{1-\nu^2}{E}\right)\rho\Omega^2 r, \quad (3.5)$$

where  $u$  is the mechanical displacement. The right-hand side term takes into account the effect of rotational velocity. For the 3 regions of the rotor, that are the shaft, the magnet and the enclosure ( $i = s, m, e$ ), the general solution is

$$u_i = -\left(\frac{1-\nu_i^2}{8E_i}\right)\rho_i\Omega^2 r^3 + c_{i1}r + \frac{c_{i2}}{r}, \quad (3.6)$$

and the radial and tangential stresses are respectively

$$\sigma_{ir} = \frac{E_i}{1-\nu_i^2} \left[ \frac{-(3+\nu_i)(1-\nu_i^2)\rho_i\Omega^2 r^2}{8E_i} + c_{i1}(1+\nu_i) - c_{i2}\left(\frac{1-\nu_i}{r^2}\right) \right], \quad (3.7)$$

and

$$\sigma_{i\phi} = \frac{E_i}{1-\nu_i^2} \left[ \frac{-(1+3\nu_i)(1-\nu_i^2)\rho_i\Omega^2 r^2}{8E_i} + c_{i1}(1+\nu_i) + c_{i2}\left(\frac{1-\nu_i}{r^2}\right) \right], \quad (3.8)$$

where  $c_{i1}$  and  $c_{i2}$  are integration constants.

### Boundary conditions

The integration constants are fixed considering the boundary conditions

$$u_s(r = 0) = 0, \quad (3.9)$$

$$\sigma_{sr}(r = r_{so}) = 0, \quad (3.10)$$

$$\sigma_{mr}(r = r_{mi}) = 0, \quad (3.11)$$

$$\sigma_{mr}(r = r_{mo}) = \sigma_c, \quad (3.12)$$

$$\sigma_{er}(r = r_{ei}) = \sigma_c, \quad (3.13)$$

$$\sigma_{er}(r = r_{eo}) = 0, \quad (3.14)$$

where  $\sigma_c$  is the radial contact stress at the magnet-enclosure interface. This stress is created by the interference, also called shrinkage, between the magnet and the enclosure. Namely, the inner radius of the enclosure is smaller than the outer radius of the magnet. This induces a prestress on the magnet. As a result, the latter tolerates higher stresses due to rotation than it would without enclosure.

Because the solution needs to be finite at the centre of the shaft,  $c_{s2} = 0$ . Boundary conditions (3.10) and (3.11) imply that there is no physical contact at the shaft-magnet interface. Indeed, the contact cannot be guaranteed for manufacturing reasons.

### Solutions

The equations for a hollow magnet rotor under plane strain condition are given bellow. The stresses in the shaft are

$$\sigma_{sr}(r) = \frac{(3 + \nu_s^*)\rho_s\Omega^2}{8}(r_{so}^2 - r^2), \quad (3.15a)$$

$$\sigma_{s\varphi}(r) = \frac{(3 + \nu_s^*)\rho_s\Omega^2}{8}\left(r_{so}^2 - \left(\frac{1 + 3\nu_m^*}{3 + \nu_m^*}\right)r^2\right), \quad (3.15b)$$

$$\sigma_{sz}(r) = \nu_s(\sigma_{sr}(r) + \sigma_{s\varphi}(r)) - E_s c_s \Delta T. \quad (3.15c)$$

The radial and tangential stresses in the shaft are proportional to the square of the angular velocity.

The stresses in the magnet are

$$\begin{aligned} \sigma_{mr}(r) = & \frac{(3 + \nu_m^*)\rho_m\Omega^2}{8} \left( -r^2 + r_{mo}^2 + r_{mi}^2 - \left( \frac{r_{mo}r_{mi}}{r} \right)^2 \right) + \\ & \frac{\sigma_c}{1 - \left( \frac{r_{mi}}{r_{mo}} \right)^2} \left( 1 - \left( \frac{r_{mi}}{r} \right)^2 \right), \end{aligned} \quad (3.16a)$$

$$\begin{aligned} \sigma_{m\varphi}(r) = & \frac{(3 + \nu_m^*)\rho_m\Omega^2}{8} \left( -\left( \frac{1 + 3\nu_m^*}{3 + \nu_m^*} \right) r^2 + r_{mo}^2 + r_{mi}^2 + \left( \frac{r_{mo}r_{mi}}{r} \right)^2 \right) + \\ & \frac{\sigma_c}{1 - \left( \frac{r_{mi}}{r_{mo}} \right)^2} \left( 1 + \left( \frac{r_{mi}}{r} \right)^2 \right), \end{aligned} \quad (3.16b)$$

$$\sigma_{mz}(r) = \nu_m(\sigma_{mr}(r) + \sigma_{m\varphi}(r)) - E_m c_m \Delta T. \quad (3.16c)$$

The stresses in the enclosure are

$$\begin{aligned} \sigma_{er}(r) = & \frac{(3 + \nu_e^*)\rho_e\Omega^2}{8} \left( -r^2 + r_{eo}^2 + r_{ei}^2 - \left( \frac{r_{eo}r_{ei}}{r} \right)^2 \right) + \\ & \frac{\sigma_c}{1 - \left( \frac{r_{eo}}{r_{ei}} \right)^2} \left( 1 - \left( \frac{r_{eo}}{r} \right)^2 \right), \end{aligned} \quad (3.17a)$$

$$\begin{aligned} \sigma_{e\varphi}(r) = & \frac{(3 + \nu_e^*)\rho_e\Omega^2}{8} \left( -\left( \frac{1 + 3\nu_e^*}{3 + \nu_e^*} \right) r^2 + r_{eo}^2 + r_{ei}^2 + \left( \frac{r_{eo}r_{ei}}{r} \right)^2 \right) + \\ & \frac{\sigma_c}{1 - \left( \frac{r_{eo}}{r_{ei}} \right)^2} \left( 1 + \left( \frac{r_{eo}}{r} \right)^2 \right), \end{aligned} \quad (3.17b)$$

$$\sigma_{ez}(r) = \nu_e(\sigma_{er}(r) + \sigma_{e\varphi}(r)) - E_e c_e \Delta T. \quad (3.17c)$$

Both the radial and tangential stresses in the magnet and the enclosure are composed by a term proportional to the contact stress at the magnet-enclosure interface, and another term proportional to the square of the angular velocity. At standstill, stresses are induced merely by the contact stress.

### Contact stress

The contact stress depends on the operating interference  $e$  at the magnet-enclosure interface which is given by

$$e = (r_{mo} - r_{ei}) + (u_{mo}^{\Omega} - u_{ei}^{\Omega}) + (r_{mo}c_m^* - r_{ei}c_e^*)\Delta T. \quad (3.18)$$

It is composed of three terms: the first one is the interference at standstill and room temperature (also referred to as  $e_0$  thereafter), the second one is the interference due to the effect of rotational velocity, and the third one takes into account the thermal expansion of pieces.

Thanks to (3.6), the displacement  $u_{mo}^{\Omega}$ , which corresponds to the expansion at the outer circumference of the magnet due to the rotating speed as if there was no enclosure, is computed as

$$u_{mo}^{\Omega} = u_m^{\Omega}(r = r_{mo}) = \frac{(3 + \nu_m^*)\rho_m\Omega^2 r_{mo}^3}{4E_m^*} \left( \frac{1 - \nu_m^*}{3 + \nu_m^*} + \left( \frac{r_{mi}}{r_{mo}} \right)^2 \right). \quad (3.19)$$

Similarly, the displacement  $u_{ei}^{\Omega}$ , which corresponds to the expansion at the inner circumference of the enclosure due to the rotating speed as if there was no magnet, is calculated as

$$u_{ei}^{\Omega} = u_e^{\Omega}(r = r_{ei}) = \frac{(3 + \nu_e^*)\rho_e\Omega^2 r_{ei}r_{eo}^2}{4E_e^*} \left( 1 + \frac{1 - \nu_e^*}{3 + \nu_e^*} \left( \frac{r_{ei}}{r_{eo}} \right)^2 \right). \quad (3.20)$$

Finally, the contact stress at the magnet-enclosure interface is given by

$$\sigma_c = \frac{-e}{r_{mo} \left( \frac{1}{E_e^*} \left( \frac{r_{eo}^2 + r_{ei}^2}{r_{eo}^2 - r_{ei}^2} + \nu_e^* \right) + \frac{1}{E_m^*} \left( \frac{r_{mo}^2 + r_{mi}^2}{r_{mo}^2 - r_{mi}^2} - \nu_m^* \right) \right)}. \quad (3.21)$$

The negative value of  $\sigma_c$  guarantees the contact between the magnet and the enclosure.

### 3.2.3 Failure criterion

#### Von Mises criterion

To ensure the mechanical strength, the von Mises yield criterion is chosen because it is closer to reality than the Tresca criterion [69]. This criterion is commonly used in the elastic range. It suggests that the yielding of the material begins once the distortion energy reaches a critical value. In other words, the von Mises stress  $\sigma_v$  must be smaller than the yield strength  $\sigma_y$  for the shaft and the enclosure and smaller than the ultimate tensile strength  $\sigma_t$  for the

magnet<sup>1</sup>. Accordingly, no plastic deformation, that would unbalance the rotor or even break it, is tolerated.

The von Mises stress is expressed as

$$\sigma_v = \sqrt{\frac{1}{2} ((\sigma_r - \sigma_\varphi)^2 + (\sigma_\varphi - \sigma_z)^2 + (\sigma_z - \sigma_r)^2)}. \quad (3.22)$$

The von Mises criterion enables the reduction of three stress components to a single positive scalar value, easily comparable to the yield strength (or the ultimate tensile strength).

#### Mechanical strength

The conditions to be fulfilled to guarantee the mechanical strength of the whole rotor are

$$\max(\sigma_{sv}) < \sigma_{sy}, \quad (3.23a)$$

$$\max(\sigma_{mv}) < \sigma_{mt}, \quad (3.23b)$$

$$\max(\sigma_{ev}) < \sigma_{ey}, \quad (3.23c)$$

$$\sigma_c < 0, \quad (3.23d)$$

throughout the speed and temperature range. It should be mentioned that even at standstill, induced stresses due to the shrinkage between the magnet and the enclosure could be destructive. In addition, the temperature can create a significant increase of stresses. A particular attention has to be paid to magnets, because they are more fragile than the shaft and the enclosure.

In practice, safety coefficients can be used on the yield strength and the ultimate tensile strength. They take into account the tolerated risk of failure related to the application, the fatigue of materials, the desired lifetime and the possible materials defects. It is also common to design a rotor that withstands a higher speed than its nominal speed.

---

<sup>1</sup>Sintered materials do not behave like dense materials in the plastic domain [71]. Consequently, the yield strength of sintered magnets is not usually precisely known and the ultimate tensile strength is used instead.

### 3.2.4 Validation of the model

#### 3D FEM model

A 3D FEM rotor is modelled with ANSYS in order to validate the analytical model presented in Section 3.2. The geometry of the rotor and its mesh are pictured in Figure 3.2. The mechanical parameters and the dimensions used are listed in Table 3.2.

The boundary conditions at the two extremities of the rotor are set so that no axial strain is possible, producing a plane strain condition. The contact at the magnet-enclosure interface is modelled as *rough* with an augmented Lagrange formulation.

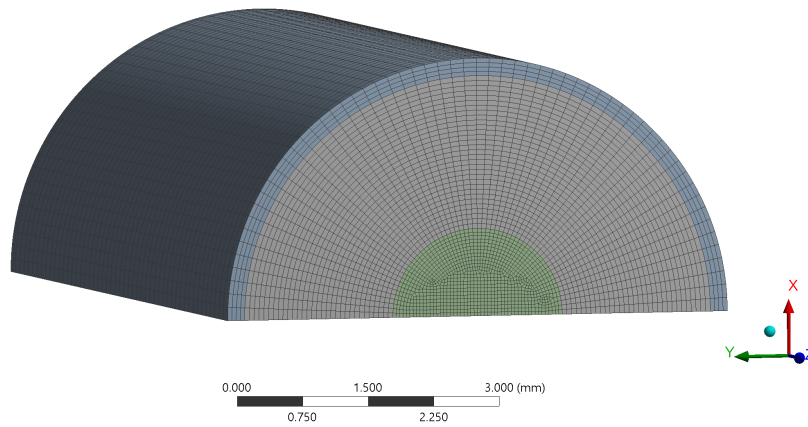


Figure 3.2 – Meshed ANSYS 3D FEM model for the computation of rotor stresses.

Mechanical and geometrical parameters					
		Shaft	Magnet	Enclosure	
Material		Martensitic steel 420 F	NdFeB	Titanium grade 5	
Density	$\rho_i$	7700	7500	4400	[kg/m <sup>3</sup> ]
Poisson's ratio	$\nu_i$	0.24	0.24	0.36	[-]
Young's Modulus	$E_i$	215	160	114	[GPa]
CTE	$c_i$	$10.5 \times 10^{-6}$	$5.0 \times 10^{-6}$	$9.0 \times 10^{-6}$	[1/°C]
Ultimate tensile strength	$\sigma_{it}$	-	75	-	[MPa]
Yield strength	$\sigma_{iy}$	1550	-	880	[MPa]
Inner radius	$r_{ii}$	-	1	2.75	[mm]
Outer radius	$r_{io}$	1	2.762	2.95	[mm]
Physical parameters					
Maximal rotational speed	$N_{\max}$		500		[krpm]
Temperature	$T$		60		[°C]

Table 3.2 – Simulation parameters used for the validation of the rotor stresses model.

### Results

Figure 3.3 compares the three stress components ( $\sigma_r, \sigma_\phi, \sigma_z$ ) in the shaft, the magnet and the enclosure at both standstill and at maximal rotational speed. The continuous lines refer to the analytical model and the dashed ones to the FEM model.

It can be noted that the radial stress is equal to zero at the shaft-magnet interface thanks to boundary conditions (3.10) and (3.11). This can be seen in Figures 3.3a and 3.3b. Regarding the magnet-enclosure interface, the radial stress is equal to  $\sigma_c$  thanks to boundary conditions (3.12) and (3.13). The negative value of this contact stress ensures that no separation will occur.

Because there is no contact with the magnet, radial and tangential stresses are nil at standstill in the shaft, as visible in Figures 3.3a and 3.3c. However, the axial stress is different from zero because of the thermal stress. Thermal stresses can reach significant values regarding the CTE and the Young's modulus of materials. They have to be considered, especially in VHS machines, where the temperature is often high.

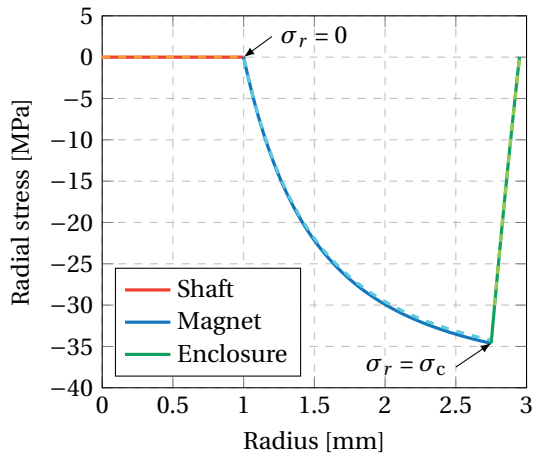
The von Mises stress is computed in ANSYS (Figure 3.4) and is compared to the model in Figure 3.5. The ultimate tensile strength of the magnet  $\sigma_{mt}$  is highlighted on the graph. The analytical model fits the FEM model extremely well. The error on the von Mises stresses is less than 1%. As previously mentioned, magnets are the most fragile part of the rotor. This fact is verified here, as the maximal value of the von Mises stress is just below the ultimate tensile strength.

In general, the maximal value of the von Mises stress in hollow cylinders appears to be at the inner circumference [62]. In the case of solid cylinders however, this value is lower (for the same outer radius) and appears at the centre. This fact has to be taken into consideration when choosing between a solid or a hollow magnet rotor.

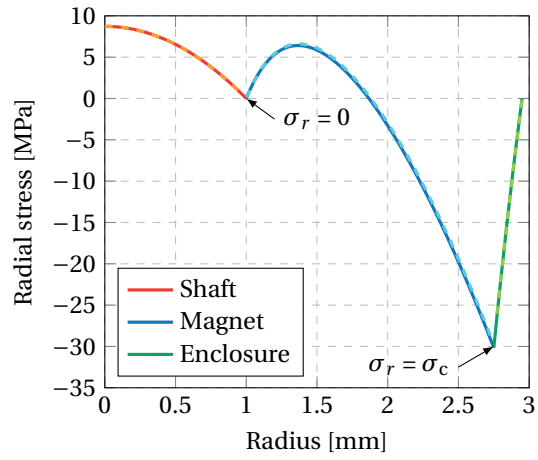
Stresses in the rotor can be limited by diminishing the size of the rotor, selecting low density materials or by reducing the temperature. In high temperature applications, such as micro gas turbines, low CTE materials should be chosen in order to lessen thermal stresses.

### 3.2.5 Limitation of the model

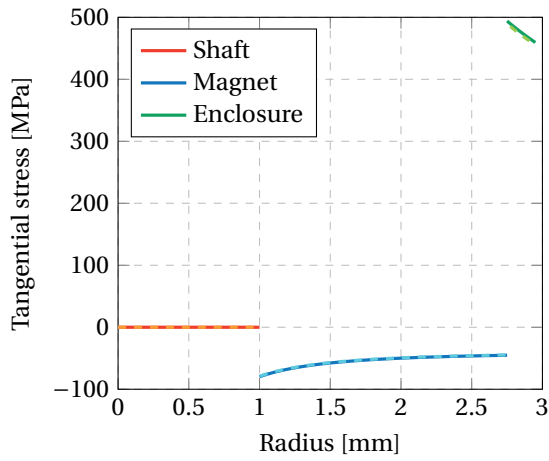
A rotor is seldom fully under plain stress or plain strain conditions. It is usually somewhere in between. The axial stress components come from the plain strain condition, which does not permit axial strain. It can correspond to the case of a rotor with ball bearings, where the longitudinal expansion is limited (but not completely impossible).



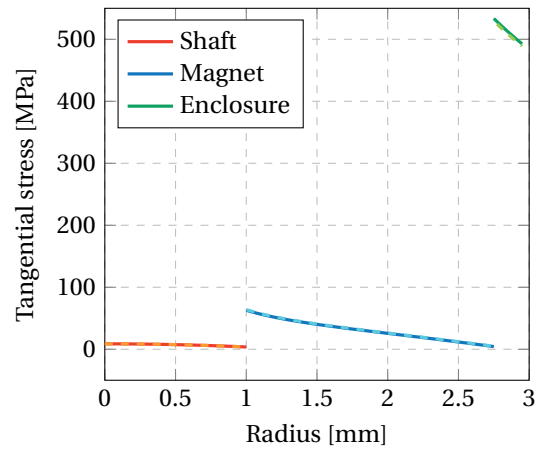
(a) Standstill.



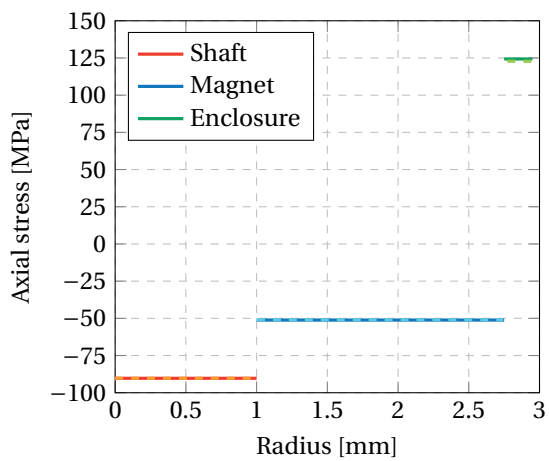
(b) Maximal speed.



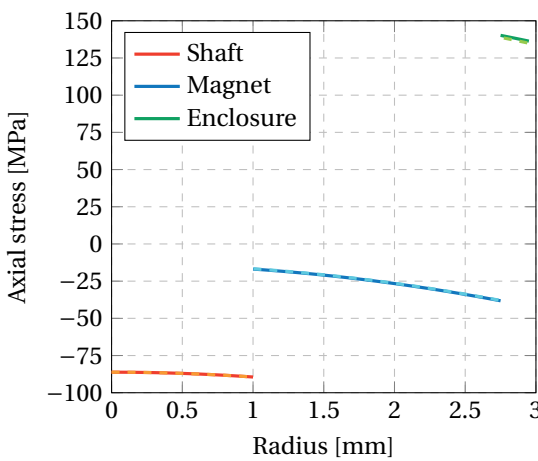
(c) Standstill.



(d) Maximal speed.



(e) Standstill.



(f) Maximal speed.

Figure 3.3 – Validation of the stresses components in the rotor.



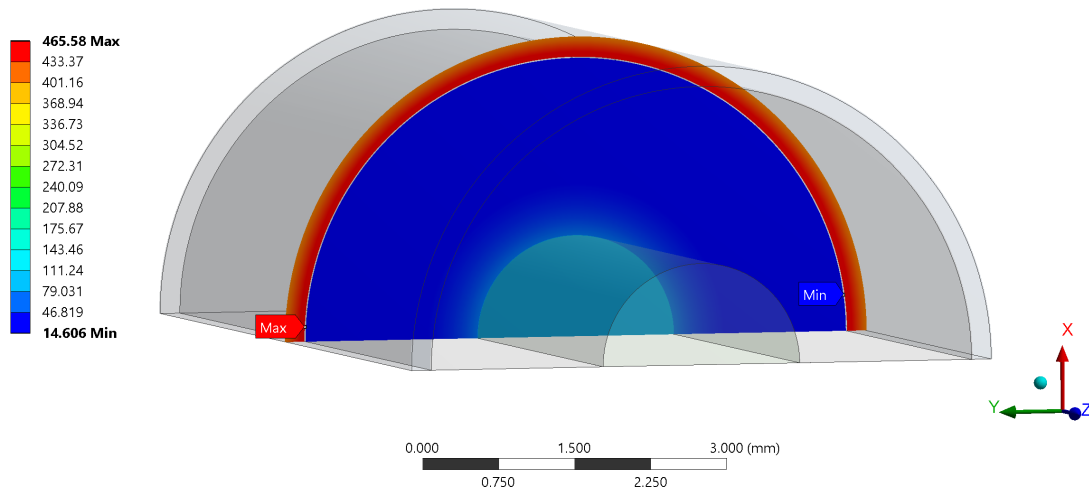


Figure 3.4 – Von Mises stress at standstill in ANSYS (scale in MPa).

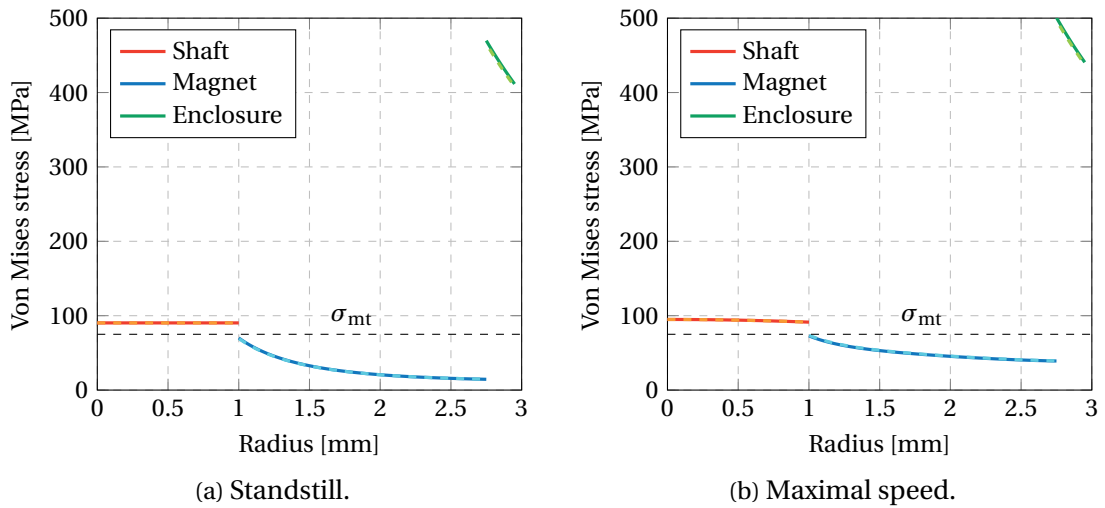


Figure 3.5 – Validation of the von Mises stress in the rotor.

In that case, it has been demonstrated that a 2D stresses model would underestimate the total stresses [70]. In other cases, e.g. with magnetic bearings, it is a conservative assumption in the sense that the rotor can expand longitudinally as the temperature increases. As a result, axial stresses diminish. In both cases, a conservative model is preferred and brings more safety to the design.

Finally, an analytical model is preferred to a FEM model, which is time consuming. Analytical models can be implemented easily in optimisation loops, as in Chapter 5.

### 3.3 Modal analysis

#### 3.3.1 Vibration modes

Just like vibrating strings, rotors have natural frequencies characterised by vibration modes. Rigid body modes occur when the bearings are very flexible towards the shaft (soft mounted rotors). For axisymmetric rotors and stators, the first rigid body mode corresponds to a cylindrical whirling (0-node mode) and the second one, occurring at higher speed, to a conical whirling (1-node mode) [72]. Both modes are illustrated in Figures 3.6a and 3.6b.

Flexural modes (also called deformation or bending modes) happen when the bearings are very rigid towards the shaft (hard mounted rotors). Rotors deform and are affected by a rotating damping. The first flexural mode is half sine shaped (2-nodes mode). Then comes the second flexural mode also sine shaped (3-nodes mode) and so on as the speed increases. The first two bending modes are depicted in Figures 3.6c and 3.6d. Hard mounted rotors are preferred for precision applications, but have less damping capability and hence, transmit more vibration to the frame. In fact, bearings are seldom very flexible or rigid with respect to the shaft. Thus, actual rotors have a combination of both vibration mode types.

#### 3.3.2 Critical speeds

A critical speed is defined as a rotating speed that excites one of the low damped natural frequencies of the rotor [73]. The rotor starts to resonate as the speed gets closer to the natural frequency and causes vibration. In low speed applications, most of rotors run under the first critical speed (subcritical) and no particular considerations of modal analysis are necessary. However, VHS machines operate commonly above the first critical speed (overcritical or supercritical). Thus it is important to know the critical speeds so that they do not lie near the operating speed range. However, if the bearings are damped enough, some critical speeds may not occur.

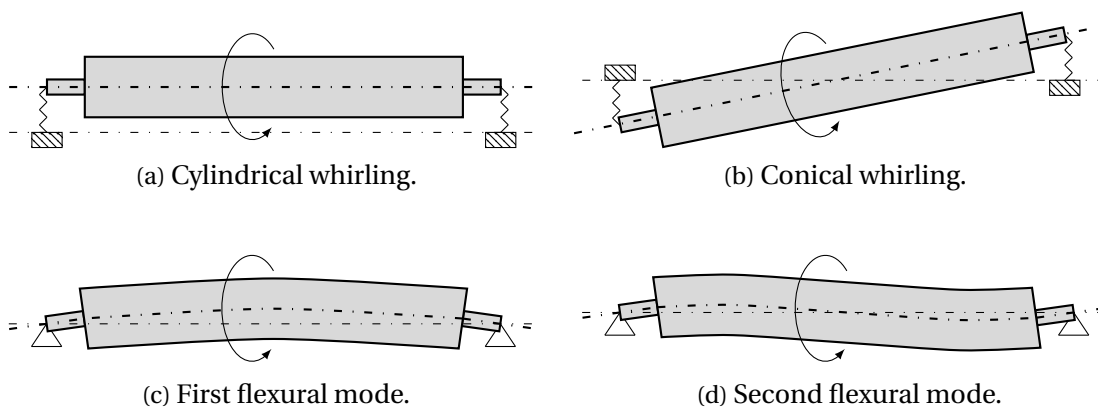


Figure 3.6 – Representation of the vibration modes.

### 3.3.3 Equation of motion

The equation of motion for a linear axisymmetric shaft rotating at a constant speed [72] is

$$\mathbf{M} \ddot{\vec{u}}(t) + (\mathbf{C} + \mathbf{G}) \dot{\vec{u}}(t) + \mathbf{K} \vec{u}(t) = \vec{f}(t), \quad (3.24)$$

where  $\vec{u}(t)$  is the displacement vector,  $\mathbf{M}$  the symmetric mass and inertia matrix,  $\mathbf{C}$  the symmetric damping matrix,  $\mathbf{G}$  the skew-symmetric gyroscopic matrix,  $\mathbf{K}$  the symmetric stiffness matrix and  $\vec{f}(t)$  a time-dependent source vector. This last vector can be, for instance, a force caused by the unbalance of the rotor. The vector  $\vec{f}(t)$  is set to zero in the case of free vibration analysis, i.e. the computation of natural frequencies.

Matrix  $\mathbf{G}$  is proportional to the rotational velocity of the rotor. As a result, the solutions of (3.24) also depend on the rotational velocity. Solutions can be found analytically for simple rotor geometries [72], or with 1D FEM [74] and 3D FEM for more complex ones. Solving (3.24) comes down to an eigenvalue problem. The imaginary part of the eigenvalues gives the natural frequencies.

### 3.3.4 Computation of critical speeds

#### 3D FEM model

Figure 3.7 pictures the ANSYS 3D FEM model used for the computation of critical speeds. Both ball bearings are modelled by the hollow grey discs at the extremities of the shaft. Bearings are isotropic and their radial stiffness is set to 1.75 N/ $\mu\text{m}$  (see Section 6.3.5 for more details). The rotor, including the bearings, has been designed so that no critical speeds occur around the operating speed, which is 400 krpm. To this end, the value of the radial stiffness can be modified to some extent, by varying the preload of ball bearings. The higher the stiffness, the higher the critical speeds [75]. Hence, the 2 degrees of freedom for acting upon critical speeds are the materials and dimensions of the shaft and the stiffness of bearings.

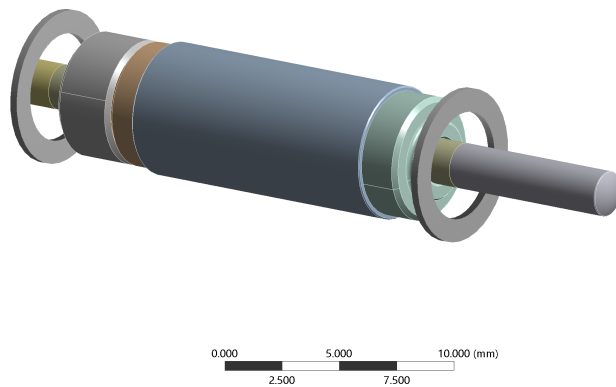


Figure 3.7 – Modeling of the ball bearings and the rotor in ANSYS for the computation of critical speeds.

### Campbell diagram

Plotting the natural frequencies  $f$  with respect to the rotational speed  $\Omega$  leads to a so called Campbell diagram as shown in Figure 3.8. Complex conjugate solutions of (3.24) give two whirling motions per mode: forward (F) and backward (B). The rotor always rotates in the same direction, which is imposed by the rotating magnetic field of the stator. However, the whirl motion can be superimposed in the same direction (forward) or in the opposite direction (backward) [76]. In the case of an axisymmetric rotor and isotropic bearings, the whirl is forward and circular.

Because a rotor is never perfectly balanced, it creates forcing frequencies that excite natural frequencies. This synchronous excitation ( $2\pi f = \Omega$ ) is plotted in the Campbell diagram (black line in Figure 3.8). The intersection of this line with the natural frequencies gives the critical speeds. However, every intersection is not necessarily a critical speed. Indeed, some modes can be very well damped and thus, no resonances occur [72].

Figure 3.9 shows the two first critical speeds obtained by ANSYS 3D FEM. The first critical speed (cylindrical whirl) occurs at 4598 Hz (276 krpm) and the second critical speed (conical whirl) occurs at 7999 Hz (480 krpm). These values are compared with measurements in Chapter 6.

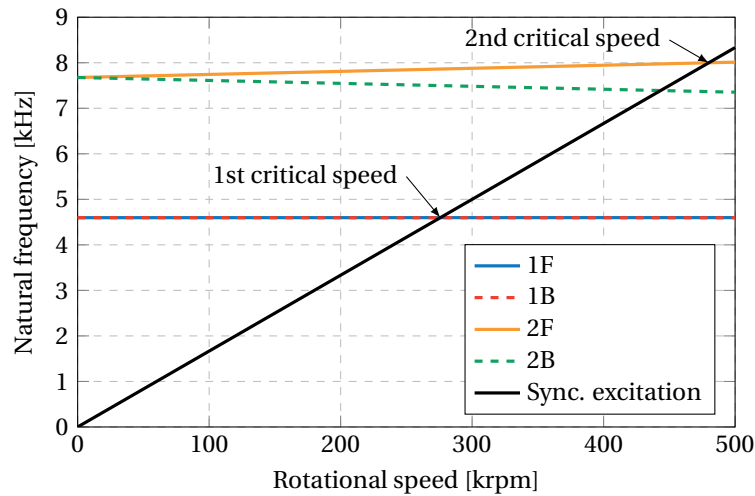


Figure 3.8 – Campbell diagram obtained by ANSYS 3D FEM.



(a) Cylindrical whirl at  $f_{1F} = 4598$  Hz.



(b) Conical whirl at  $f_{2F} = 7999$  Hz.

Figure 3.9 – Critical speeds computed by ANSYS 3D FEM.

### 3.4 Windage losses

Windage losses represent an important part of the total losses in VHS machines and have the highest rate of increase with respect to the rotational speed [12]. Indeed, the windage losses created by a cylindrical rotor spinning in a coaxial stator, as it can be seen in Figure 3.10, are proportional to the cube of rotational velocity  $\Omega$  according to

$$P_{\text{windage}} = \pi c_f \rho \Omega^3 r_{\text{eo}}^4 L_\delta, \quad (3.25)$$

where  $\rho$  is the density of the fluid in the mechanical airgap,  $L_\delta$  the axial length of this airgap (in the direction of the  $z$ -axis),  $r_{\text{eo}}$  the outer radius of the enclosure and  $c_f$  is called the friction coefficient. Windage losses models determine that friction coefficient by experimental measurements. It depends on dimensionless numbers such as the Couette-Reynolds number or the Taylor number. These numbers are independent of the scale of the machine and give an information about the state of the fluid flow in the airgap.

Because of the no-slip condition at a solid-fluid interface [77], a flow in the airgap is created when the rotor starts running. This flow is first laminar, then as the speed of the rotor increases, inertia forces overpass viscous forces and Taylor vortices, which are a pattern of regular vortices in the axial direction, start to appear. When the speed increases even more, the flow becomes fully turbulent [78]. Between laminar and fully turbulent states, the flow is defined as transitional.

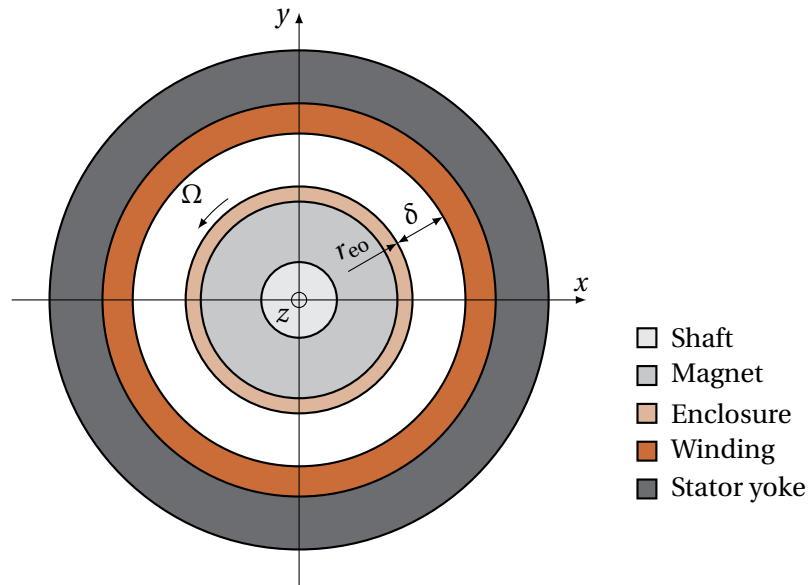


Figure 3.10 – Cross-section giving the geometry for the windage losses model.

### Chapter 3. Mechanical modelling

---

A lot of empirical models exist and one can mention the most encountered in literature:

- Daily and Nece (1960) [79],
- Yamada (1962) [80],
- Mack (1967) [81],
- Vrancik (1968) [82],
- Bilgen and Boulos (1973) [83],
- Awad and Martin (1998) [84].

They are also analysed in [12, 24, 38]. These models have been established in a specific context, for specific applications, for a specific range of Couette-Reynolds numbers. Some take into consideration axial flows and rotor or stator grooves. Some have been experimented with fluid or gas. Some even include a roughness coefficient for the outer surface of the rotor. For all these reasons, they give various estimations of the losses. Many of these models are used in research, but merely a few are validated [85]. Chapter 6 gives an experimental method to determine the windage losses. Subsequently, an existing model corresponding to the application can be selected.

It turns out that, for the prototype tested in Chapter 6, Mack's model [81] matches measurements well. According to Mack, the friction coefficient can be calculated as

$$c_f \begin{cases} = \frac{1.8}{Re} \frac{(r_{eo} + \delta)^2}{(r_{eo} + \delta)^2 - r_{eo}^2} \left( \frac{\delta}{r_{eo}} \right)^{-0.25} & : Ta \leq 41.2, \\ \propto Ta^{-0.2} & : Ta > 400, \end{cases} \quad (3.26)$$

where  $\delta$  is the thickness of the airgap. The Couette-Reynolds number is given by

$$Re = \frac{\Omega r_{eo} \delta}{\nu}, \quad (3.27)$$

and the Taylor number by

$$Ta = \frac{\Omega r_{eo} \delta}{\nu} \sqrt{\frac{\delta}{r_{eo}}}, \quad (3.28)$$

where  $\nu$  is the kinematic viscosity of the fluid in the airgap. In (3.26),  $\propto$  means proportional to, i.e.  $c_f = c_f(Ta = 41.2) Ta^{-0.2}$ . The Couette-Reynolds number can be seen as the ratio between inertia and viscous forces [38]. The flow is considered as laminar for  $Ta < 41.2$ . When the Taylor number is greater than 400, the flow is fully turbulent [24]. In between, lies the transitional flow. In practice, one considers a fully turbulent flow for  $Ta > 41.2$  in the calculations [86].

The kinematic viscosity of the fluid in the airgap is calculated as

$$\nu = \frac{\mu}{\rho}, \quad (3.29)$$

where  $\mu$  and  $\rho$  are respectively the dynamic viscosity and the density of the fluid. Both are influenced by pressure and temperature, but at moderate pressure, dynamic viscosity depends uniquely on temperature. To deal with the effect of temperature, the dynamic viscosity can be approximated by the Sutherland's law [87], that is

$$\mu = \mu_0 \left( \frac{T_0 + C}{T + C} \right) \left( \frac{T}{T_0} \right)^{3/2}, \quad (3.30)$$

where  $\mu_0$  is the dynamic viscosity of the gas at temperature  $T_0$ ,  $C$  is the Sutherland temperature and  $T$  is the absolute temperature of the gas. Temperatures are in Kelvin.

The density of the gas can be approximated by the ideal gas law

$$\rho = \frac{PM}{RT}, \quad (3.31)$$

where  $P$  is the absolute pressure of the gas,  $M$  is the molar mass of the gas and  $R$  is the ideal gas constant. The values of the aforementioned constants are given in the Nomenclature.

Windage losses for the prototype are given in Figure 3.11. The fluid in the airgap is air and the dimensions of the prototype are given in Table 6.1. The transitional flow begins at 50 krpm ( $Ta = 41.2$ ). Before that, losses are insignificant. The flow would be fully turbulent at 450 krpm ( $Ta = 400$ ).

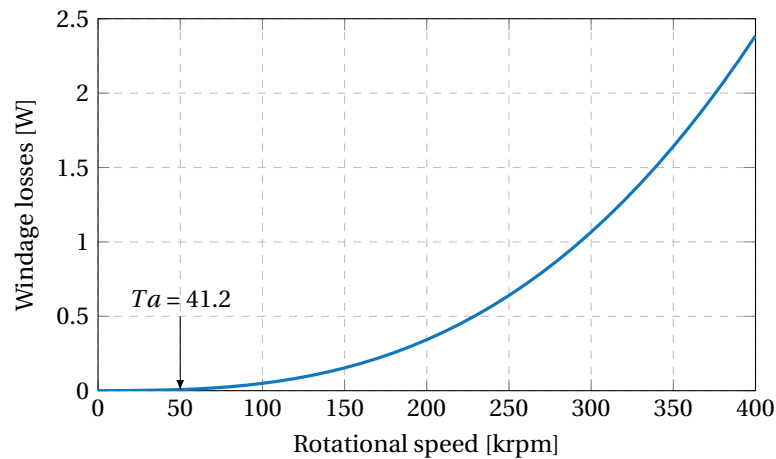


Figure 3.11 – Windage losses for the prototype according to Mack's model.

### 3.5 Ball bearing losses

Ball bearing losses also represent a very important part of the total losses in VHS machines [35]. Friction between the balls and the raceways or the retainer results in energy loss. The type and the quantity of lubricant is of great importance. In addition, the ageing of the ball bearings, the temperature, the preload, the operating load and the unbalance of the rotor have an influence.

For ball bearings running at moderate speed, empirical formulae based on laboratory testing are available [28]. Unfortunately, for very high speed applications [36, 88], there is little documentation in the literature, as pointed out in [37] and thus, ball bearing losses are measured most of the time.

Ball bearing losses can be modelled empirically by

$$P_{\text{bearings}} = c_{\text{bearings1}} \Omega^{c_{\text{bearings2}}}, \quad (3.32)$$

where  $\Omega$  is the rotational speed of the rotor and  $c_{\text{bearings1}}$  and  $c_{\text{bearings2}}$  are coefficients obtained by regression. In Chapter 6, an experimental method is proposed to evaluate these losses.

### 3.6 Conclusion

Mechanical modelling is intrinsic to the design of VHS machines. The very high speed and the temperatures induce mechanical stresses in the rotor that can be destructive, especially for permanent magnets. An innovative and very complete 3D analytical model capable of computing the stresses in the shaft, the magnet and the enclosure has been presented. It is valid for both cylinder and disc shaped rotors, as well as hollow and solid magnet rotors and takes into account the effect of thermal stresses. The von Mises failure criterion has been proposed to ensure the mechanical strength throughout the speed and temperature range. The model has been validated with 3D FEM and its limitations have been discussed.

VHS machines usually operate at overcritical speed. Accordingly, critical speeds have to be known so that none of them lie near the operating speed range. The rotor, including the ball bearings, has been modelled with 3D FEM and the first two critical speeds have been determined. They are experimentally compared in Chapter 6.

The very high speed is also responsible for creating mechanical losses, which represent a significant part of the total losses. The flow in the airgap created by the rotation of the rotor causes windage losses. Many empirical windage losses models exist and give various estimations. Furthermore, very few of them are validated in the literature. The chapter has presented the model devised by Mack. Indeed, measurements in Chapter 6 demonstrate that this model is adapted for the prototype. Ball bearings are also an important part of the total losses and a model has been presented in this chapter.



## 4 Electromagnetic modelling

### Contents

---

<b>4.1 Introduction . . . . .</b>	<b>42</b>
<b>4.2 Geometry and electromagnetic properties . . . . .</b>	<b>43</b>
<b>4.3 Magnetic quantities . . . . .</b>	<b>44</b>
4.3.1 Vector potential . . . . .	44
4.3.2 Magnetic flux density . . . . .	45
4.3.3 Magnetic flux linkage and back EMF voltage . . . . .	47
4.3.4 Electromagnetic torque . . . . .	48
4.3.5 Validation of the models . . . . .	48
<b>4.4 Winding losses . . . . .</b>	<b>50</b>
4.4.1 Component due to the current . . . . .	51
4.4.2 Component due to the permanent magnet for round wires . . . . .	51
4.4.3 Component due to the permanent magnet for rectangular wires . . . . .	53
<b>4.5 Iron losses . . . . .</b>	<b>57</b>
<b>4.6 Rotor losses . . . . .</b>	<b>58</b>
<b>4.7 Conclusion . . . . .</b>	<b>59</b>

---

Publication of the author related to this chapter:

- Guillaume Burnand and Yves Perriard. Very-High-Speed Miniaturized Permanent Magnet Motors: Modeling and Experimental Validation. In *2019 IEEE Energy Conversion Congress and Exposition (ECCE)*, pages 1–7. IEEE, October 2019.

### 4.1 Introduction

Electromagnetic modelling is based upon the magnetic vector potential. It further enables the computation of the magnetic flux density and several losses in the machine. The vector potential is especially important in the airgap, as it interacts with the winding and serves to compute the back EMF voltage and the electromagnetic torque. Section 4.2 presents the geometry and the electromagnetic properties of the models used in this chapter. Section 4.3 gives the equations for the magnetic vector potential and flux density in the airgap for a one pole pair diametrically magnetised cylindrical PM machine with a slotless winding.

Besides traditional losses encountered in BLDC machines, the very high rotational speed of the rotor and, de facto, the high electrical frequencies associated, produce additional losses. The electromagnetic losses can be divided into winding losses, iron losses and rotor losses. Unlike mechanical losses, most of electromagnetic losses can be calculated analytically in slotless machines. To this end, an essential hypothesis has to be made: the magnetic field produced by the PM is much stronger than the one produced by the stator currents in slotless machines. Indeed, the coils are surrounded by air which has a high magnetic reluctance. This hypothesis allows the models to be simplified, while keeping a very good accuracy and saving computational time.

Winding losses are presented in Section 4.4. In addition to Joule losses, they consist of the skin effect and proximity effect losses created by the high electrical frequencies [89]. Moreover, the windings of slotless PM machines have induced eddy current losses due to the time-varying magnetic field of the rotor. The computation of these losses for round section conductors can be found in [90–93]. As for rectangular section conductors, they are less encountered in literature, but nonetheless used in slotless machines. Thereby, the chapter contributes to fill the gap by presenting a model for the computation of induced eddy current losses by the rotation of the PM in rectangular section wires.

Well known models such as Steinmetz's [94] or Jordans's [95] allow the estimation of iron losses. They take into account the hysteresis and eddy current losses as function of the frequency, the peak magnetic flux density and some empirical coefficients. Based on these models, a solution is proposed to compute the iron losses due to the rotation of the PM in Section 4.5.

Finally, a discussion is made about rotor losses in Section 4.6. They are created by time-varying magnetic fields created by stator windings which induce eddy currents in the sleeve, the magnet and possibly the shaft. Rotor losses in slotted machines are researched because they are most of the time significant [96]. In slotless structures, they should be considered, because the heat generated in the rotor is difficult to dissipate, but they are most of the time very small compared to the total losses [12].

## 4.2 Geometry and electromagnetic properties

Electromagnetic models presented here are based on the geometry given in Figure 4.1. It is a one pole pair ( $p = 1$ ) diametrically magnetised cylindrical PM machine with a slotless winding. The index s stands for shaft, m for magnet, c for coil, y for yoke, i for inner and o for outer. It may happen (for manufacturing reasons) that the shaft does not pass through the magnet. Consequently, models are adapted by tending the inner radius of the magnet  $r_{mi}$  to zero in the following equations.

The permanent magnet is defined by its magnetic properties:

- Remanence:  $B_r$  [T]
- Relative permeability:  $\mu_r$  [-]

The remaining parameters are:

- Mechanical angle of the rotor:  $\theta$  [rad]
- Rotational speed:  $\Omega$  [rad/s]

The mechanical angle of the rotor is chosen to be the same as the magnetisation angle of the PM, as given by the referential in Figure 4.1.

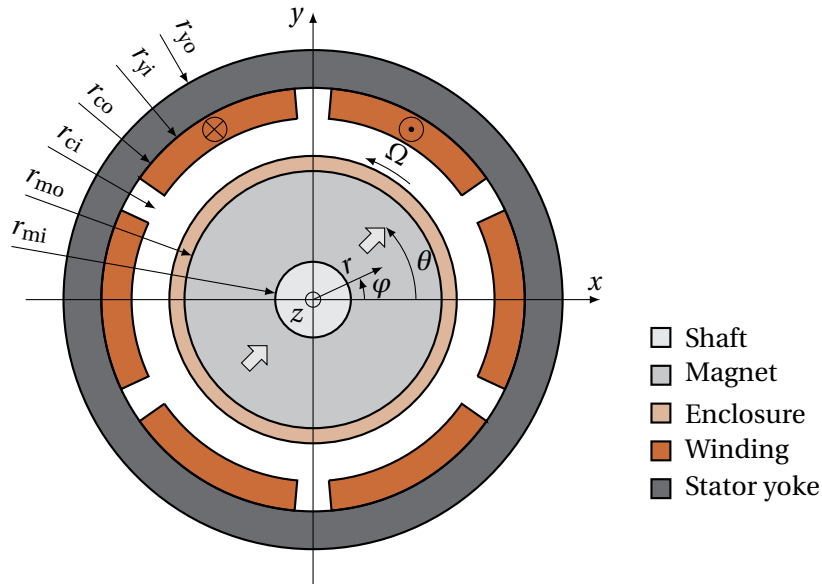


Figure 4.1 – Cross-section giving the geometry and the dimensions of electromagnetic models. The rotor is made of a one pole pair ( $p = 1$ ) diametrically magnetised cylindrical permanent magnet and the stator is slotless.

### 4.3 Magnetic quantities

#### 4.3.1 Vector potential

The vector potential  $\vec{A}$  is defined by

$$\vec{B} = \nabla \times \vec{A}, \quad (4.1)$$

and

$$\vec{E} = - \left( \nabla V + \frac{\partial \vec{A}}{\partial t} \right), \quad (4.2)$$

where  $\vec{B}$  is the magnetic flux density vector,  $\vec{E}$  the electric field vector and  $V$  the electric scalar potential. For a one pole pair diametrically magnetised cylindrical PM slotless machine, the axial component of the vector potential in the airgap [97] can be calculated as

$$A_{\delta z}(r, \varphi) = c_{\delta} \left( r + \frac{r_{yi}^2}{r} \right) \sin(\varphi - \theta), \quad (4.3)$$

where

$$c_{\delta} = \frac{B_r r_{mo}^2 (r_{mi}^2 - r_{mo}^2)}{\mu_r (r_{mi}^2 + r_{mo}^2) (r_{mo}^2 - r_{yi}^2) + (r_{mi}^2 - r_{mo}^2) (r_{mo}^2 + r_{yi}^2)}, \quad (4.4)$$

is a constant depending on the geometry and the properties of the PM. It is important to point out that the vector potential is purely sinusoidal in the airgap. In this model, the hypotheses are the following:

- the PM is diametrically magnetised and covers an entire magnetic pole,
- the magnetic field produced by the winding is not considered,
- the axial length of the model is considered as infinite (no end effects),
- the magnetic materials, including the PM, are linear (no saturation effect),
- the relative permeability of magnetic materials (the shaft and the yoke) is infinite.

The last two assumptions are justified by the fact that airgaps are large in slotless machines [98]. Figure 4.2 illustrates the equipotential lines of the axial component of the vector potential in the airgap, which are also the field lines of the magnetic flux density. The mechanical angle of the rotor equals  $\frac{\pi}{2}$ . The dimensions of the machine and the magnetic properties of the PM are those of the prototype presented in Chapter 6. The equations for the vector potential in the remaining parts of the machine can be found in [97].

The vector potential is further employed to compute the flux linkage (Section 4.3.3) as well as the induced eddy current losses in the winding (Section 4.4.3).

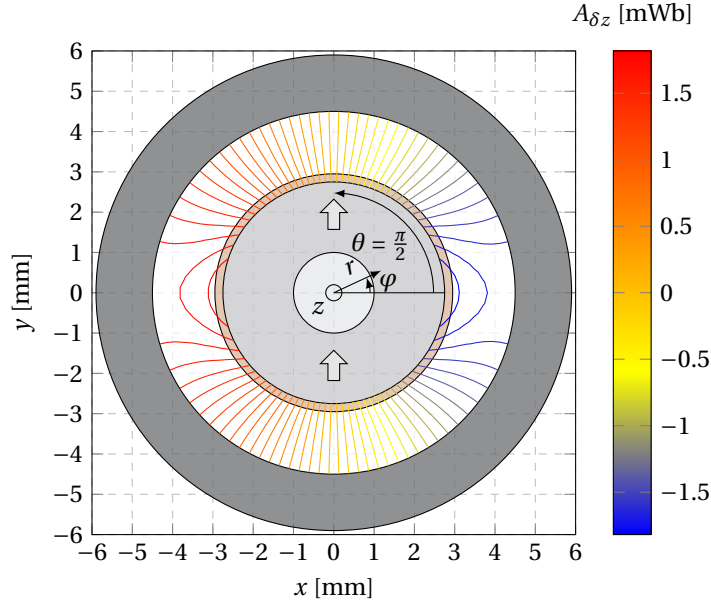


Figure 4.2 – Equipotential lines of the axial component of the vector potential in the airgap. The mechanical angle of the rotor is worth  $\frac{\pi}{2}$ .

#### 4.3.2 Magnetic flux density

The radial and tangential components of the magnetic flux density are obtained from (4.1). This gives, in cylindrical coordinates,

$$B_r = \frac{1}{r} \frac{\partial A_z}{\partial \varphi}, \quad (4.5)$$

$$B_\varphi = -\frac{\partial A_z}{\partial r}. \quad (4.6)$$

Applying (4.5) and (4.6) to (4.3) gives respectively the radial and tangential components of the magnetic flux density in the airgap for a one pole pair diametrically magnetised cylindrical PM slotless machine, that is

$$B_{\delta r}(r, \varphi) = c_\delta \left( 1 + \frac{r_{yi}^2}{r^2} \right) \cos(\varphi - \theta), \quad (4.7)$$

and

$$B_{\delta \varphi}(r, \varphi) = c_\delta \left( \frac{r_{yi}^2}{r^2} - 1 \right) \sin(\varphi - \theta). \quad (4.8)$$

The 2 equations show that the radial component is always bigger, in absolute value, than the tangential one. Under the same conditions as Figure 4.2, Figures 4.3 and 4.4 highlight the isolines of both components of the magnetic flux density. The radial component reaches its maximal value in the axis of magnetisation, whereas the tangential component has its maximal value perpendicularly to this axis.

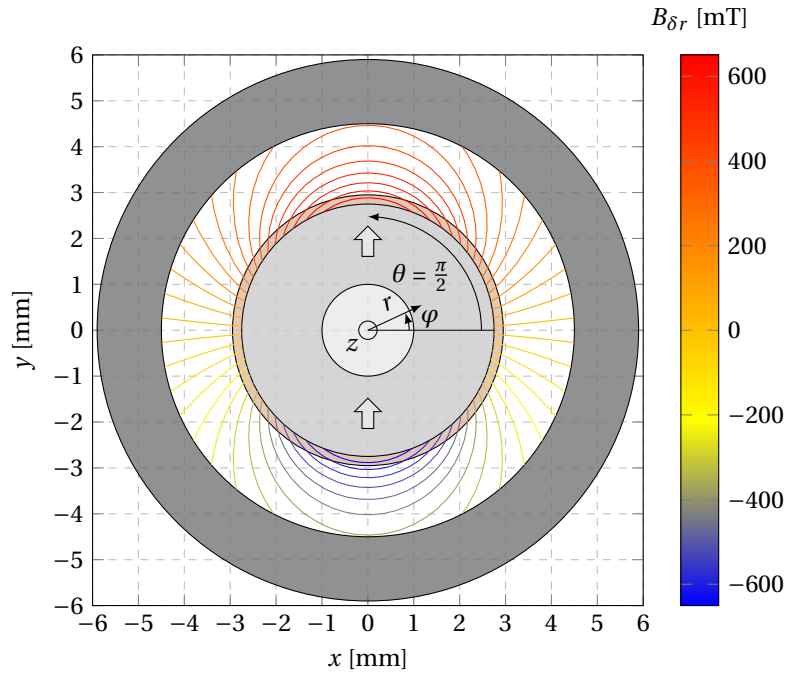


Figure 4.3 – Isolines of the radial component of the magnetic flux density in the airgap. The mechanical angle of the rotor is worth  $\frac{\pi}{2}$ .

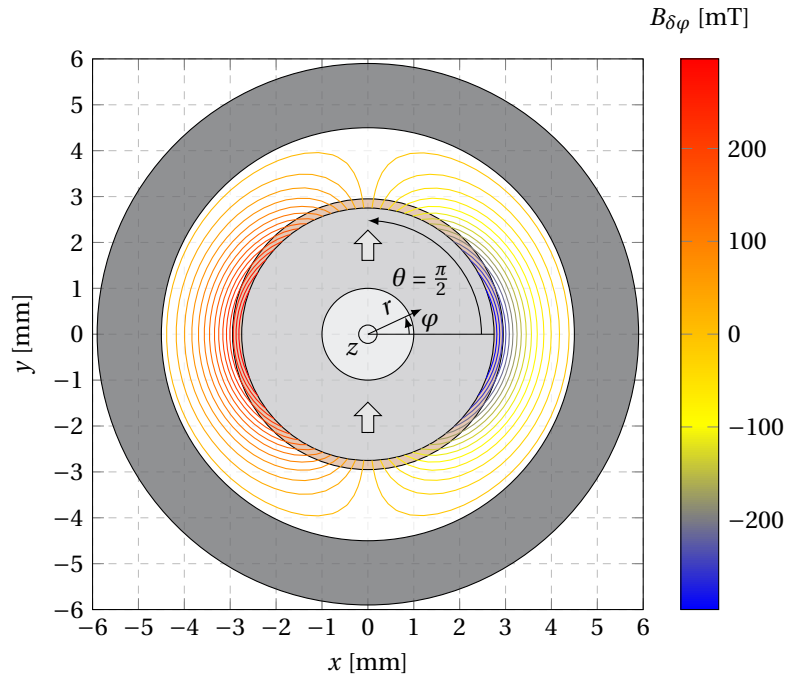


Figure 4.4 – Isolines of the tangential component of the magnetic flux density in the airgap. The mechanical angle of the rotor is worth  $\frac{\pi}{2}$ .

The radial component is responsible for the production of the electromagnetic torque (Section 4.3.4), and both components are responsible for induced eddy current losses in the winding, as demonstrated in Section 4.4.3. As can be observed, one pole pair diametrically magnetised cylindrical PM slotless machines have a purely sinusoidal magnetic flux density distribution in the airgap. Not only does the absence of harmonics reduce the induced losses, it also creates purely sinusoidal back EMF voltage in the winding (in the absence of saturation).

The peak magnetic flux density in the stator yoke, that will aim to compute iron losses in Section 4.5, can also be obtained analytically [97] by

$$\hat{B}_y = \frac{2c_\delta}{k_s} \frac{(r_{yo}^2 + r_{yi}^2)}{(r_{yo}^2 - r_{yi}^2)}, \quad (4.9)$$

where  $k_s$  is the stacking factor of the laminated stator sheets.

Analytical equations of the vector potential and the magnetic flux density presented above, which consider magnetic materials with an infinite permeability, are very accurate when compared to FEM simulations taking into account a finite permeability. However, when saturation occurs, the models lack accuracy in magnetic materials and FEM modelling must be considered.

#### 4.3.3 Magnetic flux linkage and back EMF voltage

With (4.1) and by means of the Stokes' theorem, the magnetic flux linkage  $\Psi$  through a coil can be rewritten as

$$\Psi = \iint_{\Sigma} \vec{B} \cdot d\vec{S} = \iint_{\Sigma} \nabla \times \vec{A} \cdot d\vec{S} = \oint_{\partial\Sigma} \vec{A} \cdot d\vec{l}, \quad (4.10)$$

where  $d\vec{S}$  is an infinitesimal surface vector,  $d\vec{l}$  an infinitesimal line vector,  $\Sigma$  the surface bounded by the coil,  $\partial\Sigma$  the boundary of  $\Sigma$ , that is the path of the coil. Depending on the complexity of the geometry and shape of the coils, (4.10) can be calculated by numerical integration.

Given the sinusoidal nature of the magnetic flux linkage, with respect to the rotation of the rotor in a one pole pair diametrically magnetised PM slotless machine, the back EMF voltage in one coil can be assumed to be equal to

$$u(t) = \hat{\Psi}\Omega \cos(\Omega t + \alpha), \quad (4.11)$$

where  $\hat{\Psi}$  is the peak flux linkage obtained with (4.10) for some mechanical angle of the rotor giving the maximal flux in the coil, and  $\alpha$  is the phase of the voltage which depends on the relative position of the coil. The speed or back EMF constant can be further deduced from (4.11) according to the connections of phases [48].

### 4.3.4 Electromagnetic torque

The electromagnetic torque can be obtained by computing Laplace forces as the interaction of the radial magnetic flux density created by the PM and the current density  $J$  flowing in the coil [3]. The useful electromagnetic torque (creating a rotational motion) for one coil is then

$$T'_{\text{em}}(\theta) = \int_{V_c} r J B_{\delta r} dV, \quad (4.12)$$

with  $r$  the radius from the centre of rotation to the coil and  $V_c$  the volume of the coil.

### 4.3.5 Validation of the models

#### 3D FEM model

In order to validate the models, the prototype used in Chapter 6 is modelled with 3D FEM as pictured in Figure 4.5. The dimensions and properties of the materials are given in Table 6.1. Non-meshed coils are employed, because induced eddy current losses are not computed here.

#### Vector potential and magnetic flux linkage

The analytical flux linkage is obtained by numerical integration of (4.10) and by assuming that the vector potential in the airgap drops to zero beyond the axial length of the PM. The referential for the mechanical angle of the rotor is the one defined in Figure 4.1, where the coil is at 12 o'clock.

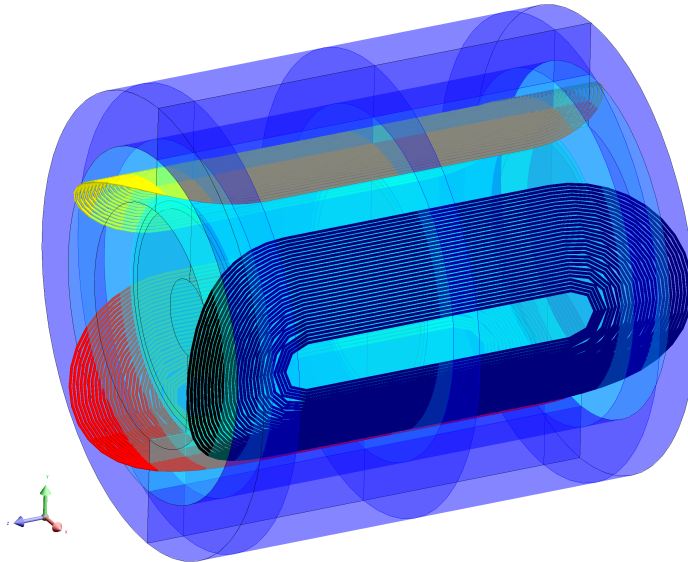


Figure 4.5 – 3D FEM model with non-mesh coils in Altair Flux.



Figure 4.6 compares the value of the magnetic flux linkage in one coil obtained analytically and by 3D FEM. The error is only 4.3 % and is due to the consideration of saturation and end effects by 3D FEM, lowering the value. The assumption of a sinusoidal flux distribution in the airgap and the equation of back EMF voltage (4.11) are experimentally validated in Chapter 6.

#### Magnetic flux density and electromagnetic torque

The analytical electromagnetic torque is calculated similarly thanks to (4.12) with an arbitrary current equal to 1 A. The same error of 4.3 % can be visualised in Figure 4.7. In both graphs hereunder, the quadrature between the magnetic flux linkage and the electromagnetic torque can be seen. In addition, the numerical values are the same (due to the sinusoidal nature of the vector potential in the airgap).

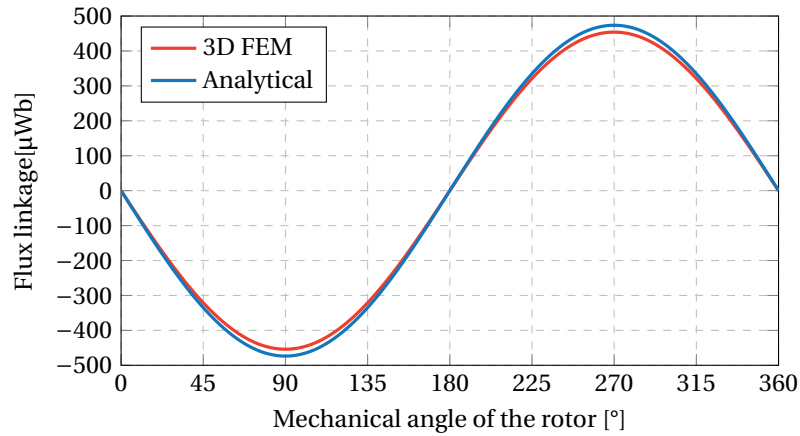


Figure 4.6 – Comparison of the magnetic flux in one coil between analytical and 3D FEM models.

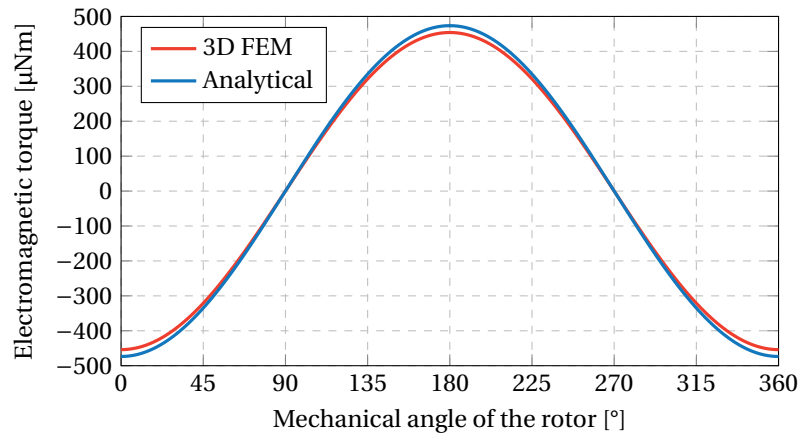


Figure 4.7 – Comparison of the electromagnetic torque in one coil between analytical and 3D FEM models.

## 4.4 Winding losses

Winding losses consist of the Joule losses due to stator currents, the skin effect that concentrates the current density at the outer border of the wires and the proximity effect resulting from perturbation in between each wire [89]. These last two effects result in an increase of the resistance of the wire and occur particularly when the electrical frequency of the stator is high. Hence, the aforementioned losses are created by the current and its frequency.

In the case of slotless machines, the temporal variation of the magnetic flux density, created by the rotation of the PM, induces additional eddy current losses in the stator winding [35]. Therefore, the total winding losses can be obtained by

$$P_{\text{winding}} = \underbrace{P_{\text{Joule}} + P_{\text{skin}} + P_{\text{prox}}}_{\text{due to the current}} + \underbrace{P_{\text{windingPM}}}_{\text{due to the PM}}, \quad (4.13)$$

where  $P_{\text{Joule}}$  represents the conduction Joule losses,  $P_{\text{skin}}$  the skin effect losses,  $P_{\text{prox}}$  the proximity effect losses and  $P_{\text{windingPM}}$  the losses due to eddy currents induced by the PM. Valuable information about the analytical computation of losses in conductors can be found in [90–93].

Nevertheless, in slotless PM machines, the magnetic flux density in the airgap is overwhelmingly due to the permanent magnet itself. Given that the magnetic flux density created by the currents flowing in the winding is low in comparison, proximity effect losses can usually be neglected [12].

The section of conductors in electrical machines is traditionally either circular or rectangular. In both cases, the higher the rotational speed (and proportionally the electrical frequency), the lower the section must be in order to limit eddy current losses. However, reducing the section of conductors increases Joule losses. The skin depth of a conductor is used as a rule of thumb for sizing the wire (the dimensions of the wire have to be smaller than the skin depth) and is calculated as

$$\delta_{\text{skin}} = \sqrt{\frac{2}{\omega \sigma \mu}}, \quad (4.14)$$

where  $\omega$  is the electrical angular frequency and  $\sigma$  and  $\mu$  are respectively the conductivity and the magnetic permeability of the conductor. The skin depth in copper for frequencies encountered in VHS machines is pictured in Figure 4.8.

Litz-wire is commonly used in VHS machines [35]. It is made of tiny round section strands electrically insulated from one another and twisted to make the wire. Rectangular section wires offer an interesting alternative and are used extensively in slotless machines for their higher filling factor and their simplicity of manufacturing in comparison to Litz-wire. Their benefits and drawbacks are discussed in detail in Chapter 7. As yet, very few losses models are available for these windings.

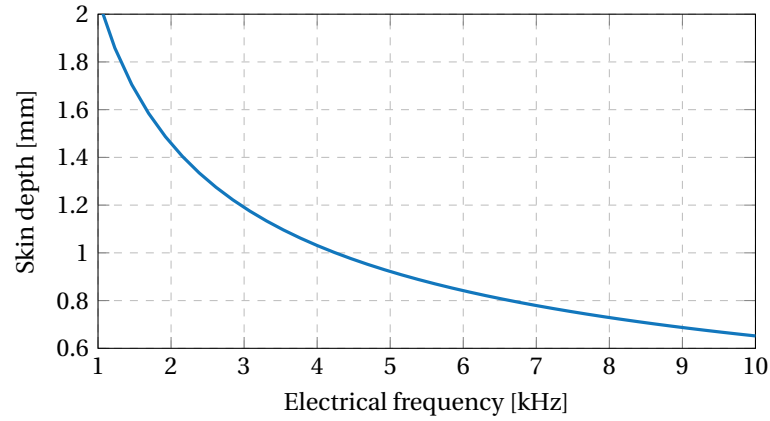


Figure 4.8 – Skin depth of copper versus typical frequencies encountered in very high speed machines.

#### 4.4.1 Component due to the current

##### Joule losses and skin effect losses

Joule losses, without considering skin effect losses, are obtained with

$$P_{\text{Joule}} = 3\rho V_c J^2, \quad (4.15)$$

where  $\rho$  is the electrical resistivity of the coil,  $V_c$  is the volume of one coil and  $J$  is the current density. Skin effect losses can be determined analytically from [90, 91].

Equation (4.15) is appropriate during the design phase. However, for measurements, another equation is more suitable. Given that the skin effect results in an increase of the DC resistance, Joule and skin effect losses can be combined to give

$$P_{\text{Joule+skin}} = \frac{3}{2} R_{\text{ph-ph}} I_1^2, \quad (4.16)$$

where  $R_{\text{ph-ph}}$  is the phase-to-phase resistance taking into account the effect of the frequency (which can be measured with an LCR meter) and  $I_1$  is the RMS line current.

#### 4.4.2 Component due to the permanent magnet for round wires

Eddy current losses, induced by a sinusoidal and homogeneous pulsating magnetic flux density in a round conductor, are analysed in [90] and [93]. An exact analytical solution is obtained and the eddy current losses induced by the PM in a round section wire of diameter  $d_w$ , per unit length, can be calculated as

$$P'_{\text{wirePM}} = \frac{G(\gamma)\hat{B}_w^2}{\sigma\mu^2}, \quad (4.17)$$

where  $\hat{B}_w$  is the peak magnetic flux density in the wire (assumed to be homogeneous due to the relatively small size of the wire) caused by the PM and  $G(\gamma)$  is a function given by

$$G(\gamma) = 2\pi\gamma \frac{\text{Ber}_2(\gamma)\text{Ber}'(\gamma) - \text{Bei}_2(\gamma)\text{Bei}'(\gamma)}{\text{Ber}^2(\gamma) + \text{Bei}^2(\gamma)}. \quad (4.18)$$

In this function,  $\text{Ber}$  and  $\text{Bei}$  are the *Kelvin functions* of the first kind (see Appendix A) and

$$\gamma = \frac{d_w}{\delta_{\text{skin}}\sqrt{2}}, \quad (4.19)$$

is called the relative penetration.

It remains to compute the term  $\hat{B}_w$  in (4.17). Given that the position of each wire in the airgap of a slotless machine cannot be precisely known, the mean value of the peak magnetic flux density in the airgap has to be calculated. First, the magnitude of the magnetic flux density in the airgap, by means of (4.7) and (4.8), is

$$\|\vec{B}_\delta(r, \varphi)\| = \sqrt{B_{\delta r}^2(r, \varphi) + B_{\delta \varphi}^2(r, \varphi)} = c_\delta \sqrt{1 + 2\frac{r_{yi}^2}{r^2} \cos(2(\varphi - \theta)) + \frac{r_{yi}^4}{r^4}}, \quad (4.20)$$

and it gets its maximal value when  $\varphi = \theta$ , that is the  $y$ -axis in both Figures 4.3 and 4.4 (magnetisation axis). Afterwards, the mean squared value of the peak magnetic flux density in the airgap is given by

$$\overline{B_{\delta \max}^2} = \frac{c_\delta^2}{r_{\text{co}} - r_{\text{ci}}} \int_{r_{\text{ci}}}^{r_{\text{co}}} \left(1 + \frac{r_{yi}^2}{r^2}\right)^2 dr = \frac{c_\delta^2}{r_{\text{co}} - r_{\text{ci}}} \left( (r_{\text{co}} - r_{\text{ci}}) + 2r_{yi}^2 \left( \frac{1}{r_{\text{ci}}} - \frac{1}{r_{\text{co}}} \right) + \frac{r_{yi}^4}{3} \left( \frac{1}{r_{\text{ci}}^3} - \frac{1}{r_{\text{co}}^3} \right) \right). \quad (4.21)$$

Finally, eddy current losses for a coil of  $N_t$  turns and per unit length are

$$P'_{\text{windingPM}} = N_t \frac{G(\gamma)\overline{B_{\delta \max}^2}}{\sigma\mu^2}. \quad (4.22)$$

### 4.4.3 Component due to the permanent magnet for rectangular wires

#### Geometry and parameters

In addition to the properties described in Section 4.2, the model for the computation of eddy current losses in the stator winding induced by the magnetic flux density of the PM includes:

- Electrical conductivity of the coil:  $\sigma$  [S/m]
- Number of turns for one coil:  $N_t$  [-]

Only a single rectangular section wire is considered as visible in Figure 4.9. The wire is specified by its width  $w_w$ , its height  $h_w$  and its position in the airgap along the  $y$ -axis.

The model does not consider the magnetic field created by the induced currents. It is therefore based on a first order vector potential formulation. The induced current density all over its section is calculated. Then, by integration over a time period and, taking into account the number of turns and coils, the total eddy current losses are obtained. As a result, the proximity effect in between the turns is not taken into account.

Both hypothesis can be justified by the fact that the magnetic flux density created by induced currents is much lower than the one produced by the PM [99]. Besides, if the skin depth of the conductor is equal to or bigger than the dimensions of the wire, the use of the diffusion equation (second order vector potential formulation) is not necessary.

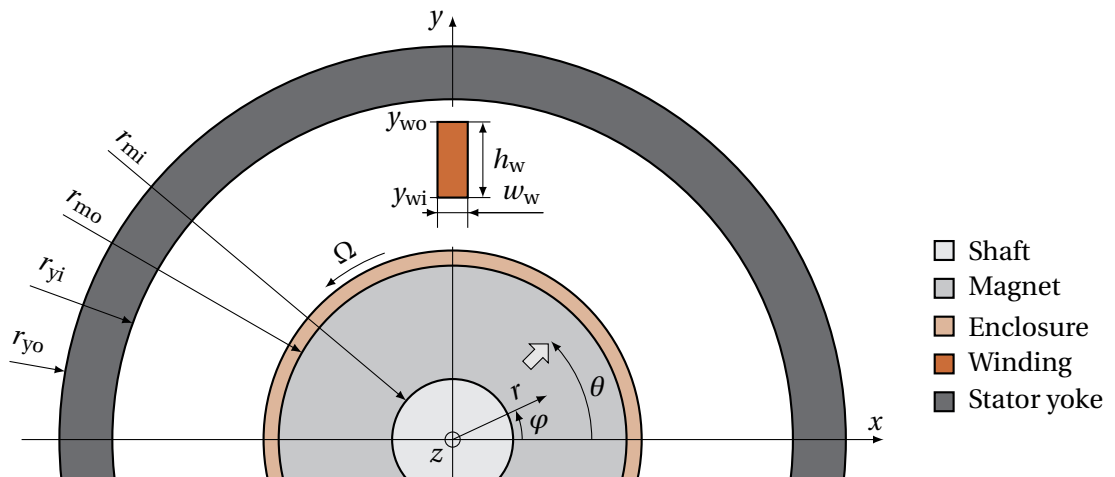


Figure 4.9 – Cross-section giving the geometry and the dimensions of the model for the computation of eddy current losses in the winding induced by the rotation of the PM. The PM has one pole pair and is diametrically magnetised.

### Induced current density

Introducing (4.2) in Ohm's law

$$\vec{E} = \rho \vec{J}, \quad (4.23)$$

gives the general equation for the induced current density

$$\vec{J} = -\sigma \left( \nabla V + \frac{\partial \vec{A}}{\partial t} \right), \quad (4.24)$$

where  $\vec{J}$  is the current density vector, and  $\rho$  and  $\sigma$  are respectively the resistivity and the conductivity of the medium. With the referential of Figure 4.9 and the hypotheses in Section 4.3.1, the vector  $\vec{J}$  reduces to a scalar value  $J_z$  in the axial direction. Introducing  $\theta = \Omega t$ , the time derivative of the vector potential in (4.24) is calculated from (4.3) leading to

$$\frac{\partial A_{\delta z}(r, \varphi)}{\partial t} = -\Omega c_\delta \left( r + \frac{r_{yi}^2}{r} \right) \cos(\varphi - \Omega t). \quad (4.25)$$

For the sake of simplicity, the time derivative can be rewritten in Cartesian coordinates and, with the help of trigonometric identities, it becomes

$$\frac{\partial A_{\delta z}(x, y)}{\partial t} = -\Omega c_\delta \left( 1 + \frac{r_{yi}^2}{x^2 + y^2} \right) (x \cos(\Omega t) + y \sin(\Omega t)). \quad (4.26)$$

It remains to define the gradient of the electric scalar potential in (4.24). Considering the wire as an open-circuit conductor (without an external electrical potential) is to say that the surface integral of induced current density on the  $x$ - $y$  plane of the wire is equal to zero

$$\int_{y_{wi} - \frac{w_w}{2}}^{y_{wo} + \frac{w_w}{2}} \int \nabla V(z) + \frac{\partial A_{\delta z}(x, y)}{\partial t} dx dy = 0. \quad (4.27)$$

From there, the gradient of the potential, which is constant on the  $x$ - $y$  plane, is deduced (see details in Appendix B) and the induced current density in a single wire is obtained by

$$J_z(x, y, t) = \sigma \Omega c_\delta \left( \left( 1 + \frac{r_{yi}^2}{x^2 + y^2} \right) (x \cos(\Omega t) + y \sin(\Omega t)) - c_w \sin(\Omega t) \right), \quad (4.28)$$

with

$$c_w = \frac{1}{w_w h_w} \left( \frac{1}{2} w_w (y_{wo}^2 - y_{wi}^2) + 2 r_{yi}^2 \left( \frac{w_w}{4} \ln \frac{w_w^2 + 4 y_{wo}^2}{w_w^2 + 4 y_{wi}^2} + y_{wo} \arctan \frac{w_w}{2 y_{wo}} - y_{wi} \arctan \frac{w_w}{2 y_{wi}} \right) \right), \quad (4.29)$$

a constant depending on the geometry.

Figure 4.10 illustrates the induced current density in a single wire for 3 different positions of the rotor at a rotational speed of 400 krpm. The dimensions and the position of the wire correspond to the ones in the prototype presented in Chapter 6. In this particular case, the skin depth of copper is equal to  $827 \mu\text{m}$  at 6.6 kHz (400 krpm) and the height of the wire is equal to  $900 \mu\text{m}$ , which justifies the first order vector potential formulation.

When the mechanical angle of the rotor  $\theta = 0^\circ$ , flux lines of the magnetic flux density are horizontal in Figure 4.10a. Consequently, merely the tangential component of  $\vec{B}$  is the source of induced currents. In this case, the values of  $J_z$  are the lowest because they are limited by the width of the wire. Conversely, when  $\theta = 90^\circ$  as in Figure 4.10c, the radial component of  $\vec{B}$  is responsible for the induced currents. In this case, the values of  $J_z$  are the highest because the height of the wire is several times its width.

### Computation of losses

Finally, the eddy current losses induced in the winding by the PM, per unit length and for one coil of  $N_t$  turns, are calculated by the following integral

$$P'_{\text{windingPM}} = \frac{2N_t}{\sigma T} \int_0^T \int_{S_w} J_z^2(x, y, t) dS dt, \quad (4.30)$$

where  $S_w$  is the section of the wire and  $T$  is the time period. This equation does not have an analytical solution (at least for the surface integral) and must be computed numerically.

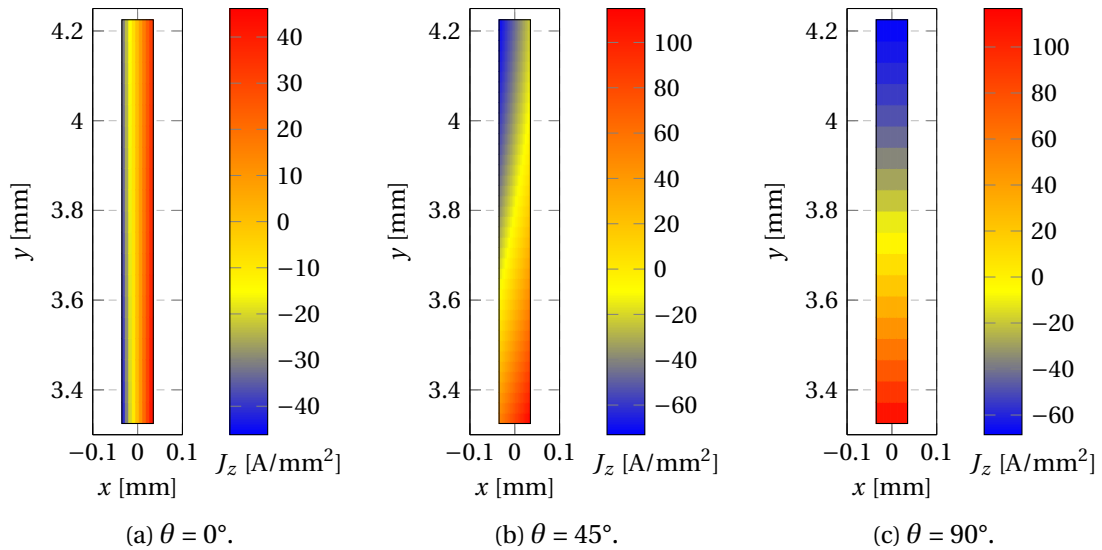


Figure 4.10 – Induced current density in the wire with respect to several values of the angle of the rotor at 400 krpm.

### 2D FEM validation

Half a coil of 29 turns, which corresponds to the one in the prototype in Chapter 6, is modelled in 2D FEM as visible in Figure 4.11. The dimensions are given in Table 6.1. The transient FEM formulation deals with a second order equation for the potential vector, meaning that the magnetic field of induced currents is considered, as well as the proximity effect. It also considers the saturation effect in magnetic materials.

Figure 4.12 compares the eddy current losses between the analytical and FEM models in a winding made of 3 coils of 29 turns each (as in Figure 4.5). Just like eddy current losses in iron sheets, these losses scale with the square of rotational speed. The maximal error is 1.8%. Thereby, the hypothesis about the first order formulation of the vector potential is justified: the magnetic field produced by the PM is much higher than the one of the induced currents. An experimental validation of the model is presented in Chapter 6.

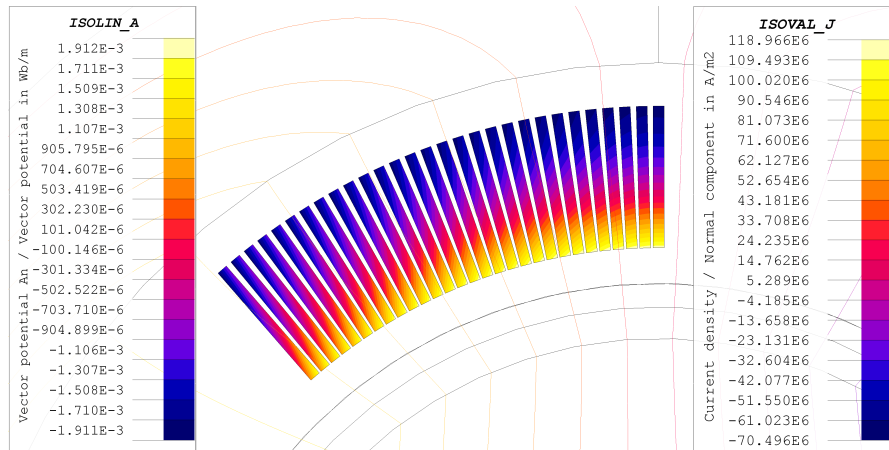


Figure 4.11 – Transient 2D FEM model highlighting the induced current density in half a coil of 29 turns due to the rotation of the PM (Altair Flux).

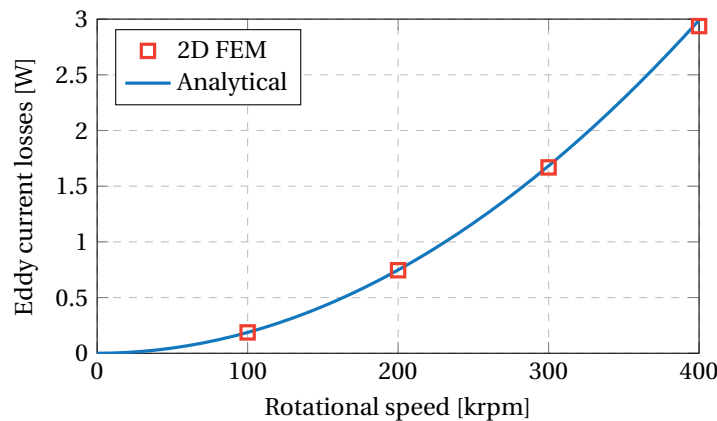


Figure 4.12 – Comparison of the eddy current losses induced in the winding by the rotation of the PM between analytical and 2D FEM models.



## 4.5 Iron losses

A time-varying magnetic field creates losses in a magnetic material. These losses are usually divided into 2 parts: hysteresis losses and eddy current losses [100]. From a macroscopic point of view, hysteresis losses represent the energy required for the magnetic moments in the medium to be oriented with the external magnetic field. They are proportional to the area of the hysteresis cycle and to the frequency of the magnetic field. Eddy current losses are created by induced currents due to the time-varying magnetic field in the core. They are proportional to the square of both the peak magnetic flux density and the frequency.

Iron losses can be calculated, per unit volume, given a peak magnetic flux density  $\hat{B}$  of frequency  $f$ , by the Steinmetz's equation [94] or by the Jordan's equation [95], respectively

$$P'_{\text{iron}} = c f^{\alpha} \hat{B}^{\beta}, \quad (4.31)$$

$$P'_{\text{iron}} = c_{\text{hyst}} f \hat{B}^2 + c_{\text{eddy}} f^2 \hat{B}^2, \quad (4.32)$$

where  $\alpha, \beta, c, c_{\text{hyst}}$  and  $c_{\text{eddy}}$  are empirical coefficients related to the material. These coefficients are generally given by manufacturers. They are valid in some frequency and temperature ranges, but also for a sinusoidal excitation and non-saturated materials [101]. Besides, manufacturing processes on the cores do have an influence on the magnetic properties [102]. Therefore, it may be preferable to measure the losses directly on the machine and subsequently to determine the coefficients as presented in Chapter 6.

The time-varying magnetic field is produced by the stator currents but also by the rotation of the permanent magnet. Again, the magnetic field produced by the magnet is much stronger than the one of the currents in slotless machines. Thus, iron losses due to the stator currents are negligible in most cases. Iron losses in the stator yoke due to the rotation of the PM can be empirically modelled by

$$P_{\text{ironPM}} = \pi(r_{\text{yo}}^2 - r_{\text{yi}}^2) L_{\text{PM}} k_s \left( c_{\text{iron1}} \Omega \hat{B}_y^2 + c_{\text{iron2}} \Omega^2 \hat{B}_y^2 \right), \quad (4.33)$$

where  $k_s$  is the stacking factor,  $c_{\text{iron1}}$  and  $c_{\text{iron2}}$  are coefficients obtained by regression,  $\hat{B}_y$  is the peak magnetic flux density in the stator yoke given by (4.9) and  $L_{\text{PM}}$  is the axial length of the PM<sup>1</sup>. Jordan's model turns out to be more appropriate than Steinmetz's for wide frequency ranges [103].

Iron losses can be reduced by choosing low loss materials like amorphous or nanocrystalline alloys [104] and by increasing the radial thickness of the stator yoke, which will reduce the peak magnetic flux density. However, this last point can be problematic with miniaturised machines, where the size is a limiting factor.

<sup>1</sup>The axial length of the stator is assumed to be longer than the axial length of the PM in order to avoid the induction of eddy current losses in ball bearings.

### 4.6 Rotor losses

Rotor losses are due to eddy currents induced by the magnetic field of the stator in the sleeve, the permanent magnet and possibly the shaft. These losses are most of the time insignificant with regard to the total losses of the machine. However, in some cases, it is important to take them into consideration since the losses produced in the rotor are not easy to dissipate. The heat is extracted most of the time by natural convection only. Indeed, a forced axial flow would increase even more windage losses [40]. If the machine operates in a vacuum, the heat cannot be extracted at all. Excessive temperature in the rotor would limit the mechanical strength of materials (see Section 3.2) and reduce the performance of the magnet.

Induced currents come from space harmonics due to stator slots openings (if any exist), the winding distribution and the magnetic field of the stator on one hand, and on the other hand, from time harmonics due to the pulse width modulation (PWM) of stator currents [96]. Losses due to the magnetic field of the stator and PWM harmonics are current dependant and thus, vary with the load [89].

Stator slots openings generate variations of the reluctance of the airgap which create space harmonics. Besides, the magnetic field of the airgap created by the stator in slotted structures is stronger than in slotless machines, increasing the rotor losses. These are some of the reasons for which slotted stators are rarely used for VHS machines.

In the case of a sinusoidal stator supply, the fundamental component of the magnetic field of the stator rotates at the same speed as the rotor, and therefore only the harmonics induce eddy currents. For square wave stator supply ( $120^\circ$  or  $180^\circ$ ), since the magnetic field is stationary, the fundamental component plus all the harmonics are asynchronous with respect to the rotor leading to higher induced losses [41]. If present, the PWM generates high frequency stator current ripples leading to high frequency magnetic field time harmonics. However, these losses tend to be negligible for small machines [105]. Besides, PWM is not appropriate because the switching losses of transistors become too important and pulse amplitude modulation (PAM) is preferred instead [63].

Induced rotor losses can be calculated analytically under simplifying assumptions [96, 106–108]. Some are based on a first order vector potential formulation, i.e. the magnetic field produced by induced currents is negligible. However, if the skin depths of harmonics are relatively small compared to the dimensions of the rotor, a second order vector potential formulation (i.e. the diffusion equation) is requested. These models compute the total rotor eddy current losses as the sum of losses created by each harmonic. The losses can also be computed by FEM [107], with the drawback of being time consuming.

These losses can be reduced by choosing non-conductive sleeves, such as carbon fibre, and PM materials with higher resistivity, such as bonded alloys. The thickness of the airgap can also be increased, reducing the torque. However, as demonstrated experimentally in Chapter 6, rotor losses are negligible in miniaturised slotless machines and hence are not modelled.

## 4.7 Conclusion

In this chapter, the essentials for modelling electromagnetically PM slotless machines have been presented. The models comprise the computation of magnetic quantities and the depending losses in one pole pair diametrically magnetised cylindrical PM slotless machines. The most important magnetic quantity is the vector potential, from which the magnetic flux density can be deduced. Models for the computation of the back EMF voltage and the electromagnetic torque have been presented thanks to these quantities. They have been compared and validated to a 3D FEM model with an error of 4.3%. The back EMF constant is also experimentally validated in Chapter 6.

The electromagnetic losses related to the very high rotational speed of the rotor and the high electrical frequencies have been described and analysed. The electromagnetic losses have been divided into winding losses, iron losses and rotor losses. Models have been established by formulating an essential hypothesis: the magnetic field produced by the PM in slotless machines is much stronger than the one produced by stator currents or induced currents in the winding. As a result of this assumption, proximity effect losses in the winding and rotor losses can be ignored, as they represent a very small amount of the total losses in slotless machines.

An important contribution in this chapter comes from the development of an analytical model for the computation of induced eddy current losses in rectangular section windings. Indeed, very few models are available for these windings, and yet they are commonly used in slotless machines. The model is based on a first order vector potential formulation, because of the aforesaid hypothesis, but also because the dimensions of the wire have to be designed so that the skin depth in the conductor is equal or bigger. Consequently, the use of the diffusion equation is not necessary. A 2D FEM transient simulation has shown that proximity effect due to the induced currents is negligible given that an error of merely 1.8% with the analytical model has been highlighted. The model is also experimentally validated in Chapter 6.

A model for iron losses has been proposed and is based on empirical coefficients. An experimental technique able to separate the losses is presented in Chapter 6, which allows the definition of these coefficients.

Finally, this chapter gathers all necessary models for the design of permanent magnet slotless VHS machines. They are combined with the mechanical models of Chapter 3 and allow a multiphysics optimisation in Chapter 5.



# 5 Design and optimisation

## Contents

<b>5.1 Introduction</b>	<b>62</b>
<b>5.2 Models and design</b>	<b>63</b>
5.2.1 Mechanical models	63
5.2.2 Electromagnetic models	63
5.2.3 Power balance	67
<b>5.3 Optimisation framework</b>	<b>67</b>
5.3.1 Objective function	67
5.3.2 Design variables	68
5.3.3 Constraints and fixed parameters	68
5.3.4 Optimisation algorithm	70
<b>5.4 Comparison of conductors at several rotational speeds</b>	<b>70</b>
5.4.1 Fixed parameters specific to the case study	70
5.4.2 Results	70
<b>5.5 Comparison of solid and hollow magnet rotors</b>	<b>73</b>
5.5.1 Results	73
<b>5.6 Synthesis</b>	<b>75</b>
<b>5.7 Conclusion</b>	<b>76</b>

Publication of the author related to this chapter:

- Guillaume Burnand and Yves Perriard. Very-High-Speed Miniaturized Permanent Magnet Motors: Design and Optimization. In *2019 IEEE Energy Conversion Congress and Exposition (ECCE)*, pages 1–7. IEEE, October 2019.

### 5.1 Introduction

Electrical machines represent a large field of application for optimisation. Today's focus on the maximisation of the efficiency, but also on costs reduction, volume and/or weight limitation, legitimises optimisation. In addition, electrical machines are multiphysical by essence. They combine electromagnetic, mechanical and thermal properties. Associating several physical models results in antagonistic outcomes. For instance, reducing the radius of the permanent magnet increases its mechanical strength with respect to the rotational speed, but decreases the electromagnetic torque. The optimisation enables finding a suitable trade-off when many variables are involved.

There are at least two different approaches when performing multiphysics system optimisation: using finite element methods (FEM) [109, 110] or fully analytical models [35, 37]. The first ones can solve complex geometries and structures but require a long computational effort. Whereas the second ones are very fast, they do not always conform to reality because of simplifying assumptions. However, analytical models are preferred during pre-design in order to obtain fast estimations or to obtain inputs for FEM models. One can even consider a combination of the two approaches [111].

In electrical machines optimisation, both iterative methods, such as sequential quadratic programming (SQP) [112] and heuristic methods, such as genetic algorithm (GA) [37, 113, 114], Nelder-Mead simplex method [35], ant colony algorithm [115] or particle swarm optimisation [116] are used. One can also note the combination of FEM and metamodels [110]. Regarding VHS machines in particular, the optimisation of a 500 krpm-100 W PM synchronous motor has been investigated in [35]. Similarly, a 200 krpm-2 kW PM synchronous motor is optimised in [37]. Beside these 2 examples, not much has been found in the literature.

Although GA offers no guarantee of finding a true optimum, it does not need the initialisation of variables (initial guess) and it presents fewer risks of finding a local optimum, as its search space is broader than iterative methods [114]. These are the main reasons why GA is widely used in electrical machines optimisation [113] and thus, in the following. The present chapter does not focus on the mathematical and algorithmic aspects of optimisation. Instead, it presents a methodology to handle analytical models in order to design optimal VHS machines under given constraints and limitations.

Section 5.2 presents the different analytical models used for the optimisation. All have been experimentally validated in Chapter 6. They allow the computation of the back EMF voltage, the torque, the electrical and mechanical losses and the mechanical stresses in the rotor. The optimisation framework is established in Section 5.3, where the variables, the constraints and the optimisation algorithm are detailed. Later on, 7 optimisation scenarios involving motors are analysed. This original contribution of the chapter proposes the comparison of Litz-wire and rectangular wire windings in Section 5.4 and solid and hollow magnet rotors in Section 5.5. It finds the best suitable option for VHS machines. Finally, Section 5.6 synthesises the features to take into account when designing miniaturised VHS machines.

## 5.2 Models and design

The mechanical and electromagnetic analytical models presented respectively in Chapter 3 and Chapter 4 are implemented in the optimisation process.

### 5.2.1 Mechanical models

#### Rotor mechanical strength

The model used for the computation of the mechanical strength of the rotor is the one presented in Section 3.2. The materials of the rotor are given in Table 3.2.

#### Windage losses

Equation (3.25) with Mack's friction coefficient (3.26) is used for the computation of air friction losses. For manufacturing reasons, the axial length of the airgap  $L_\delta$  is longer than the one of the magnet  $L_{PM}$ . Therefore, the axial length of the airgap, in (3.25), is assumed to be

$$L_\delta = L_{PM} + \Delta L. \quad (5.1)$$

#### Ball bearing losses

The empirical model (3.32) is used for the computation of losses due to ball bearings. The values of the coefficients of regression are found in Table 6.2. In the following chapter, ball bearing losses are assumed to be independent from all other variables (they are speed-dependant only).

### 5.2.2 Electromagnetic models

The winding chosen for the optimisation is a 3-phase delta-connected winding. One of the coils is sketched in Figure 5.1. Delta-connection windings for VHS machines allow to reduce the back EMF voltage compared to star-connection windings. Although the chosen 3-coil winding has a lower filling factor compared to a 6-coil winding (see Chapter 7), it is easier to manufacture for miniaturised machines.

Currents are assumed to vary sinusoidally with time. The back EMF voltage is calculated from (4.10) and (4.11) and the electromagnetic torque from (4.12).

As indicated in Section 4.4, winding losses are assumed to be Joule losses and losses due to eddy currents induced by the field of the PM only (skin and proximity effects are not considered).

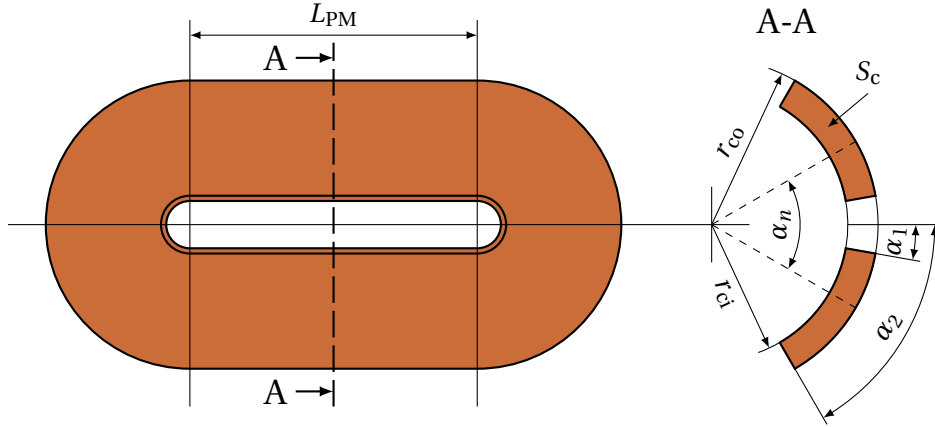


Figure 5.1 – Sketch of a coil.

### Back EMF voltage and electromagnetic torque for rectangular wires

Assuming that the straight parts of the winding have the same axial length as the permanent magnet and that the mechanical angle of the rotor  $\theta$  is chosen to give the maximal flux in the coil, the RMS back EMF voltage for this delta-connected winding is

$$U_{\text{EMF}} = \sqrt{2}\Omega \sum_{n=1}^{N_t} A_{\delta z}(\bar{r}_c, \varphi_n, \theta) L_{\text{PM}}, \quad (5.2)$$

where the  $\varphi_n$  are the angular coordinates of the  $N_t$  turns,  $L_{\text{PM}}$  is the axial length of the PM,  $A_{\delta z}$  is the vector potential in the airgap given by (4.3) and  $\bar{r}_c$  is the mean radius of the coil given by

$$\bar{r}_c = \frac{r_{\text{ci}} + r_{\text{co}}}{2}. \quad (5.3)$$

Using the mean radius is an approximation. Nevertheless, it proves to be sufficiently accurate as demonstrated experimentally in Section 6.3.4. According to (4.12), the interaction of the radial magnetic flux density in the airgap  $B_{\delta r}$  given by (4.7) and a current density  $J$  in one coil produces a torque equal to

$$T'_{\text{em}}(\theta) = 2\bar{r}_c h_w w_w J \sum_{n=1}^{N_t} B_{\delta r}(\bar{r}_c, \varphi_n, \theta) L_{\text{PM}}, \quad (5.4)$$

where  $w_w$  and  $h_w$  are respectively the width and the height of a wire given by (5.10) and (5.11).

Equation (5.4) can be maximised by using the peak current density  $\hat{J} = \sqrt{2}J$  and the mechanical angle of the rotor  $\theta$  so that no flux is passing through the coil, giving  $\hat{T}'_{\text{em}}$ . Finally, with 3 coils, the total electromagnetic torque is

$$T_{\text{em}} = \frac{3}{2} \hat{T}'_{\text{em}}. \quad (5.5)$$



### Back EMF voltage and electromagnetic torque for round wires

Considering a coil of  $N_t$  turns and the mechanical angle of the rotor  $\theta$  giving the maximal flux in the coil, the RMS back EMF voltage for this delta-connected winding is

$$U_{\text{EMF}} = \frac{\sqrt{2}N_t}{2S_c} c_\delta \Omega L_{\text{PM}} \left( \frac{r_{\text{co}}^3 - r_{\text{ci}}^3}{3} + r_{\text{yi}}^2 (r_{\text{co}} - r_{\text{ci}}) \right) \cdot \left( (\cos(\alpha_1 - \theta) - \cos(\alpha_2 - \theta)) + (\cos(-\alpha_1 - \theta) - \cos(-\alpha_2 - \theta)) \right), \quad (5.6)$$

where  $c_\delta$  is the constant defined by (4.4),  $\alpha_1$  and  $\alpha_2$  are the opening angles of the coil and  $S_c$  is half the section of the coil (as indicated in Figure 5.1) given by

$$S_c = \frac{1}{2} (r_{\text{co}}^2 - r_{\text{ci}}^2) (\alpha_2 - \alpha_1). \quad (5.7)$$

With a coil filling factor  $k_f$ , the interaction of the radial magnetic flux density in the airgap and a current density  $J$  in one coil produces a torque equal to [37]

$$T'_{\text{em}}(\theta) = k_f c_\delta J L_{\text{PM}} \left( \frac{r_{\text{co}}^3 - r_{\text{ci}}^3}{3} + r_{\text{yi}}^2 (r_{\text{co}} - r_{\text{ci}}) \right) \cdot \left( (\sin(\alpha_2 - \theta) - \sin(\alpha_1 - \theta)) + (\sin(-\alpha_2 - \theta) - \sin(-\alpha_1 - \theta)) \right), \quad (5.8)$$

As with the rectangular wires case, the total torque of the motor is obtained with (5.5).

### Winding losses for rectangular wires

With the winding in Figure 5.1, Joule losses are given by

$$P_{\text{Joule}} = 3\rho h_w w_w J^2 \left( 2N_t L_{\text{PM}} + \pi \bar{r}_c \sum_{n=1}^{N_t} \alpha_n \right), \quad (5.9)$$

where  $\rho$  is the resistivity of the coil,  $h_w$  and  $w_w$  are respectively the height and the width of a wire,  $J$  is the current density,  $N_t$  is the number of turns for one coil,  $L_{\text{PM}}$  is the axial length of the PM and the  $\alpha_n$  are the end-winding opening angles of each turns as shown in Figure 5.1. The width of a wire is assumed to be

$$w_w = \bar{r}_c \frac{\alpha_2 - \alpha_1}{N_t} - 2e_w, \quad (5.10)$$

and its height is

$$h_w = r_{\text{co}} - r_{\text{ci}} - 2e_w, \quad (5.11)$$

where  $e_w$  is the thickness of the insulation around the wire.

The losses due to eddy currents induced by the rotation of the PM are computed as detailed in Section 4.4.3.

### Winding losses for round wires

The section of a wire, considering the filling factor  $k_f$ , is

$$S_w = k_f \frac{S_c}{N_t}, \quad (5.12)$$

with  $S_c$  given by (5.7). Thereby, one obtains the Joule losses as

$$P_{\text{Joule}} = 3N_t \rho S_w J^2 (2L_{\text{PM}} + \pi \bar{r}_c (\alpha_1 + \alpha_2)). \quad (5.13)$$

The induced eddy currents losses due to the rotation of the PM are obtained as detailed in Section 4.4.2 thanks to (4.22) and using a diameter of the wire equal to

$$d_w = 2 \sqrt{\frac{S_w}{\pi}}. \quad (5.14)$$

### The case of Litz-wire

Litz-wire is made with  $N_{\text{strand}}$  tiny round section strands electrically insulated from one another (enamelled) and twisted to avoid circulating currents between the strands, as they may have different back EMF voltage [48]. The filling factor of Litz-wire slightly decreases as the diameter of strands gets smaller [63]. Again, a trade-off has to be found between Joule losses on the one hand, and eddy current losses due to the rotation of the PM on the other. In [63], Zwyssig has found the diameter of strands  $d_{\text{strand}} \in [30, 50] \mu\text{m}$  to be the range minimising both losses for similar dimensions and frequencies.

Knowing the diameter, the number of strands can be determined by

$$N_{\text{strand}} = \frac{4S_w}{\pi d_{\text{strand}}^2}. \quad (5.15)$$

Induced losses due to the rotation of the PM are further calculated with (4.22) using the diameter of strands  $d_{\text{strand}}$ . The back EMF voltage along with electromagnetic torque and Joule losses are calculated respectively with (5.6), (5.8) and (5.13).

### Iron losses

Iron losses are obtained with (4.33) and the material used for the stator is Metglas® 2605SA1 [117]. The reasons for this choice have been detailed in Section 2.4. This material is an amorphous iron-based alloy which features very low losses at high frequency. The values of the coefficients in (4.33) for this material can be found in Table 6.2.

### 5.2.3 Power balance

#### Sum of losses

In order to get the mechanical power (see Section 2.3.2) as a constraint during the optimisation, a power balance has to be done. The sum of all the losses is assumed to be

$$\Sigma P = P_{\text{windage}} + P_{\text{bearings}} + P_{\text{ironPM}} + P_{\text{windingPM}} + P_{\text{Joule}}. \quad (5.16)$$

#### Mechanical power

The mechanical power can then be calculated, knowing the electromagnetic torque  $T_{\text{em}}$  and the mechanical speed of the rotor  $\Omega$ , by

$$P_{\text{mec}} = T_{\text{em}}\Omega - (P_{\text{windage}} + P_{\text{bearings}} + P_{\text{ironPM}} + P_{\text{windingPM}}). \quad (5.17)$$

Joule losses are not subtracted from the electromagnetic power because they already have been considered in the power balance as depicted in Figure 2.4.

## 5.3 Optimisation framework

An optimisation process is almost unavoidable in electrical machines design, especially for VHS machines. For example, to reduce windage losses, the outer radius of the enclosure should be as small as possible. However, this also diminishes the electromagnetic torque because of a smaller magnet. This is a simple illustration of antagonistic objectives. Besides, the number of variables can easily reach a dozen or more. A global and multiphysics optimisation using robust and reliable models is then necessary.

As optimisation is based on mathematical laws, constraints have to be applied to the variables in order to give a physical sense to the optimisation. Applying too few constraints leads to unrealistic results whereas too many leads to infeasible solutions. A trade-off must therefore be found to ensure evenhanded solutions but also to guarantee the convergence of the algorithm.

### 5.3.1 Objective function

The minimisation of losses in VHS machines is one of the key aspects. Hence, the objective function to minimise is the sum of losses  $\Sigma P$  given by (5.16). Thermal modelling is not considered here. However, the minimisation of losses is consistent with the limitation of heating.

### 5.3.2 Design variables

The number of turns per coil  $N_t$  is chosen as a variable, as it is directly related to the back EMF voltage. Thus, the optimisation algorithm must be able to handle integer numbers. This is one of the reasons why GA is selected. Other variables are the remanence of the permanent magnet  $B_r$ , the RMS phase current density  $J$  and all the dimensions of the motor (see Table 5.3). This leads to a total of 12 variables.

Intuitively, the rotor of VHS machines should be designed as small as possible, given that windage losses scale with the outer radius of the enclosure to the power 4 (see (3.25)). In order to compensate this reduction, the remanence of the PM should be set at its maximal value to maintain the magnetic flux. However, in the case of hollow magnet rotors (see Section 3.2), significant mechanical stresses arise at the inner diameter of the PM, limiting the possibility of downsizing for a fixed diameter of the shaft.

Although VHS solid magnet rotors have been prototyped [37, 118], they turn out to be much more challenging from a manufacturing point of view. Therefore, the choice of hollow magnet rotors makes sense. From a manufacturing point of view, the diameter of the shaft is imposed by the inner diameter of ball bearings. Similarly, the outer diameter of ball bearings limits the inner diameter of the winding to enable the assembly of the motor.

In the case of hollow magnet rotors, the remanence of the permanent magnet should not be fixed before the optimisation as is usually the case. Indeed, in many works found in the literature review,  $B_r$  is mostly fixed before the optimisation. However, in this case, it should not be fixed beforehand because of its great impact on electromagnetic losses. The magnetic flux density in slotless machines is overwhelmingly due to the PM itself. Thereby, there is a compromise to find between the electromagnetic torque (high  $B_r$ ) on the one hand, and the losses (low  $B_r$ ) on the other. The same applies to the current density  $J$ , as a high current density is going to produce more electromagnetic torque but also more Joule losses.

The dimensions of rectangular wires given by (5.10) and (5.11) are not design variables. They are consequently deduced considering the dimensions of the coil, the number of turns and the thickness of the insulation. The opening angles of a coil, namely  $\alpha_1$  and  $\alpha_2$  (see Figure 5.1), are respectively set at  $10^\circ$  and  $60^\circ$ . The reason is that when set as design variables, the optimisation always tries to get the biggest section possible whether it is for rectangular wire or Litz-wire [119].

### 5.3.3 Constraints and fixed parameters

There are linear constraints on the minimal thickness of the enclosure and the airgap. These minimal thicknesses have been set at 0.2 mm, because lower thickness would be difficult to manufacture. The maximal current density, the maximal PM axial length and the outer diameter of the motor are constrained by upper boundaries. The minimal outer radius of the shaft has been set at 1 mm so that it corresponds to standard ball bearings.

Nonlinear constraints are set on the mechanical power  $P_{\text{mec}}$  given by (5.17), the mechanical strength of the rotor given by conditions (3.23) throughout the speed and temperature range, the maximal back EMF voltage and the maximal peak magnetic flux density in the stator yoke. The maximal peak magnetic flux density has to be lower than the magnetic saturation  $B_{\text{sat}}$  of the stator material. The maximal back EMF voltage has been set below 50 V to stay in the very low voltage range. However, this value depends on the maximal voltage of the power supply and can be changed accordingly.

The temperature of the winding has been assumed to be 100 °C and the one of the motor has been assumed to be 60 °C, because it is a common temperature for medical hand tools. The parameter  $\Delta L$  in (5.1) has been set to 4 mm. The remaining fixed parameters are listed in Table 5.1.

In order to avoid critical speeds lying near the speed range, the modal analysis is not considered in the optimisation. Critical speeds could be further computed with 3D FEM commercial software for complex geometries or could be added in the optimisation loop thanks to a 1D FEM [74].

Motor temperature	$T_{\text{mot}}$	60	[°C]
PM relative permeability	$\mu_r$	1.05	[-]
Wire resistivity	$\rho$	$20.0 \times 10^{-9}$	[Ωm]
Insulation for rectangular wires	$e_w$	10	[μm]
Stator stacking factor	$k_s$	0.82	[-]
Stator material saturation	$B_{\text{sat}}$	1.56	[T]
Max RMS back EMF voltage	$U_{\text{EMFmax}}$	50	[V]

Table 5.1 – Fixed parameters and constraints for the optimisation.

Maximal iterations	1200
Maximal stall generations	50
Population size	200
Nonlinear constraint algorithm	Augmented Lagrange
Crossover fraction <sup>1</sup>	0.8
Crossover function	Scattered
Elite count <sup>2</sup>	10

<sup>1</sup> The fraction of the population at the next generation, not including elite children, that the crossover function creates.

<sup>2</sup> Positive integer specifying how many individuals in the current generation are guaranteed to survive to the next generation.

Table 5.2 – Parameters for the genetic algorithm.

### 5.3.4 Optimisation algorithm

The optimisation is carried out using the genetic algorithm (GA) of the Matlab function *ga*. This enables the handling of an integer, which is the number of turns per coil  $N_t$ . Besides, for this number of variables, GA is more appropriate than iterative methods. Moreover, GA is preferred for the windage losses model (3.25), which is discontinuous (the friction coefficient has 2 equations depending on the Taylor number, see Section 3.4). It is also true for the winding losses model due to the field of the PM (4.30), which does not have an analytical solution and must be computed numerically. In these circumstances, the computation of a gradient would be complicated. Finally, GA does not require an initial estimation to start the optimisation and is less liable to find a local optimum. The parameters of the algorithm are given in Table 5.2.

## 5.4 Comparison of conductors at several rotational speeds

This section aims at comparing 2 types of conductors under different rotational speeds: Litz-wire and rectangular section wires. The purpose is to find out which one of the 2 is more adapted to miniaturised VHS machines.

### 5.4.1 Fixed parameters specific to the case study

The mechanical power is set at 40 W, which is common for medical hand tools. The different nominal speeds of the motor are {100, 200, 400} krpm, but, in order to have a safety margin, the rotor is designed to sustain a rotational speed of {125, 250, 500} krpm respectively. Hollow magnet rotors are chosen. They will be compared to solid magnet rotors in the next section. To keep reduced dimensions, the maximal axial length of the PM is set at 15 mm and the outer diameter of the motor at 12.7 mm. (The maximal outer radius of the stator yoke  $r_{yo}$  is set at 6 mm to allow space for the housing of the motor).

The maximal current density is set at 30 A/mm<sup>2</sup>. It has been demonstrated in [33] that lower current density values would result in a decrease of the efficiency. It seems counterintuitive, yet it increases the efficiency of the motor by allowing a better balance between Joule losses on the one hand and iron and winding losses due to the field of the PM on the other. For Litz-wire, the diameter of a strand  $d_{strand}$  has been selected to be 50  $\mu$ m (see Section 5.2.2 on Litz-wires) with a related filling factor  $k_f$  of 0.55 [120].

### 5.4.2 Results

A total of 5 optimisation scenarios have been carried out. The results are listed in Table 5.3. Firstly, it should be mentioned that the scenario with coils made of Litz-wire at 100 krpm-40 W was infeasible given the restricted dimensions and current density. Indeed, the lower the rotational speed, the higher the torque provided by the motor for a constant output power.

#### 5.4. Comparison of conductors at several rotational speeds

		Opt. 1	Opt. 2	Opt. 3	Opt. 4	Opt. 5	
Wire		Rect.	Litz	Rect.	Litz	Rect.	
<b>Constraints</b>							
Nominal rotational speed	$N$	100	200	200	400	400	[krpm]
<b>Design variables</b>							
Number of turns	$N_t$	24	27	39	61	39	[-]
PM remanence	$B_r$	1.31	1.30	1.24	1.33	1.07	[T]
PM axial length	$L_{PM}$	15.0	14.9	14.5	14.4	8.87	[mm]
Outer shaft radius	$r_{so}$	1.13	1.00	1.64	1.00	1.02	[mm]
Outer magnet radius	$r_{mo}$	2.55	2.43	2.79	1.84	2.37	[mm]
Magnet-enclosure interference at standstill	$e_0$	4.7	8.8	8.9	4.3	7.1	[ $\mu\text{m}$ ]
Outer enclosure radius	$r_{eo}$	2.86	2.63	2.99	2.04	2.57	[mm]
Inner coil radius	$r_{ci}$	3.23	2.83	3.53	2.23	3.43	[mm]
Outer coil radius	$r_{co}$	4.43	4.57	4.32	4.38	4.25	[mm]
Inner yoke radius	$r_{yi}$	4.53	4.67	4.42	4.48	4.35	[mm]
Outer yoke radius	$r_{yo}$	6.00	6.00	5.96	6.00	6.00	[mm]
RMS Phase current density	$J$	19.9	12.5	17.3	11.8	20.9	[A/mm <sup>2</sup> ]
<b>Derived quantities</b>							
Wire width	$w_w$	119	-	68	-	66	[ $\mu\text{m}$ ]
Wire height	$h_w$	1.20	-	0.78	-	0.82	[mm]
Number of strands	$N_{\text{strand}}$	-	58	-	28	-	[-]
RMS back EMF voltage	$U_{\text{EMF}}$	4.75	9.60	15.2	22.1	13.4	[V]
Stator peak flux density	$\hat{B}_y$	1.56	1.49	1.54	0.69	1.06	[T]
Mechanical airgap	$\delta$	0.37	0.20	0.54	0.20	0.86	[mm]
Sum of losses	$\Sigma P$	5.37	3.19	4.22	5.56	7.79	[W]
Ball bearing losses	$P_{\text{bearings}}$	0.10	0.52	0.52	2.69	2.69	[W]
Windage losses	$P_{\text{windage}}$	0.05	0.27	0.45	0.73	1.47	[W]
Iron losses due to the PM	$P_{\text{ironPM}}$	0.35	0.88	1.03	0.68	1.05	[W]
Winding losses due to the PM	$P_{\text{windingPM}}$	0.68	0.07	0.36	0.11	0.54	[W]
Joule losses	$P_{\text{Joule}}$	4.18	1.45	1.87	1.35	2.03	[W]
Motor efficiency	$\eta$	88.0	92.5	90.3	87.7	83.5	[%]

Table 5.3 – Optimisation results of motors with Litz-wire or rectangular wire at several rotational speeds.

This translates into an increase of the current given by  $I = k_f / S_c$ . However, Litz-wire has a low filling factor  $k_f$  and, because of the restricted dimensions of miniaturised machines (low coil section  $S_c$ ) and the limited current density, the requested torque was impossible to reach. This would also have been true using a mechanical power of 100 W at 100 krpm and 200 krpm with Litz-wire. When the motor has limited and narrow dimensions, the very high speed is necessary to reach a given output power. This illustrates the complexity of miniaturised machines design.

Opt. 2 and Opt. 3 compare designs at 200 krpm with Litz-wire and rectangular wire respectively. So do Opt. 4 and Opt. 5 but at a rotational speed of 400 krpm. As brought up in the previous paragraph, both comparisons show that designs with Litz-wire require a much larger section for the coils. This is depicted in Figure 5.2, where the normalised dimensions of the 4 designs are visible. For comparison, the filling factor of the coils made of rectangular wires is 0.75 versus 0.55 for the coils made of Litz-wire. However, the drawback of rectangular wires is that induced losses in the winding due to the rotation of the PM are 4 to 5 times higher in this case study.

Given that more space is required by the coils, the airgap is smaller in Litz-wire scenarios Opt. 2 and Opt. 4, as shown in Figure 5.2. The same applies for the outer radius of the enclosure  $r_{eo}$ , which allows to halve the windage losses. Indeed, as given in (3.25), these losses scale with the outer radius of the enclosure to the power 4.

A smaller rotor is also more prone to sustain mechanical stresses. Consequently, a smaller magnet produces less magnetic flux density in the machine, and thereby there is a lower peak magnetic flux density in the airgap and the stator yoke. It should be kept in mind that VHS machines do not require a high torque (their power comes mainly from their speed) Therefore, there is no need for a high magnetic flux density in the airgap. Also, induced losses (iron and winding) due to the rotation of the PM scale with the square of both rotational speed and

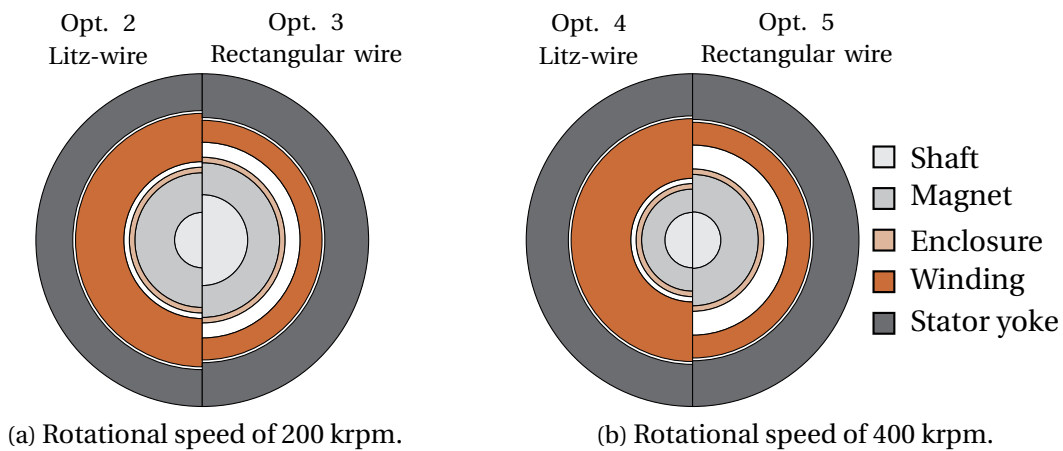


Figure 5.2 – Normalised dimensions of the motors.



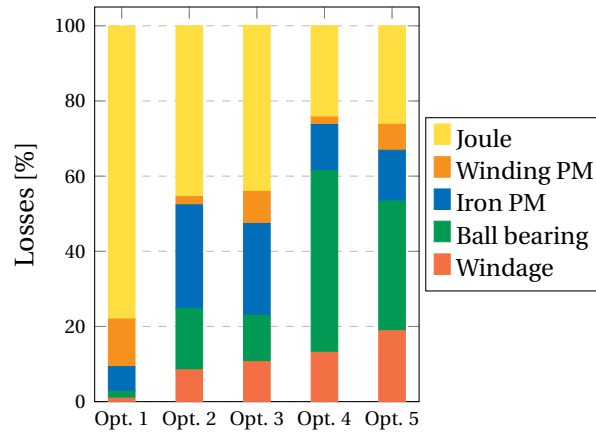


Figure 5.3 – Distribution of losses in the motors.

magnetic flux density. Given that the rotational speed is extremely high in VHS machines anyway, one can only act on the magnetic flux density.

The higher efficiency appears at 200 krpm for both types of wire (Opt. 2 and Opt. 3). The explanation lies in the distribution of losses with respect to the rotational frequency, as illustrated in Figure 5.3. At 100 krpm (Opt. 1), Joule losses (78%) outnumber the other losses and at 400 krpm (Opt. 4 and Opt. 5), the mechanical losses (sum of ball bearing and windage losses, 50 to 60%) outnumber the rest of losses. There is a peak efficiency between these 2 cases.

The efficiency of designs is better with Litz-wire, and the difference increases with the speed. At the same time, Opt. 5 shows that the axial length of the PM is almost 40% smaller using rectangular wires. The power density is then increased. The manufacturing of Litz-wire is complex and expensive. Strands may break during the forming of the coil (Litz-wire manufacturers even envisage this by giving a factor for broken wires [120]). Finally, the case study has demonstrated that some scenarios with Litz-wire are infeasible for the given constraints. All this may have an impact when considering the price of magnets and windings and the possibility of increasing the power density of the system.

## 5.5 Comparison of solid and hollow magnet rotors

In this section, the parameters of optimisation are the same as for the previous case study, except that for solid magnet rotors the inner radius of the shaft is set to zero.

### 5.5.1 Results

Two additional scenarios Opt. 6 and Opt. 7 with solid magnet rotors are proposed here. They have to be compared with Opt. 4 and Opt. 5 respectively. The results are visible in Table 5.4.

		Opt. 4	Opt. 6	Opt. 5	Opt. 7	
Wire		Litz	Litz	Rect.	Rect.	
<b>Constraints</b>						
Nominal rotational speed	$N$	400	400	400	400	[krpm]
<b>Design variables</b>						
Number of turns	$N_t$	61	69	39	35	[-]
PM remanence	$B_r$	1.33	1.35	1.07	1.40	[T]
PM axial length	$L_{PM}$	14.4	12.6	8.87	14.1	[mm]
Outer shaft radius	$r_{so}$	1.00	-	1.02	-	[mm]
Outer magnet radius	$r_{mo}$	1.84	1.61	2.37	1.53	[mm]
Magnet-enclosure interference at standstill	$e_0$	4.3	5.5	7.1	5.6	[ $\mu\text{m}$ ]
Outer enclosure radius	$r_{eo}$	2.04	1.81	2.57	1.73	[mm]
Inner coil radius	$r_{ci}$	2.23	2.01	3.43	3.05	[mm]
Outer coil radius	$r_{co}$	4.38	4.29	4.25	3.88	[mm]
Inner yoke radius	$r_{yi}$	4.48	4.39	4.35	3.98	[mm]
Outer yoke radius	$r_{yo}$	6.00	6.00	6.00	6.00	[mm]
RMS Phase current density	$J$	11.8	12.2	20.9	20.2	[A/mm <sup>2</sup> ]
<b>Derived quantities</b>						
Wire width	$w_w$	-	-	66	66	[ $\mu\text{m}$ ]
Wire height	$h_w$	-	-	0.82	0.83	[mm]
Number of strands	$N_{\text{strand}}$	28	25	-	-	[-]
RMS back EMF voltage	$U_{\text{EMF}}$	22.1	23.8	13.4	13.2	[V]
Stator peak flux density	$\hat{B}_y$	0.69	0.72	1.06	0.64	[T]
Mechanical airgap	$\delta$	0.20	0.20	0.86	1.32	[mm]
Sum of losses	$\Sigma P$	5.56	5.23	7.79	6.93	[W]
Ball bearing losses	$P_{\text{bearings}}$	2.69	2.69	2.69	2.69	[W]
Windage losses	$P_{\text{windage}}$	0.73	0.43	1.47	0.71	[W]
Iron losses due to the PM	$P_{\text{ironPM}}$	0.68	0.67	1.05	0.72	[W]
Winding losses due to the PM	$P_{\text{windingPM}}$	0.11	0.14	0.54	0.57	[W]
Joule losses	$P_{\text{Joule}}$	1.35	1.30	2.03	2.24	[W]
Motor efficiency	$\eta$	87.7	88.3	83.5	85.1	[%]

Table 5.4 – Optimisation results of motors with hollow or solid magnet rotors at several rotational speeds.

In the case of Litz-wire (Opt. 6), the diameter of the rotor has been reduced, increasing the available space for the winding and the stator yoke and decreasing the windage losses. For Opt. 7 with rectangular wires, the diameter of the rotor has been significantly decreased and the remanence of the PM has been set to its maximal value, as expected. The gain on losses seems light, however this represent a reduction of 11% on the losses for Opt. 7.

## 5.6 Synthesis

The following has been highlighted by the author in [33]. It gives an overview and summarises the design and the optimisation of miniaturised VHS machines. Increasing the outer diameter of a machine increases the efficiency (to some extent) for a given mechanical power. This has already been noticed in [35]. This fact can be explained by a better use of the available space in order to reduce the losses. Finally, the bigger the diameter of the machine, the better the thermal convection, because the surface of exchange is bigger. This demonstrates the difficulty of designing miniaturised machines.

The size of the rotor (radial dimensions) is imposed by the rotational speed. At 500 krpm and with sintered magnets, the limit of the mechanical strength of a rotor is reached for a radius of a little more than 3 mm. An increase of the radius would lead to a mechanical failure. Furthermore, it drastically increases windage losses.

Undeniably, windage losses represent an important part of the total losses for each optimisation. They are generally between 15-30%. This is why a reliable and validated model has to be selected for the design of VHS machines.

Another interesting remark is that Joule and winding losses due to the field of the PM are antagonistic. Indeed, increasing the section of the wire decreases the DC resistance, while enabling more induced eddy currents to flow.

VHS machines do not require a high magnetic flux density in the airgap as it drastically increases induced losses in the winding. Similarly, the value of the peak magnetic flux density in the stator yoke seems very low when compared to the saturation. This could be seen as a misuse of the iron capabilities. However, it should be seen as a way to decrease iron losses, which vary with the square of the peak magnetic flux density.

The smaller the wire, the higher the current density can be because the surface over volume ratio becomes greater, enhancing the cooling capabilities [121]. The same applies to PCB where the maximal current density is around  $35 \text{ A/mm}^2$  for a  $35 \mu\text{m}$  copper track thickness.

Finally, losses related to very high speed become an overwhelming part of the total losses and the reduced dimensions make it difficult to diminish them. As a consequence, the efficiency is generally lower than in low speed machines. Nonetheless, VHS machines offer a higher power density leading to a reduction of the size and the weight. All the aforementioned facts, plus the number of variables, make an optimisation process inevitable when designing VHS machines.

### 5.7 Conclusion

An optimisation method for very high speed electrical motors based on multiphysical analytical models has been presented. The set of the models presented is very complete and covers the mechanical design of the rotor, the computation of the losses and the computation of the back EMF voltage and electromagnetic torque for both Litz-wire and rectangular wire slotless windings. Even though analytical models may lack accuracy in some circumstances, they are preferred (at least for pre-design) when there is an important number of variables to optimise, because of their fast computing capabilities. They are also easily generalisable to machines of other size and speed. The models have been validated on a 400 krpm prototype in Chapter 6.

The framework of the optimisation sets down the objective function, the design variables and the different constraints and fixed parameters. A genetic algorithm has been chosen as it offers numerous advantages for multiphysical analytical nonlinear models with many variables. The objective function to be minimised was the sum of losses in the motors. Nevertheless, the proposed methodology is very flexible as it is based on analytical models. Indeed, a composite objective function with the weighted sum method [122] on every loss component could be easily implemented. Consequently, the designer could choose *a priori articulation of preferences* to give more weight on particular losses components. Although the optimisation has been focused on small scale VHS motors, it can be extended to any slotless machines.

The chapter has illustrated the difficulty of VHS electrical machines miniaturisation, because the losses do not decrease linearly with the size of the motor. Results strongly depend on the mechanical power provided and the nominal rotational speed. Furthermore, losses related to very high speed become a very important part of the total losses, and the reduced dimensions make it difficult to diminish these losses. As a consequence, the efficiency is generally lower than in low speed machines. Nonetheless, VHS machines offer a higher power density leading to a reduction of the size and the weight.

A thermal model could be implemented to the optimisation process for even more accuracy, and also to consider forced cooling of the motor. However, reducing the losses in the machine is consistent with the limitation of temperature. Similarly, a modal analysis could be added in the optimisation loop for the computation of critical speeds.

An original contribution of the chapter is the comparison between Litz-wire and rectangular wire windings. Indeed, VHS literature focuses predominantly on Litz-wire winding. Despite the fact that rectangular wire windings experience more induced losses due to the field of the PM, they can lead to a more compact design of the machine and therefore a reduction of the cost of materials. Furthermore, rectangular wires are easier and cheaper to manufacture and can reach higher torque densities than Litz-wire.

Finally, the comparison between hollow and solid magnet rotors shows that the latter offers better performances. Again, manufacturing constraints have to be considered before choosing between one of the two solutions.

# 6 Experimental validation

## Contents

<b>6.1 Introduction</b>	<b>78</b>
<b>6.2 Construction of the prototype</b>	<b>79</b>
<b>6.3 Measurements</b>	<b>81</b>
6.3.1 Resistance	81
6.3.2 Inductance	81
6.3.3 No-load losses	82
6.3.4 Back EMF and torque constant	82
6.3.5 Critical speeds	83
<b>6.4 Measurement technique to separate the losses</b>	<b>84</b>
6.4.1 Setup and tests	84
6.4.2 Results	88
6.4.3 Power balance	90
<b>6.5 Conclusion</b>	<b>91</b>

Publication of the author related to this chapter:

- Guillaume Burnand and Yves Perriard. Very-High-Speed Miniaturized Permanent Magnet Motors: Modeling and Experimental Validation. In *2019 IEEE Energy Conversion Congress and Exposition (ECCE)*, pages 1–7. IEEE, October 2019.

### 6.1 Introduction

Regarding research on experimental validation of mechanical and electrical models for VHS applications, one can cite Zwyssig *et al.* in [31] and Luomi *et al.* in [35], where measurements are carried out on a 500 krpm machine. They have used deceleration tests to determine the losses due to the rotation of the rotor. However, they were not successful in separating losses components, especially ball bearing losses. At the time of writing, it is the sole miniaturised VHS machine found in the literature.

Similarly in [123] and [124], a 100 krpm bearingless motor is modelled and validated experimentally. Nevertheless, it is not trivial to carry out deceleration tests on bearingless motors in order to determine the losses. In fact, it is quite possible that the bearing control system would create a breaking torque during the deceleration. In [125], 4 bearingless prototypes are investigated. Measurements are compared with the losses models. Only the sum of all losses could be verified, and not the different losses components separately. The same applies in [126] with a 150 krpm bearingless motor.

In [37], Pfister presents an experimental technique to measure ball bearing losses. With the help of a contactless coupling, 2 ball bearings mounted on a shaft are driven and a torquemeter records the torque reaction on the stator at several rotational speeds. In this chapter, another method is proposed to determine ball bearing losses. Again, Pfister presents an interesting dynamic torque measurement technique in [3]. It is based on an acceleration test that emulates a mechanical load. Unfortunately, this technique could not be applied to the prototype here, as the acceleration needed would have been tremendous due to the very small inertia of the rotor.

The chapter aims at experimentally validating the models presented in Chapter 3 and Chapter 4. Consequently, a miniaturised VHS prototype is manufactured and operated up to a rotational speed of 475 krpm. Section 6.2 presents the construction of the 400 krpm 12.7 mm (0.5 inch) diameter prototype. To the author's knowledge, it is one of the smallest and fastest electrical motors ever operated. The dimensions of the prototype are not optimised. Indeed, at the time when the prototype was designed, some models were not yet validated. An optimisation such as in Chapter 5 would have been uncertain. Instead, the prototype is used as a tool in order to validate the models.

Subsequently, several relevant quantities are measured on the prototype in Section 6.3, such as the resistances and inductances of the coils, no-load losses, the back EMF constant and critical speeds. Except for no-load losses, every measurement is compared to the theoretical models. Finally, an innovative experimental method to separate every losses component due to the rotation of the rotor (see Section 2.3) is proposed and tested on the prototype in Section 6.4.

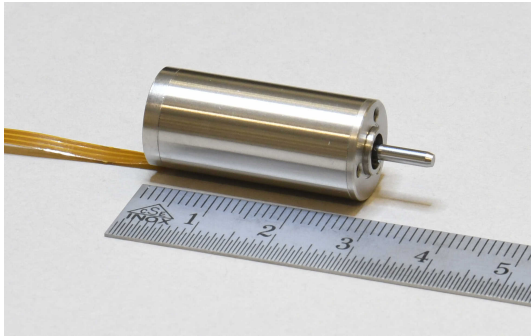
Unfortunately, it has not been possible to operate the prototype under load. Nonetheless, losses in PM slotless VHS machines are overwhelmingly speed dependant, not current dependant. The measurements are oriented on the motor alone and do not consider the motor as

part of a system. For instance, power electronic losses are not considered as they depend on the power converter and its control strategy.

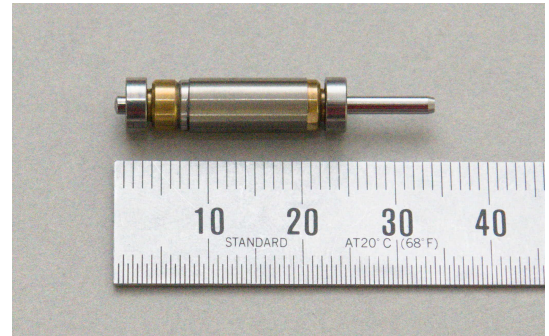
### 6.2 Construction of the prototype

The miniaturised prototype is 12.7 mm in diameter (0.5 inch) and 28 mm in length and is visible in Figure 6.1a. The rotor has been designed to withstand a rotational speed of 500 krpm thanks to the model in Section 3.2. The NdFeB permanent magnet is made in one-piece and its enclosure is in titanium grade 5. The mechanical properties of the materials are given in Table 3.2. Brass rings are used to radially centre the enclosure and are machined afterwards for the balancing. The rotor is supported by mini ball bearings as it can be seen in Figure 6.1b.

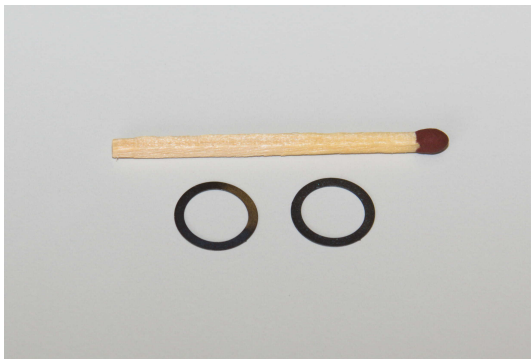
The stator is made of amorphous iron-based Metglas® 2605SA1 alloy, which features very low losses at high frequency [117]. The sheet are 25  $\mu\text{m}$  in thickness and can be seen in Figure 6.1c. The 3-phase 3-coil winding is made of rectangular wires, as depicted in Figure 6.1d. The coils are delta-connected. The cross-section of the prototype is similar to Figure 4.1. The inner dimensions and the parameters are given in Table 6.1.



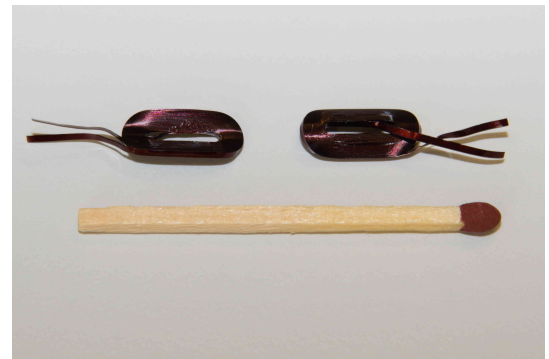
(a) Assembly of the prototype.



(b) The rotor.



(c) Stator sheets.



(d) Coils.

Figure 6.1 – Pictures of the VHS prototype employed for the experimental validation of the models.

Parameters			
Nominal power	$P_{mec}$	40	[W]
Nominal speed	$N$	400	[krpm]
PM remanence	$B_r$	1.13	[T]
PM permeability	$\mu_r$	1.05	[-]
Coil resistivity	$\rho$	$18 \times 10^{-9}$	[ $\Omega m$ ]
Number of turns per coil	$N_t$	29	[-]
Stator stacking factor	$k_s$	0.82	[-]
Stator material saturation	$B_{sat}$	1.56	[T]
Rotor inertia	$J$	$14.32 \times 10^{-9}$	[kg m <sup>2</sup> ]
Dimensions			
Inner magnet radius	$r_{mi}$	1.0	[mm]
Outer magnet radius	$r_{mo}$	2.75	[mm]
Outer enclosure radius	$r_{eo}$	2.95	[mm]
Inner yoke radius	$r_{yi}$	4.5	[mm]
Outer yoke radius	$r_{yo}$	5.9	[mm]
Inner wire distance	$y_{wi}$	3.3	[mm]
Outer wire distance	$y_{wo}$	4.2	[mm]
Wire width	$w_w$	70	[ $\mu m$ ]
Wire height	$h_w$	0.9	[mm]
PM axial length	$L_{PM}$	10	[mm]
Motor diameter	$d_{mot}$	12.7	[mm]

Table 6.1 – Parameters and dimensions of the VHS prototype.

The motor is driven with a commercially available sensorless PAM power converter. PAM is preferred to PWM for very high speed machines as the switching frequency is the same as the fundamental electrical frequency, but the DC bus voltage is modulated [63]. This produces fewer switching losses in the power switches and less current ripple in the machine.



## 6.3 Measurements

### 6.3.1 Resistance

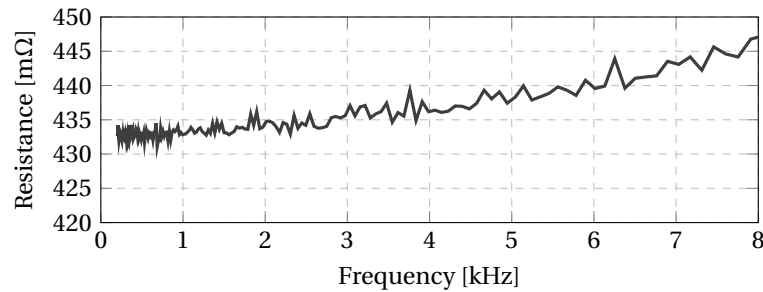
The DC resistance of the 3 coils at 20 °C has been measured at 245 mΩ. The theoretical value is 225 mΩ, giving an error -8.2%. This difference may originate from the forming process of the coil, where deformation occurs which can modify the section of the wire.

The coils are then delta-connected on a PCB, which is connected to a cable for the power supply. The measurement of the phase-to-phase resistance with an LCR meter is shown in Figure 6.2a. The resistance slightly increases with the frequency due to the skin effect (see Section 4.4). The value is later used in Section 6.4.3 for the computation of Joule losses.

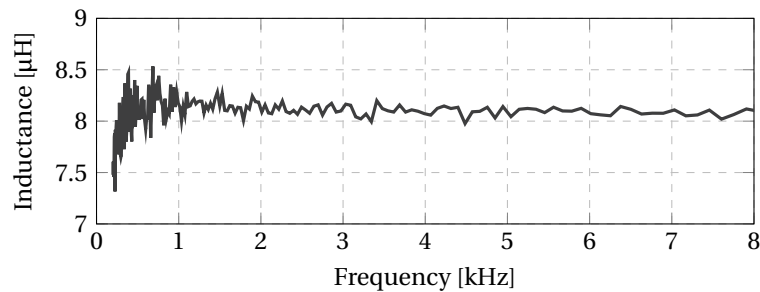
### 6.3.2 Inductance

The 3D FEM model used in Section 4.3.5 is adapted to compute the self-inductance of the individual coils. The value is 10.28 μH. Measurements give a value of 11.1 μH (error of 8%).

Similarly to the phase-to-phase resistance, the phase-to-phase inductance is measured as depicted in Figure 6.2b. The value is constant on the whole range.



(a) Phase-to-phase resistance.



(b) Phase-to-phase inductance.

Figure 6.2 – Measurements of the phase-to-phase inductance and resistance taking into account the power supply cable.

### 6.3.3 No-load losses

No-load electrical losses are measured with a Newtons4th PPA5530 3-phase high precision power analyser connected between the power converter and the motor. The losses are plotted in Figure 6.3 for a maximal speed up to 475 krpm. This is the fastest speed reached with the prototype. A 3rd order polynomial fitting is superposed to the measured points. The losses almost double from 400 to 500 krpm. This illustrates the tremendous increase of losses with respect to the rotational speed. The value of no-load losses at 400 krpm is a little more than 11 W. The optimisation in Section 5.4.2 has demonstrated that this value could be decreased to 7.79 W, which is a reduction of -29%.

### 6.3.4 Back EMF and torque constant

The motor is mounted on a coupling bench as pictured in Figure 6.10 and driven by another one. The back EMF voltage of the 3 phases has been measured up to 250 krpm. They are perfectly symmetrical and balanced. A screenshot of the voltage over time extracted from an oscilloscope is shown in Figure 6.4 at the maximal speed. The sinusoidal waveform can be observed. The RMS back EMF voltage  $U_{EMF}$  is defined as

$$U_{EMF} = k_e \Omega, \quad (6.1)$$

with  $\Omega$  the rotational speed in rad/s. The RMS value of the back EMF voltage is visible in Figure 6.5. As the 3 coils are delta-connected, the phase-to-phase voltage equals the phase voltage. The regression gives a measured value of  $k_{e\text{meas}} = 330.5 \mu\text{V}/\text{rad/s}$ . From (5.2) in Section 5.2.2, the theoretical back EMF constant can be derived. This gives  $k_e = 334.9 \mu\text{V}/\text{rad/s}$ , namely a difference of 1.3%.

The torque constant for one phase, as defined by (7.5) in Section 7.3.1, has therefore the same numerical value as the back EMF constant hereinabove.

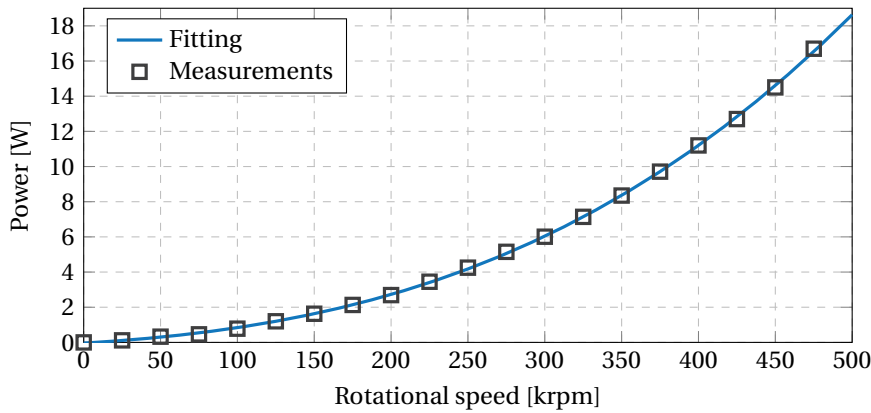


Figure 6.3 – No-load losses with respect to the rotational speed up to 475 krpm.

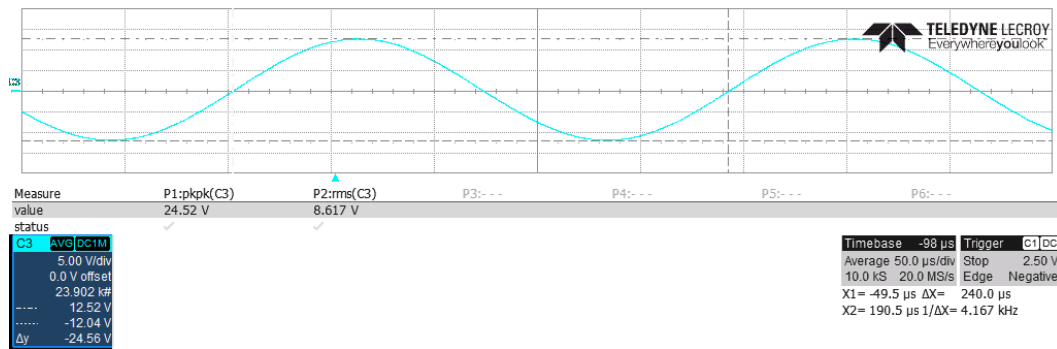


Figure 6.4 – Back EMF voltage over time at 250 krpm on the oscilloscope.

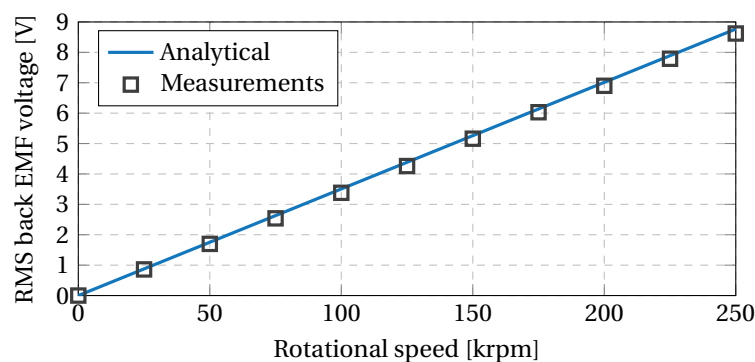


Figure 6.5 – RMS back EMF voltage with respect to the rotational speed.

### 6.3.5 Critical speeds

Critical speeds can be obtained by measuring the unbalance of the shaft [127] or by impulse force response tests [128]. Taking into account the size of the motor, the first method is adopted here. The unbalance at the extremity of the shaft has been measured with a Polytec CLV 1000 laser vibrometer for a rotational speed up to 400 krpm. The results can be visualised in Figure 6.6 where the maximal peak-to-peak displacement occurs at 280 krpm (4667 Hz). The rotor-bearing system is well damped as the peak of amplitude is not very pronounced [76]. This peak corresponds to the first and only critical speed throughout the speed range. As described in Section 3.3.4, it is a cylindrical whirl.

The theoretical value computed with 3D FEM is 276 krpm (4598 Hz), which is a discrepancy of 1.4%. This value has been obtained considering a radial stiffness of the ball bearings of 1.75 N/μm. Along with the axial stiffness, the radial stiffness increases with the axial preload [28]. Indeed, to stiffen the assembly and to avoid vibration and a premature wear, the rings are preloaded with an axial force. This preload is generally done by a spring. Thereby, the force versus displacement curve of the spring used in the prototype has been characterised. Then, knowing the compression of the spring, the axial force applied on the ball bearing can be deduced. Finally, the radial stiffness is assessed thanks to the data given by the manufacturer.

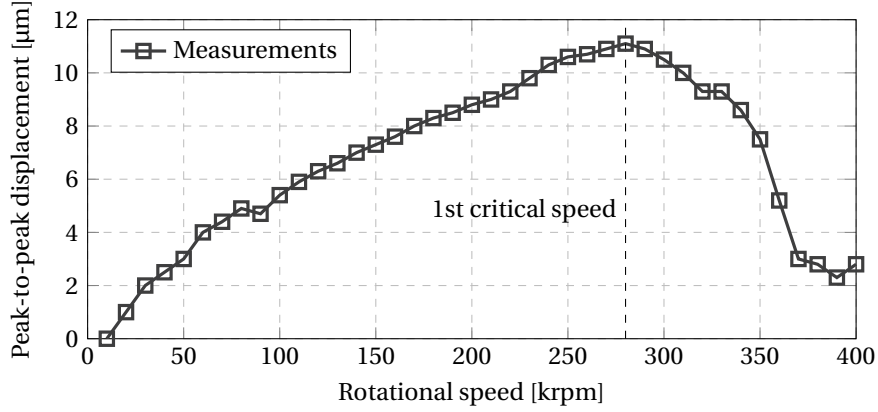


Figure 6.6 – Modulus of the unbalance of the shaft with respect to the rotational speed.

## 6.4 Measurement technique to separate the losses

### 6.4.1 Setup and tests

Deceleration tests, also named spin down tests, are broadly used to evaluate losses due to the rotation of rotors [24]. The 4 losses components due to the rotation of rotors in slotless PM motors with ball bearings are depicted in Figure 2.4. Newton's second law states that the rate change of velocity is proportional to the applied torque in a rotating system. When multiplied by the mechanical rotational speed, it becomes

$$-J_{\text{rot}} \frac{d\Omega}{dt} \Omega = P_{\text{windage}} + P_{\text{bearings}} + P_{\text{ironPM}} + P_{\text{windingPM}}, \quad (6.2)$$

where  $J_{\text{rot}}$  is the inertia of the rotor,  $P_{\text{windage}}$  are the windage losses,  $P_{\text{bearings}}$  the ball bearing losses and  $P_{\text{ironPM}}$  and  $P_{\text{windingPM}}$  are respectively the iron and winding losses due to the field of the PM. The minus sign in (6.2) refers to a braking torque.

In practice, the speed of the rotor is increased to be slightly higher than the nominal speed, then the electrical supply is shut down (the phases are in open-loop). The losses related to the current are consequently nil. The speed is measured with an optical tachometer. A diode emits light that reflects on the shaft back to a photodiode. A continuous dark zone on the shaft enables interruption the beam, producing a rectangular signal with the same frequency as the mechanical rotational speed. This signal is later postprocessed. First, zero crossings are identified to obtain the rotational speed over time. Then, the signal is filtered and a regression with a polynomial fitting is processed. This allows proper calculation of the time derivative in (6.2). Some rotational speed over time curves are plotted in Figure 6.7. Finally, the power is obtained knowing the inertia of the rotor.

Unfortunately, if the test is performed just as it is on the motor, only the sum of the 4 components is deduced. The following technique allows to separate the 4 losses components carrying out an equal number of tests successively. The tests are referred to as Test 1 to Test 4.

#### 6.4. Measurement technique to separate the losses

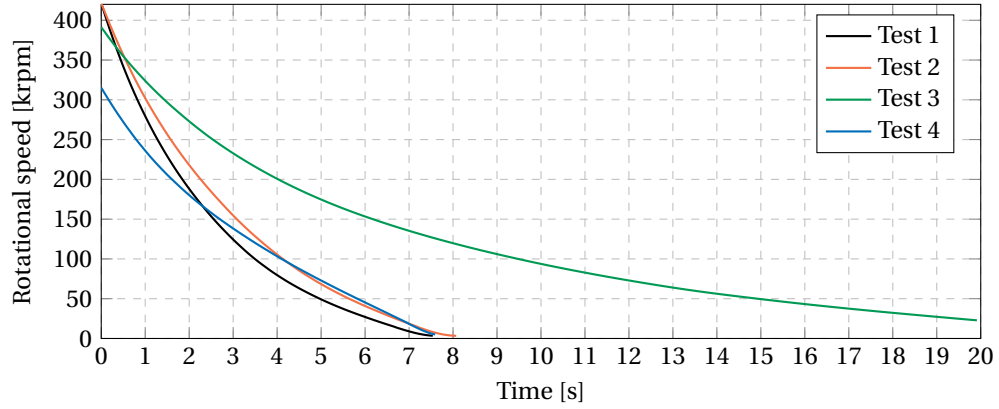


Figure 6.7 – Rotational speed (deceleration) over time for the 4 tests.

Test 1 is a spin down test achieved at ambient pressure that gives the sum of the 4 components as in (6.2). The deceleration over time can be seen in Figure 6.7. The initial configuration of the motor is composed of the stator S1 and the rotor R1.

Test 2 is then achieved with the same motor (stator S1 and rotor R1), but in a vacuum chamber where the pressure is lower than 1 mbar as pictured in Figure 6.8. This test gives

$$-J_{\text{rot}} \frac{d\Omega}{dt} \Omega = P_{\text{bearings}} + P_{\text{ironPM}} + P_{\text{windingPM}}. \quad (6.3)$$

The different evolutions of the speed over time of Test 1 and Test 2 can be clearly identified in Figure 6.7. Hence, windage losses are deduced by the subtraction from (6.3) to (6.2).

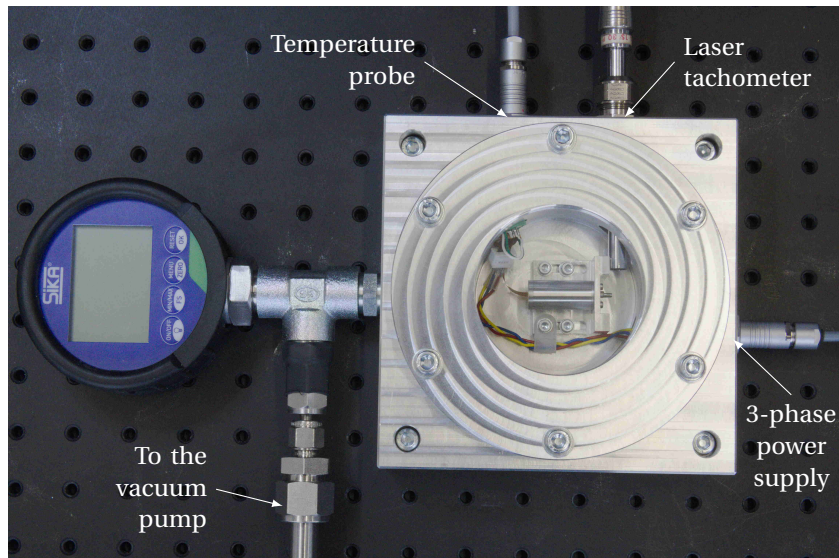


Figure 6.8 – Vacuum chamber ( $P < 1$  mbar).

## Chapter 6. Experimental validation

Test 3 enables the determination of ball bearing losses. For this test, the terms  $P_{\text{ironPM}}$  and  $P_{\text{windingPM}}$  in (6.3) should be removed. This can be done by replacing the original rotor R1 by a non-magnetized rotor R2 in the stator S1. This is illustrated in Figure 6.9. Of course, the new configuration has to be driven at the desired speed by means of another motor. Thus, both motors are mounted on a very accurate XYZ-stage as visible in Figure 6.10 to ensure an alignment as perfect as possible. Once the speed is reached, the powered motor is decoupled and the deceleration of the non-magnetized rotor can be measured. The test gives

$$-J_{\text{rot}} \frac{d\Omega}{dt} \Omega = P_{\text{windage}} + P_{\text{bearings}}. \quad (6.4)$$

Ball bearing losses are thereafter calculated by subtracting the windage losses previously obtained to (6.4).

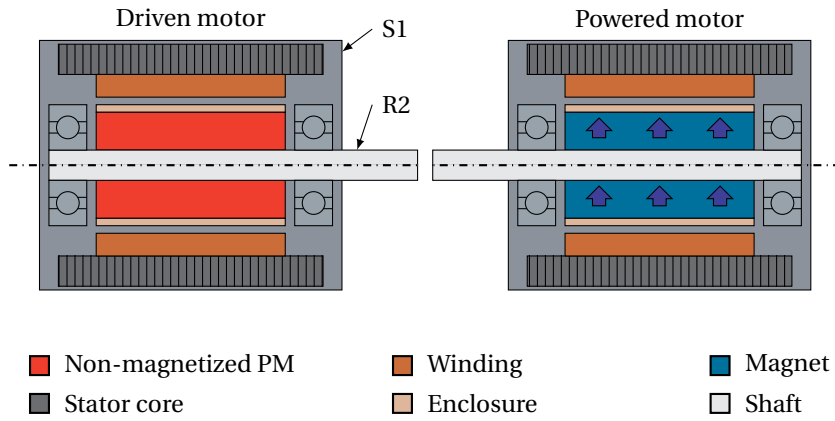


Figure 6.9 – Measurement of ball bearing losses (Test 3).

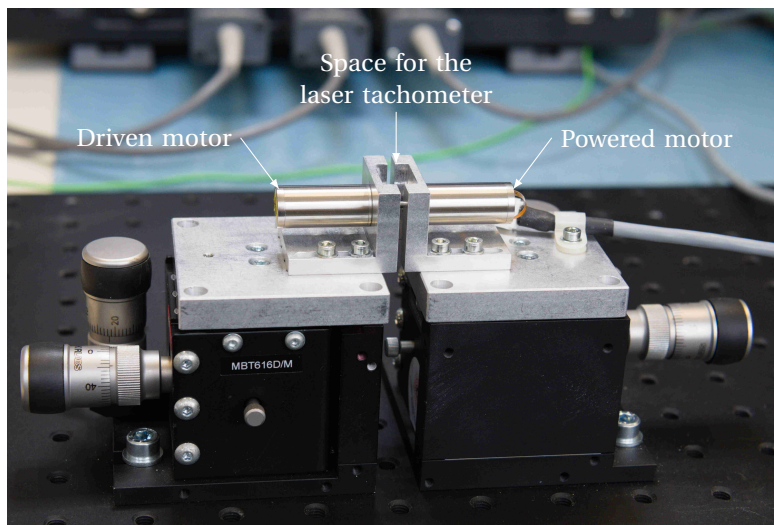


Figure 6.10 – Coupling bench.

#### 6.4. Measurement technique to separate the losses

Test 4, which is the final test, enables the measurement of iron losses due to the field of the PM. Another stator is necessary to succeed in this test. It is named S2 and its particularity is that the coils are replaced by non-conductive fictitious coils. By removing the coils, winding losses due to the field of the PM vanish, but the magnetic conditions remain unchanged. However, the mechanical airgap and the surface condition on the inner side of the fictitious coils both have to be strictly identical. The test is schemed in Figure 6.11. The rest of the test is identical to the previous ones and gives

$$-J_{\text{rot}} \frac{d\Omega}{dt} \Omega = P_{\text{windage}} + P_{\text{bearings}} + P_{\text{ironPM}}. \quad (6.5)$$

By subtracting the windage and the ball bearing losses to this test, the iron losses due to the field of the PM are determined. Finally, the winding losses due to the field of the PM are obtained by subtracting the 3 other losses from the sum of all losses given by Test 1.

The benefit of deceleration tests is to obtain the losses with respect to the rotational speed in one measurement, although successive measurements are favoured to get an average of the tests. Also, a mechanical measurement of the speed of the rotor is preferred as opposed to the measurement of the back EMF voltage frequency like in [121]. Obviously, a non-magnetised permanent magnet does not produce a back EMF voltage in the stator winding.

The advantage of the proposed method is to insulate the losses components due to the rotation of the rotor from one another. As a result, each model can be validated and/or obtained. The disadvantage of this method is that the inertia of the rotor has to be perfectly established. It can be calculated analytically for trivial geometries or computed with CAD software. As it depends on the density of materials, it is recommended to weigh the rotor and to compare with the theoretical mass. Another drawback is that 2 different stators and 2 different rotors are necessary. Other features have to be carefully considered. Since all the losses are temperature dependent, the temperature has to be similar between the setups and the measurements. The 2 stators and the 2 rotors have to be as near to identical as possible geometrically and

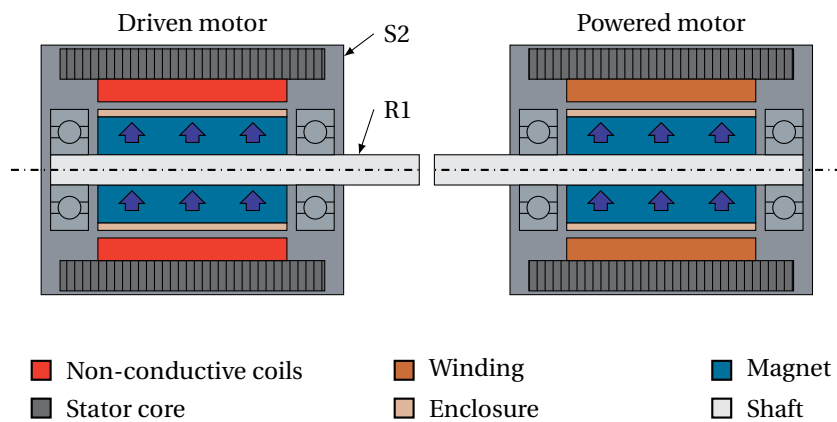


Figure 6.11 – Measurement of iron losses due to the field of the PM (Test 4).

mechanically. In particular, the preload of the ball bearing and the mechanical airgap have to be the same. A good practice is to perform similar measurements on different setups and compare the results obtained if possible.

### 6.4.2 Results

The following results have been obtained from an average of 7 to 10 measurements with the same temperature conditions for each of the 4 tests. The 4 losses components with respect to the rotational speed are reported in Figure 6.12. Iron losses due to the field of the PM have been measured only up to 300 krpm as visible in Figure 6.12c. The reason for this is that the coupling was not able to withstand the requested torque at higher speed. Hence, winding losses due to the field of the PM have also been determined up to 300 krpm only, as shown in Figure 6.12d.

Figure 6.12a compares the measurement of windage losses (the dashed line) with the model given by Mack in Section 3.4. The maximal error is -24% and occurs at 120 krpm. Above that speed, the error ranges from -16.7% to 8.6%, which is more than satisfactory for an empirical model. According to the Taylor number  $Ta$ , the flow in the airgap is laminar up to 50 krpm ( $Ta = 41.2$ ) and so called Taylor vortices start to appear beyond that threshold. The speed where the flow is fully turbulent ( $Ta > 400$ ) is beyond 400 krpm.

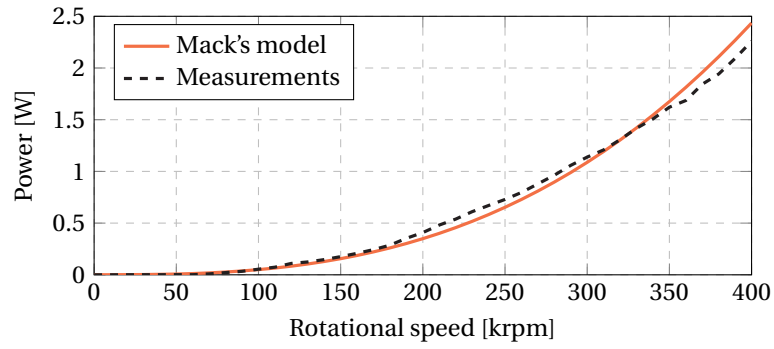
Figure 6.12b gives the ball bearing losses. The discrepancy ranges from -6.6% to 12.4 % above 120 krpm between the measurements and the model given by (3.32). The coefficients of the model are obtained with a nonlinear fitting and are given in Table 6.2.

As for the error on iron losses due to the field of the PM in Figure 6.12c, it ranges from -6.6% to 11.3% above 120 krpm between the model given by (4.33) and the measurements. The coefficients are also given in Table 6.2. A linear behaviour due to hysteresis losses can be observed up to 170 krpm. At higher speeds, eddy current losses become more important. Two Steinmetz's equations found in the literature review [129, 130] for the computation of iron losses in Metglas®2605SA1 are highlighted in Figure 6.12c. The first one clearly undervalues the losses, whereas the second one exaggerates them. This demonstrates that empirical coefficients found in the literature review have to be used with care [131].

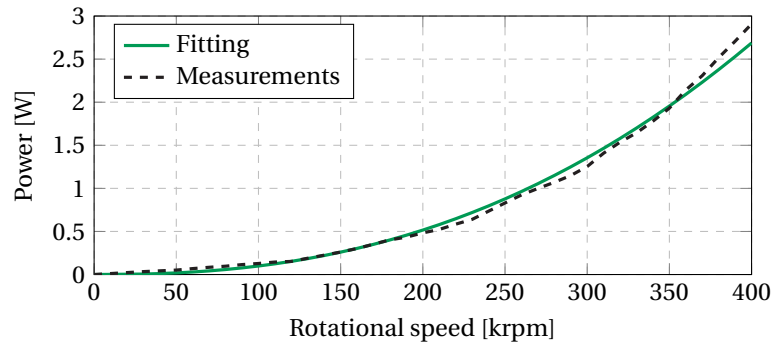
Winding losses due to the field of the PM in Figure 6.12d are compared with the model described in Section 4.4.3. The model underestimates the losses up to -28.8% in a narrow range, close to 160 krpm, probably due to a slight mechanical difference between the setups. Elsewhere, it remains excellent. This allows to experimentally validate the developed model.

In order to ensure the extrapolation of models for the iron and winding losses due to the field of the PM from 300 to 400 krpm (Figures 6.12c and 6.12d), Figure 6.13 contrasts the sum of all the losses given by the individual models and the measurements of Test 1. The matching is excellent, and furthermore, the share of every component can be observed. It turns out that the 4 components are more or less equal.

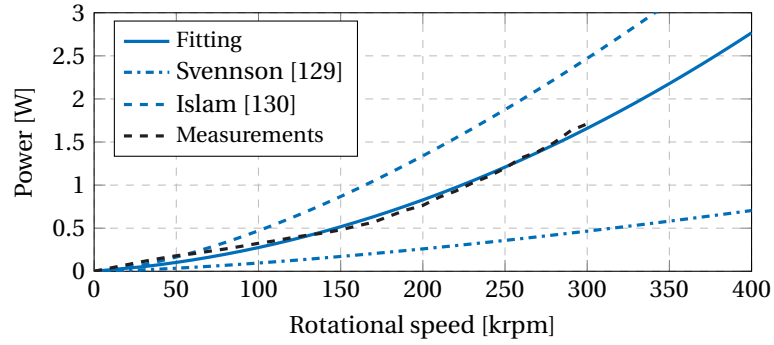




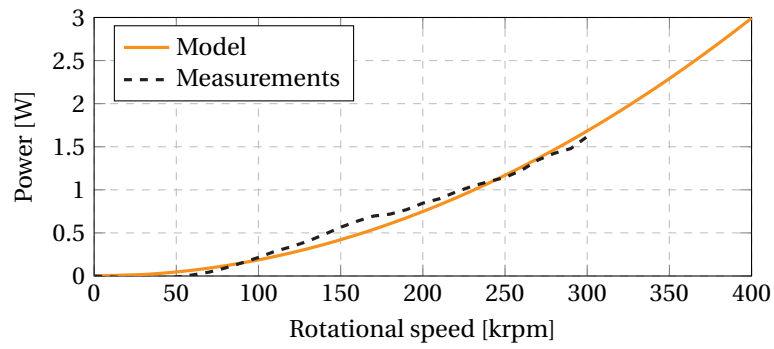
(a) Windage losses.



(b) Ball bearing losses.



(c) Iron losses due to the field of the PM.



(d) Winding losses due to the field of the PM.

Figure 6.12 – Measurements of losses components due to the rotation of the rotor.

Ball bearing losses	
$c_{\text{bearings1}}$	$26.677 \times 10^{-12}$
$c_{\text{bearings2}}$	2.380
Iron losses due to the field of the PM	
$c_{\text{iron1}}$	11.415
$c_{\text{iron2}}$	$1.110 \times 10^{-3}$

Table 6.2 – Constants for the model of ball bearing and iron losses.

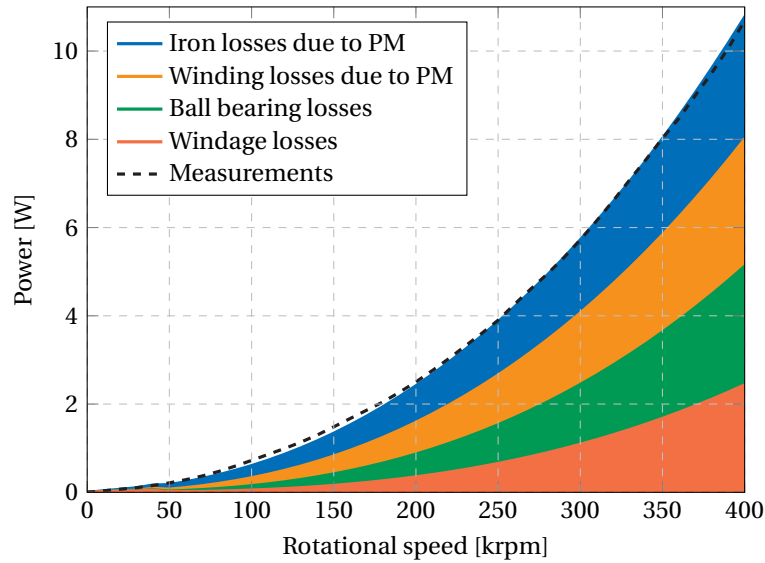


Figure 6.13 – Sum of all the individual losses models compared to the measurements (Test 1) of all losses due to the rotation of the rotor.

### 6.4.3 Power balance

A power balance can be established as a result of the measurement of no-load electrical losses in Figure 6.3. As seen in the power diagram in Figure 2.4, subtracting the sum of all losses due to the rotation of the rotor to no-load electrical losses gives the sum of losses due to the stator currents. Hence, the sum of Joule losses (including skin effect losses) and proximity effect losses in the coils, stator iron losses due to the currents and induced eddy current losses in the rotor can be seen.

Knowing the phase-to-phase resistance and the RMS line current, Joule losses (including skin effect losses), given by (4.16), can be separated from the previous sum. Figure 6.14 illustrates Joule losses in yellow and the remaining losses due to the stator currents in brown. The amount of the last losses at 400 krpm is merely about 4% of the total no-load losses. This confirms the hypothesis made in the previous chapters that the magnetic flux density in slotless PM motors is overwhelmingly due to permanent magnets.

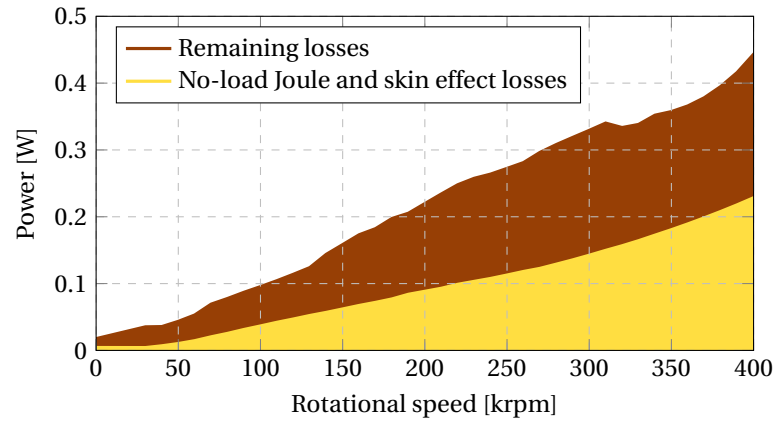


Figure 6.14 – Losses due to the stator currents.

## 6.5 Conclusion

A miniaturised VHS prototype of 12.7 mm in diameter (0.5 inch) and 28 mm in length has been manufactured and operated at a rotational speed up to 475 krpm. To the author's knowledge, it is one of the smallest and fastest electrical motor ever operated. The prototype has been used as a tool for validating the models of resistance and inductance of the coils, back EMF constant, critical speeds and losses. The models match the measurements very well.

One of the most important contribution of the chapter comes from the experimental method that enables the separation of the losses components due to the rotation of the rotor in very high speed permanent magnet machines with ball bearings. These are the windage losses, the ball bearing losses and the winding and iron losses due to the rotation of the permanent magnet. The method has been tested and validated on a miniaturised prototype up to 400 krpm. Hence, the 4 losses models have been validated and/or obtained. Thereby, knowing the repartition of these losses allows to act on and reduce the most important of them.

In particular, the analytical model for the computation of induced eddy current losses in rectangular section conductors due to a rotating magnetic field presented in Section 4.4.3 has been validated. Moreover, the empirical windage losses model developed by Mack turns out to be reliable for miniaturised VHS machines. The comparison of iron losses measurement in Metglas®2605SA1 with Steinmetz's equations found in the literature review have demonstrated the evidence that losses coefficients should be used carefully, as they can give considerably different estimations.

Finally, the power balance of the prototype has highlighted the fact that proximity effect losses in the coils, stator iron losses due to the currents, and induced eddy current losses in the rotor are negligible in miniaturised slotless PM machines, as they represent only a few percent of the total losses.



# 7 Towards a new winding topology

## Contents

---

<b>7.1 Introduction . . . . .</b>	<b>95</b>
<b>7.2 Winding topology . . . . .</b>	<b>96</b>
7.2.1 Preliminary considerations . . . . .	96
7.2.2 Geometry and parameters . . . . .	97
<b>7.3 Modelling . . . . .</b>	<b>98</b>
7.3.1 Torque constant . . . . .	98
7.3.2 Back EMF constant . . . . .	99
7.3.3 Resistance . . . . .	100
7.3.4 Motor constant . . . . .	101
7.3.5 Winding factor . . . . .	102
<b>7.4 Optimisation . . . . .</b>	<b>103</b>
7.4.1 Objective function . . . . .	103
7.4.2 Optimisation framework . . . . .	103
7.4.3 Results . . . . .	103
7.4.4 3D FEM validation . . . . .	106
<b>7.5 Prototype and measurements . . . . .</b>	<b>107</b>
7.5.1 Realisation of the prototype . . . . .	107
7.5.2 Experimental validation . . . . .	108
<b>7.6 Implementation in rotating and linear machines . . . . .</b>	<b>110</b>
<b>7.7 Conclusion . . . . .</b>	<b>111</b>

---

Patent of the author related to this chapter:

- Guillaume Burnand, Douglas Martins Araujo, and Yves Perriard, Electrical machines winding. CH20180001134, 2018.

Publications of the author related to this chapter:

- Guillaume Burnand, Douglas Martins Araujo, and Yves Perriard. Optimization of shape and topology for slotless windings in BLDC machines. In *21st International Conference on Electrical Machines and Systems (ICEMS)*, pages 1–6. IEEE, October 2018.
- Guillaume Burnand, Adrien Thabius, Douglas Martins Araujo and Yves Perriard. Novel optimized shape and topology for slotless windings in BLDC machines. In *IEEE Transactions on Industry Applications*, 2019.

## 7.1 Introduction

One of the biggest benefits of slotless windings (also called self-supporting windings) compared with slotted windings, is the many possible topologies and shapes they can embrace. The most common windings are skewed and rhombic windings (see Section 2.5). Usually, they are wound with round section wires. Contrary to slotted windings forced to follow the direction of the slots, slotless windings can be freely placed in the airgap. This represents great potential for optimisation.

Nonetheless, little research has been performed on this topic. Linder *et al.* have manufactured a self-supporting winding with 3D screen printing [50]. They have mentioned the idea of using nonconstant wire section without however, optimising the shape [51]. Dehez *et al.* have investigated a flexible PCB winding for slotless machines with nonconstant tracks width [54]. In [55], they have demonstrated the significant increase of the performances of a motor thanks to an optimal track shape. These researches have eventually led the way to nonconstant section windings.

Recent works have focused on additive manufacturing (AM) for electrical machines or components [56, 57] and have shown opportunities in this area. As a result of these emerging technologies, such as selective laser melting (SLM), electron beam melting (EBM) [58, 59], 3D screen printing [51, 60], 3D Multi-Material Printing [52, 53], or more conventional ones, such as wire-cut electrical discharge machining (WEDM) [61] or laser cutting, innovation and enhancement can be considered in the design and manufacturing of windings.

The present chapter intends to challenge the conventional manner of manufacturing windings. Indeed, most of the windings are made with isolated wire of constant section. However, it has been demonstrated by the author in [119] that the performances of a motor can be significantly increased by optimizing the shape of the winding and by choosing nonconstant wire sections. On the one hand, the filling factor is better, since spaces between the coils are filled because of the use of nonconstant wires. On the other hand, the reduction of the width of the wire in the axial direction at the locations of end-winding enables the lengthening of the central part of the coil. This is where the magnetic flux density in the airgap is the highest and where the turns can be oriented in the axial direction to maximise the torque. This last consideration could also be applied to slotted windings.

Section 7.2 gives the topology of the new winding, which derives from preliminary considerations on the production of the electromagnetic torque and end-windings in electrical machines. The geometry and parameters of the new topology are detailed as well as a reference winding used for comparison. The analytical modelling of the new winding is described in Section 7.3. The model is then optimised in Section 7.4, leading to enhanced performances of the motor. The model for the torque constant is validated by 3D FEM. Afterwards, a prototype of the new winding is manufactured in Section 7.5. It enables the experimental validation of the model and demonstrates the technical feasibility of the winding. Finally, Section 7.6 illustrates the implementation of the new winding in both rotating and linear machines.

### 7.2 Winding topology

#### 7.2.1 Preliminary considerations

By the cross product of Laplace forces, it is known that only the radial component of the magnetic flux density in the airgap and the axial component of the current in a coil contribute to a rotating torque. Thereby, to get the maximal electromagnetic torque in a machine, the winding should be straight in the axial direction. However, end-windings have to be considered. They are unavoidable in order to close the electrical loop. Unfortunately, they add electrical resistance to the winding, are located where the magnetic flux density in the airgap is the weakest and have an azimuthal component producing little or no useful torque.

The proposed solution for a new winding is later compared to a classical winding as illustrated in Figure 7.1. It is subsequently named *Reference Winding*. This is a winding composed of 6 coils entangled on 2 layers. Thanks to its 6 coils, it offers the flexibility of being series or parallel connected and delta or star-connected [48]. The coils are made of rectangular wires. This has the benefit of increasing the filling factor as opposed to coils made of round section wires (this fact is demonstrated in Section 5.4). Finally, rectangular wires have a better thermal conductivity in the radial direction.

Nonetheless, rectangular section wires usually have a larger section, which enables more induced currents by the rotation of the field of the PM to flow and thus, more losses. Finally, windings made of constant section wires have the disadvantage that the entire available widthwise space cannot always be filled, as can be visualised in Figure 7.1.

Based on the aforementioned facts, a proposed solution which minimises the drawbacks of end-winding, maximises the axial component of the currents and uses nonconstant wire width is presented hereinbelow.

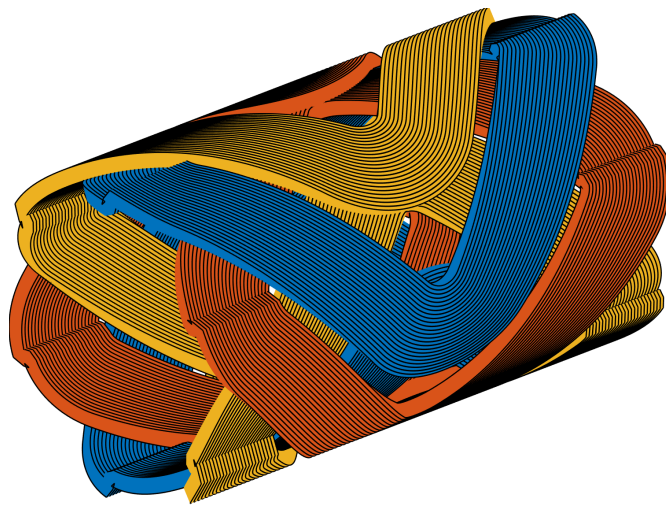


Figure 7.1 – A 3-phase 6-coil slotless winding used as comparison.



### 7.2.2 Geometry and parameters

The new winding topology is sketched in Figure 7.2 for a 3-phase 6-coil 2-layer one pole pair winding. Only one of the six coils and only half of the axial length (axial symmetry) is represented. The total axial length of the coil is  $L_c$ . The coil skims an octagonal shape and is composed of 3 distinct segments:

- segments ① are made of turns in the axial direction with an opening angle  $\beta_c$  and are centred on  $\varphi = \pm \frac{\pi}{2p}$ ,
- segments ② are made of diagonal turns of bend angle  $\alpha_c$  starting at the axial distance  $z_{\text{bend}}$ ,
- segment ③ is made of turns in the azimuthal direction with an opening angle  $\gamma_c$  (end-windings).

As in Figure 7.1, the coil is made of 2 layers of index ① for the top layer and ② for the bottom layer.

In the particular case of Figure 7.2, the angles  $\beta_c = \gamma_c = \frac{\pi}{3}$  and segments ① are centred on  $\varphi = \pm \frac{\pi}{2}$ . Continuous and dashed grey lines are receptively the edges and the centres of the turns. Nevertheless, this can be generalised to any number of coils of  $p$  poles.

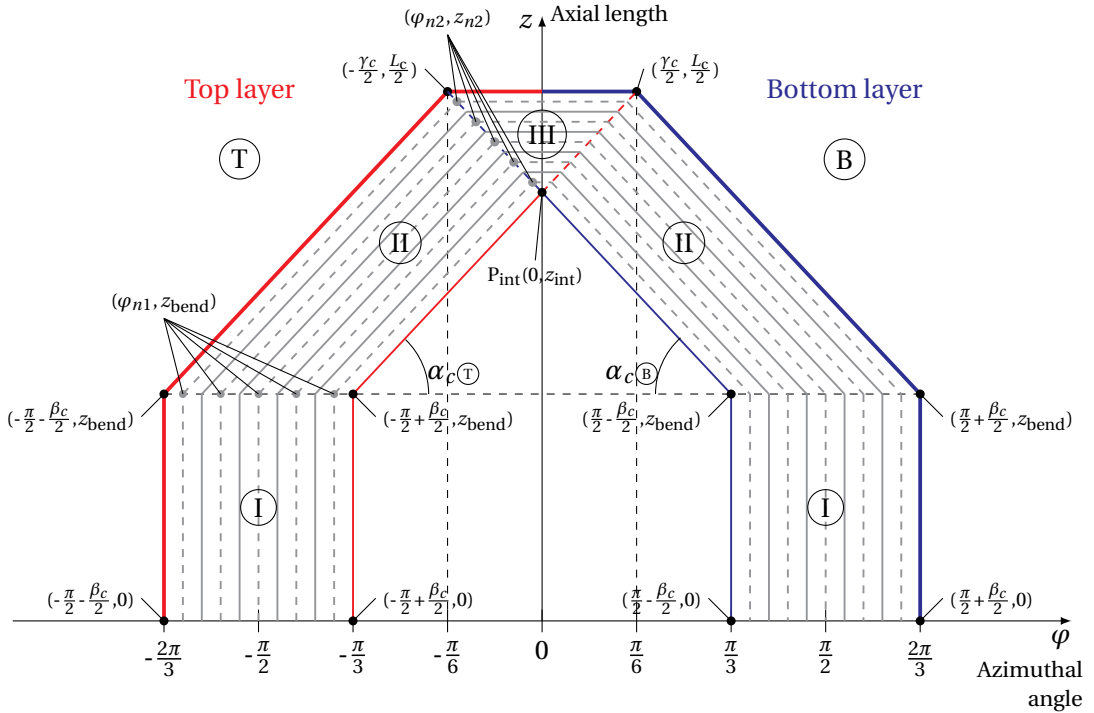


Figure 7.2 – The new slotless winding topology.

The radii at the centre of these layers are given by

$$r_{\textcircled{T}} = \frac{1}{4}r_{\text{ci}} + \frac{3}{4}r_{\text{co}}, \quad (7.1)$$

$$r_{\textcircled{B}} = \frac{3}{4}r_{\text{ci}} + \frac{1}{4}r_{\text{co}}. \quad (7.2)$$

Segment  $\textcircled{\text{III}}$ , which is the end-winding, is where the turns pass from one layer to another, and thus is located on a mean radius equal to

$$\bar{r}_c = \frac{1}{2}r_{\textcircled{T}} + \frac{1}{2}r_{\textcircled{B}}. \quad (7.3)$$

In order to have parallel turns in segments  $\textcircled{\text{II}}$ , and therefore to avoid coils overlapping, the axial coordinate of intersection point  $P_{\text{int}}$  must be equal to

$$z_{\text{int}} = z_{\text{bend}} + \frac{L_c - 2z_{\text{bend}}}{\frac{\pi}{p} + \beta_c - \gamma_c} \left( \frac{\pi}{2p} - \frac{\beta_c}{2} \right). \quad (7.4)$$

Once every edges of the coil is determined, the  $N_t$  turns can be distributed in the segments, as illustrated in Figure 7.2, where continuous and dashed grey lines are respectively the edges and the centres of the turns.

The parameters (dimensions, permanent magnet) of the following model are the same as in Figure 4.1 in Section 4.2.

## 7.3 Modelling

### 7.3.1 Torque constant

The torque constant for one coil  $k'_t$  is defined as

$$T'_{\text{em}} = k'_t I, \quad (7.5)$$

where  $I$  is the DC current in the coil and  $T'_{\text{em}}$  is the RMS electromagnetic torque created by the coil. Only the current flowing in the axial direction and the radial magnetic flux density in the airgap given by (4.7) contribute to a rotating torque. The torque constant  $k'_t$  for one coil is derived from (4.12). Choosing the rotor mechanical angle  $\theta$  creating the maximum torque, the constant can be calculated in cylindrical coordinates by

$$k'_t = \frac{\sqrt{2}}{2} \int_{\partial\Sigma} r B_{\delta r}(r, \varphi) dz, \quad (7.6)$$

where  $\partial\Sigma$  is the path of the coil (at the centre of the wire) as in (4.10). The path of rectangular section wires in slotless machine is known precisely, conversely to round section wires.

The coil is made of  $N_t$  turns of index  $n$ . Thereby, the contribution to the torque constant for segment ① of one layer and, taking into account the axial symmetry, becomes

$$k'_{t①} = \sqrt{2}r z_{\text{bend}} \sum_{n=1}^{N_t} B_{\delta r}(r, \varphi_{n1}), \quad (7.7)$$

where  $r$  is the radius of the layer, namely either  $r_{\text{T}}$  or  $r_{\text{B}}$ .

For segment ② of one layer, after operating a change of variables [54], the contribution to the torque constant becomes

$$k'_{t②} = \sqrt{2}r c_{\delta} \left( 1 + \frac{r_{\text{yi}}^2}{r^2} \right) \cdot \sum_{n=1}^{N_t} (\sin(\varphi_{n2} - \theta) - \sin(\varphi_{n1} - \theta)) \frac{\Delta z_n}{\Delta \varphi_n}, \quad (7.8)$$

where  $r$  is the radius of the layer,  $c_{\delta}$  is the constant depending on the geometry and the properties of the permanent magnet given by (4.4) and with

$$\Delta z_n = z_{n2} - z_{\text{bend}}, \quad (7.9)$$

and

$$\Delta \varphi_n = \varphi_{n2} - \varphi_{n1}. \quad (7.10)$$

Segment ③ does not contribute to the torque constant since it is oriented in the azimuthal direction. Finally, the total torque constant for one coil  $k'_t$  is obtained by taking into account the 2 layers, that is

$$k'_t = k'_{t①\text{T}} + k'_{t②\text{T}} + k'_{t①\text{B}} + k'_{t②\text{B}}. \quad (7.11)$$

In (7.7) and (7.8), the axial length of the permanent magnet  $L_{\text{PM}}$  is assumed to be equal or longer than the length of the coil  $L_c$ . If it is not the case, the integration of (7.6) is assumed to be zero beyond the permanent magnet.

### 7.3.2 Back EMF constant

The back EMF constant for one coil  $k'_e$  has the same numerical value (see Figures 4.6 and 4.7) as the torque constant  $k'_t$  due to the sinusoidal nature of the vector potential in the airgap given by (4.3).

### 7.3.3 Resistance

Similarly to the torque constant, the resistance  $R'$  for one coil is calculated by integration along the wire of the coil, considering the possible variations of the cross-section. It yields to

$$R' = \rho \int_{\partial \Sigma} \frac{dl}{w_w(r, \varphi, z) h_w(r, \varphi, z)}, \quad (7.12)$$

where  $\rho$  is the resistivity of the coil,  $dl$  is an infinitesimal segment along the path of the coil and  $w_w$  and  $h_w$  are respectively the width (in the azimuthal direction) and the height (in the radial direction) of the wire.

The widths of the wire of one layer, which are constant in each segment, are given by

$$w_{w\textcircled{I}} = \frac{\beta_c}{N_t} r - 2e_w, \quad (7.13)$$

$$w_{w\textcircled{II}} = \frac{\beta_c}{N_t} r \sin(\alpha_c) - 2e_w, \quad (7.14)$$

$$w_{w\textcircled{III}} = \frac{\frac{L_c}{2} - z_{\text{int}}}{N_t} - 2e_w, \quad (7.15)$$

where  $e_w$  is the thickness of the insulation of the wire,  $r$  is the radius of the layer, namely  $r_{\textcircled{T}}$  or  $r_{\textcircled{B}}$  and  $\alpha_c$  is the bend angle of segments  $\textcircled{II}$  with the azimuthal axis given by

$$\alpha_c = \arctan \left( \frac{z_{\text{int}} - z_{\text{bend}}}{\left( \frac{\pi}{2p} - \frac{\beta_c}{2} \right) r} \right). \quad (7.16)$$

The height of the wire is constant over a segment. For segments  $\textcircled{I}$  and  $\textcircled{II}$  it is worth

$$h_{w\textcircled{I}} = h_{w\textcircled{II}} = r_{\textcircled{T}} - r_{\textcircled{B}} - 2e_w. \quad (7.17)$$

For segment  $\textcircled{III}$ , given that it is the only place where there is no overlapping of layers, the height of the wire can be doubled. Consequently, it offers more mechanical strength where the width of the wire is the lowest and, in addition, it decreases the resistance.

The resistances of the 3 segments for one layer, taking into account the axial symmetry, are calculated as

$$R'_{\textcircled{\text{I}}} = \frac{2\rho}{w_{\textcircled{\text{I}}} h_{\textcircled{\text{I}}}} N_t z_{\text{bend}}, \quad (7.18)$$

$$R'_{\textcircled{\text{II}}} = \frac{2\rho}{w_{\textcircled{\text{II}}} h_{\textcircled{\text{II}}}} \sum_{n=1}^{N_t} \sqrt{\Delta z_n^2 + (r \Delta \varphi_n)^2}, \quad (7.19)$$

$$R'_{\textcircled{\text{III}}} = \frac{2\rho}{w_{\textcircled{\text{III}}} h_{\textcircled{\text{III}}}} \sum_{n=1}^{N_t} \bar{r}_c \varphi_{n2}. \quad (7.20)$$

Finally, the total resistance for one coil  $R'$  is obtained by taking into account the 2 layers and the 3 segments, leading to

$$R' = R'_{\textcircled{\text{I}}(\text{T})} + R'_{\textcircled{\text{II}}(\text{T})} + R'_{\textcircled{\text{I}}(\text{B})} + R'_{\textcircled{\text{II}}(\text{B})} + R'_{\textcircled{\text{III}}}. \quad (7.21)$$

### 7.3.4 Motor constant

There are several ways to compare electrical motors. However, one of the most popular ones used by motor designers and manufacturers is the motor constant defined as

$$k_m = \frac{T_{\text{em}}}{\sqrt{P_{\text{Joule}}}} = \frac{k_t I_{\text{ph}}}{\sqrt{3 R_{\text{ph}} I_{\text{ph}}^2}} = \frac{k_t}{\sqrt{3 R_{\text{ph}}}}, \quad (7.22)$$

where  $T_{\text{em}}$  is the electromagnetic torque produced by the motor,  $P_{\text{Joule}}$  are the Joule losses,  $R_{\text{ph}}$  is the phase resistance,  $I_{\text{ph}}$  is the phase current and  $k_t$  is the global torque constant. It is valid for a given temperature and without saturation in the magnetic circuit.

The motor constant asserts the torque efficiency. Namely, it links the electromagnetic torque produced by the motor and the corresponding winding losses to produce it [132]. This ratio relies neither on the number of turns (for a constant filling factor) nor on the current. It is also independent of the winding configuration (delta or star-connected). It can serve as a means of comparing motors of the same winding volume and size [54]. Nonetheless, this last fact may be ambitious to verify, as motors may have the same diameter, but barely the same length and/or winding volume.

Given a winding of 6 coils and assuming sinusoidal currents, the global motor constant  $k_m$  can be given in terms of the torque constant for one coil  $k'_t$  and the resistance  $R'$  for one coil with

$$k_m = \frac{\sqrt{6} k'_t}{\sqrt{R'}}. \quad (7.23)$$

### 7.3.5 Winding factor

In electrical machines, the winding factor is used to take into consideration that only a part of the total flux created by the rotor is seen by the winding. For distributed windings in slotted machines, it is defined as the product of the distribution factor and the pitch factor [133]. The first factor is related to the distribution of turns in the slots, which are not subject to the same back EMF voltage. The second factor refers to the reduction of the coil opening that enables the reduction of harmonics.

In slotless machines, the winding factor  $k_w$  can be calculated from the definition of the RMS value of the fundamental of the back EMF voltage, that is

$$^1U_{EMF} = \sqrt{2}\pi N_t k_w f ^1\hat{\Phi}, \quad (7.24)$$

where  $N_t$  is the number of turns for one coil,  $f$  is the electrical frequency and  $^1\hat{\Phi}$  is the fundamental of the peak magnetic flux in the airgap created by a pole of the rotor.

With the help of (6.1), the winding factor is

$$k_w = \frac{^1U_{EMF}}{\sqrt{2}\pi N_t f ^1\hat{\Phi}} = \frac{k_e 2\pi f}{\sqrt{2}\pi p N_t f ^1\hat{\Phi}} = \frac{\sqrt{2}k_e}{p N_t ^1\hat{\Phi}}. \quad (7.25)$$

Equation (7.25) is actually the ratio between the magnetic flux seen by a coil, and the magnetic flux that a coil with  $N_t$  turns and an opening equal to the pole pitch would see.

Considering a single pole pair magnet, the magnetic flux in the airgap is purely sinusoidal. Its peak value (with a given mechanical angle of the rotor that maximises it) can be computed as

$$\hat{\Phi} = 2A_{\delta z}(\bar{r}_c, 0)L_{PM}, \quad (7.26)$$

where  $A_{\delta z}$  is the axial component of the vector potential in the airgap given by (4.3) with the referential for the permanent magnet corresponding to the one of Figure 4.1.

Finally, the winding factor is

$$k_w = \frac{\sqrt{2}k_e}{2N_t A_{\delta z}(\bar{r}_c, 0)L_{PM}}. \quad (7.27)$$

## 7.4 Optimisation

### 7.4.1 Objective function

As explained in Section 7.3.4, the motor constant links the geometry of the winding to the magnetic properties of the motor. Indeed, the torque constant for one coil  $k'_t$  relies on the magnetic flux density in the airgap, which relies on the permanent magnet and the magnetic circuit, but also on the path of the coil. For its part, the resistance for one coil  $R'$  depends on the length and the section of the coil and its material. As a result, the motor constant is a very appropriate choice for optimisation and the objective function to be maximised is (7.23).

### 7.4.2 Optimisation framework

The geometry of the new topology has very few variables to be optimised and has the convenience of being easily implemented and giving fast results. The design variables are:

- $\beta_c$  the opening angle of segments ①,
- $\gamma_c$  the opening angle of end-windings,
- $z_{\text{bend}}$  the axial distance where the bend of segments ② starts.

The total axial length of the coil  $L_c$  along with the radii of layers  $r_{\text{T}}$  and  $r_{\text{B}}$  are set equal to those of Reference Winding in order to have the same available volume. The number of turns per coil  $N_t$  has been set to 16 in order to have the torque constant as close as possible to that of Reference Winding. The insulation thickness of the wire  $e_w$  is also the same and is worth 13  $\mu\text{m}$ . The other parameters of the motor employed are listed in Table 7.1.

The optimisation algorithm used here is a conjugate gradient method with the Matlab function *fmincon*. Variables  $\beta_c$  and  $\gamma_c$  are bound to a maximal value of  $58^\circ$  for mechanical assembly reasons. In order to guarantee the mechanical strength of segment ③, which is the narrowest, a constraint on the width of the wire has been set. It should not be less than 0.2 mm.

Conversely to the global optimisation in Chapter 5, where the winding and the rest of the motor are optimised as a whole, here only the winding is considered. The purpose is to compare the performances of 2 windings having the same magnetic conditions and an equivalent available volume.

### 7.4.3 Results

As previously highlighted, the height of the wire in segment ③ can adopt either the height of the wire in segments ① and segments ② (given by (7.17)) or twice this value. In the first case, the optimised winding is referred to as *Winding 1* and, in the second case, as *Winding 2*. The results obtained in 3D can be visualised respectively in Figures 7.3a and 7.3b.

Parameters			
PM remanence	$B_r$	1.17	[T]
PM permeability	$\mu_r$	1.05	[-]
Stator material saturation	$B_{sat}$	1.6	[T]
Coil resistivity	$\rho$	$18 \times 10^{-9}$	[ $\Omega m$ ]
Number of turns per coil	$N_t$	16	[-]
Dimensions			
Inner magnet radius	$r_{mi}$	2.5	[mm]
Outer magnet radius	$r_{mo}$	7.5	[mm]
Inner coil radius	$r_{ci}$	8.25	[mm]
Outer coil radius	$r_{co}$	10.35	[mm]
Inner yoke radius	$r_{yi}$	10.75	[mm]
Outer yoke radius	$r_{yo}$	14.3	[mm]
Wires insulation	$e_w$	13	[ $\mu m$ ]
Coil axial length	$L_c$	39	[mm]
PM axial length	$L_{PM}$	33	[mm]
Stator length	$L_{stat}$	36	[mm]
Motor diameter	$d_{mot}$	30	[mm]

Table 7.1 – Parameters and dimensions of the motor used for the theoretical and experimental validation of the new winding topology model.

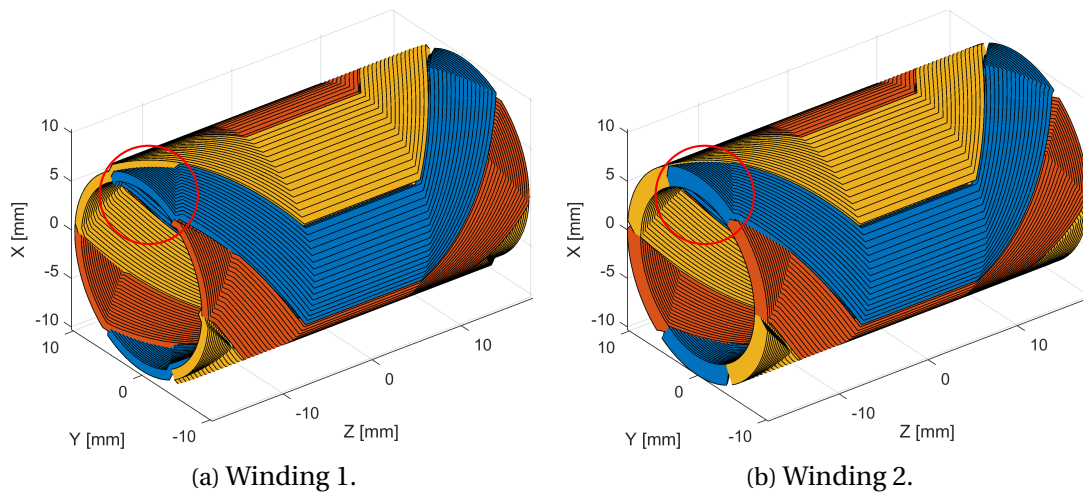


Figure 7.3 – Results after optimisation of the new windings. Red circles highlight the difference between the heights of the wire at the location of end-windings.



For Winding 1, the optimal values of the design variables are  $z_{\text{bend}} = 6.2$  mm and  $\beta_c = \gamma_c = 58^\circ$ . Angles  $\beta_c$  and  $\gamma_c$  have been pushed to their maximal values. This fact has already been pointed out in Section 5.3.2.

For Winding 2, the optimal value of the axial distance where the bend of segments (II) starts is  $z_{\text{bend}} = 6.5$  mm and the angles  $\beta_c$  and  $\gamma_c$  are the same than in Winding 1. Table 7.2 gives the values of the resistance and the torque constant for one coil and the corresponding global motor constant.

In the case of Winding 1, the resistance for one coil is lower by almost 25% compared to Reference Winding, because of the use of non-constant wire sections. Given that the number of turns has been set to have the torque constant for one coil as close as possible to Reference Winding, the motor constant is increased by 15.5%.

For Winding 2, because the height of the wire in segment (III) is doubled, the resistance for one coil has been decreased by 27% in comparison with the Reference Winding. Accordingly, the torque constant for one coil and the motor constant have been increased respectively by 0.88% and 18%.

Figures 7.4 and 7.5 show respectively the resistance for one coil and the global motor constant  $k_m$  with respect to the axial distance  $z_{\text{bend}}$  and with  $\beta_c = \gamma_c = 58^\circ$ . In Figure 7.5, the contribution of each segment is detailed. The longer the distance  $z_{\text{bend}}$  the higher is the resistance, because the width of the wires of segments (II) and segment (III) become narrower. The dominant contribution comes from segments (II), due to their lengths. The dashed lines represent Winding 2, where the height of the wire of end-winding has been doubled. As a consequence, the total resistance is diminished.

One can note a maximal value of the global motor constant  $k_m$  with respect to  $z_{\text{bend}}$  in Figure 7.5. Indeed, after the optimal value  $z_{\text{bend}}$ , the resistance becomes too high. This makes the motor constant drop. In red, the height of the wire of end-winding has been doubled. The maximal value of each curve is not the same. As mentioned earlier, this value slightly changes between Winding 1 and Winding 2.

	$R'$ [mΩ]	$k'_t$ [mNm/A]	$k_m$ [mNm/√W]
Reference Winding	98.63	3.41	26.57
Winding 1	74.23 (-24.7%)	3.41 (0%)	30.68 (15.5%)
Winding 2	71.93 (-27.1%)	3.44 (0.88%)	31.39 (18.1%)

Table 7.2 – Results of the optimisation.

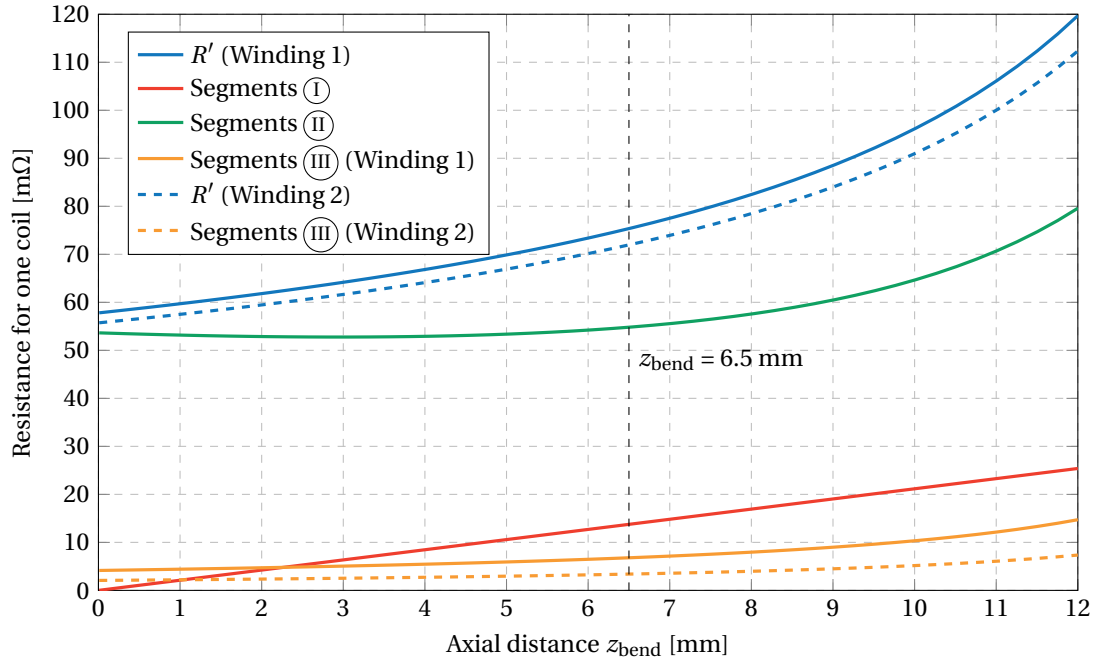


Figure 7.4 – Resistance for one coil with respect to the axial distance  $z_{\text{bend}}$ .

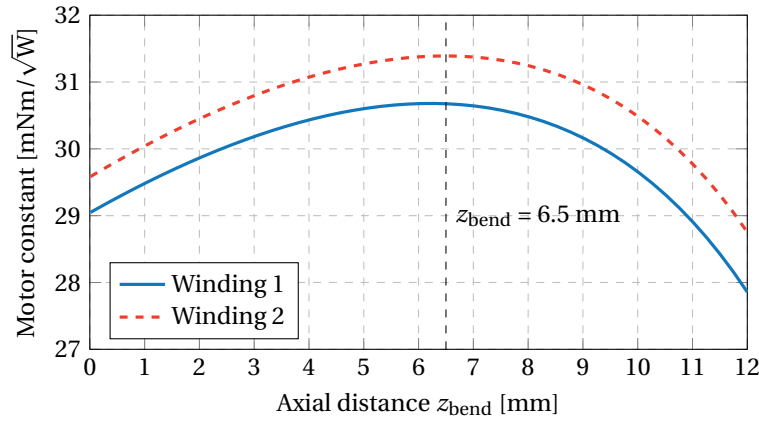


Figure 7.5 – Motor constant with respect to the axial distance  $z_{\text{bend}}$ .

#### 7.4.4 3D FEM validation

The coordinates of the path of the coil (centre of the turns) for Winding 1 are exported into 3D Altair Flux for the validation of the torque constant for one coil. This is sketched in Figure 7.6. The electromagnetic torque produced with respect to the mechanical angle of the rotor is plotted in Figure 7.7. The DC current in the coil is 1 A. Thereby, the RMS value of this curve gives the torque constant for one coil  $k'_t$  as defined by (7.5). The conditions of simulation are strictly identical to the analytical model, leading to a maximal error of 4.5%. The difference comes from the fact that 3D FEM takes into account the end effects of the rotor and the magnetic saturation of the stator.

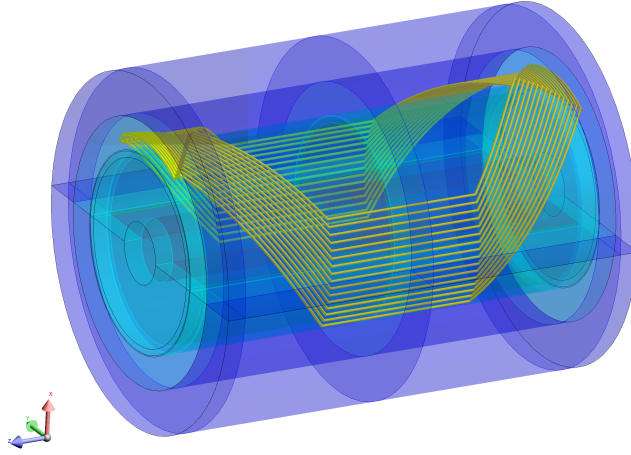


Figure 7.6 – 3D FEM model of the new winding topology with a non-mesh coil in Altair Flux.

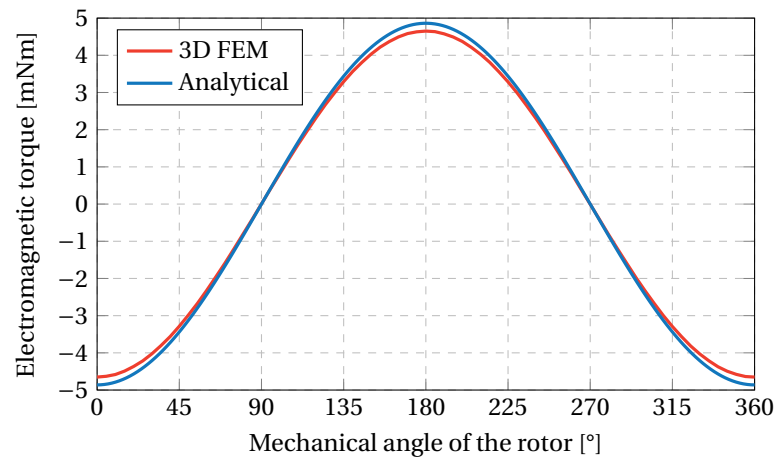
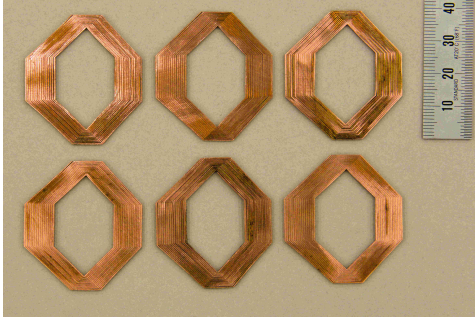


Figure 7.7 – Comparison of the electromagnetic torque in one coil between analytical and 3D FEM models.

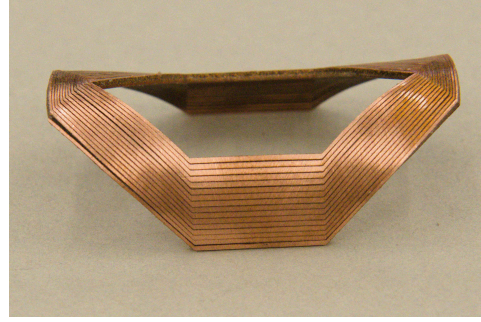
## 7.5 Prototype and measurements

### 7.5.1 Realisation of the prototype

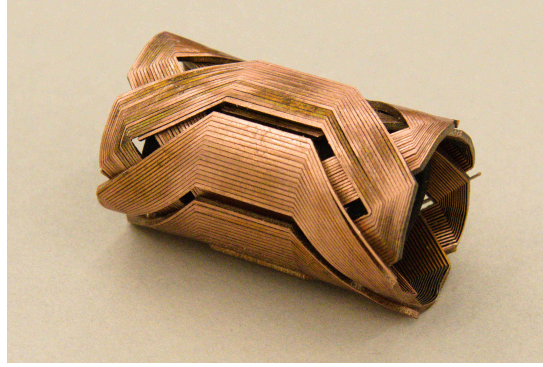
A prototype of the new winding with 6 coils has been manufactured. The dimensions are the same as Winding 1. The coils have been laser cut from a 1 mm sheet of copper as pictured in Figure 7.8a. The drawing is available in Appendix C. Afterwards, the coils have been coated with an isolated resin for electrical windings to avoid short-circuits between the turns and the coils. Lastly, each coil has been curved on a dedicated tool, which gives the 2 necessary radii of curvature to the coils. One of the coil obtained after rolling is visible in Figure 7.8b.



(a) Laser-cutting of the 6 coils.



(b) A coil after rolling.



(c) Assembly of the 6 coils.

Figure 7.8 – Manufacturing of the new winding prototype.

For the sake of simplicity, connecting wires have been welded at each terminal of the coils. However, one could consider lengthening the wires at the extremities of the coils and using them as output wires like in Figure 7.10a. In this case, all connecting wires would be on the same side and could be welded on a ring shape PCB. The latter would be used as a holder to maintain the coils together, but also to configure the connection of phases (series or parallel-connection and delta or star-connection). Finally, the 6 coils are assembled as visible in Figure 7.8c.

### 7.5.2 Experimental validation

#### Resistance measurement

The resistances of the manufactured coils have been obtained with 4-wire measurements. The average value is  $R'_{\text{meas}} = 79 \text{ m}\Omega$ , whereas the theoretical value for Winding 1 is  $R' = 74.23 \text{ m}\Omega$ . This gives an error of -6%. The widths of wires have been measured (see Table 7.3). The slight difference between the theoretical and the measured values is due to the width of the laser groove. This width was a bit more than expected, which explains why the measured values are lower.

	Theoretical [mm]	Measured [mm]
$w_{w(I)T}$	0.59	0.53
$w_{w(I)B}$	0.53	0.49
$w_{w(II)T}$	0.35	0.34
$w_{w(II)B}$	0.34	0.33
$w_{w(III)}$	0.21	0.21

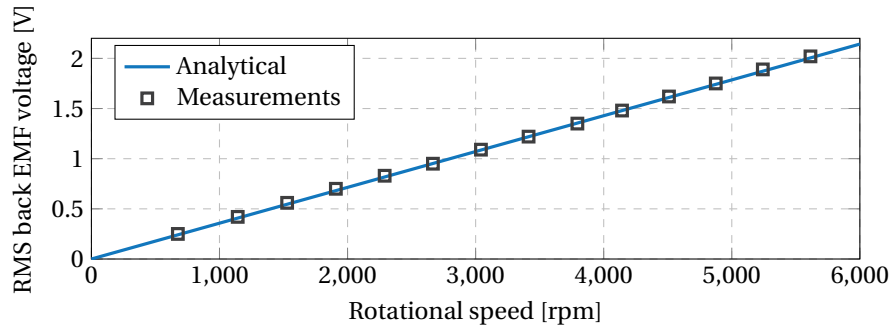
Table 7.3 – Average wire widths measurements of the new winding prototype.

### Torque constant measurement

The winding has been inserted into a motor with the dimensions and characteristics shown in Table 7.1. The measured motor has been driven by another motor. The back EMF voltage has been measured on the coils at several rotational speeds. The measurements of one of the coil are plotted in Figure 7.9. As previously mentioned in Section 4.3.5, the back EMF constant and the torque constant for one coil have the same numerical value. This is because of the sinusoidal nature of the magnetic flux density in the airgap. The average value gives a torque constant for one coil  $k'_{t\, meas} = 3.21$  mNm/A. The theoretical value given by the analytical model is  $k'_t = 3.41$  mNm/A, namely an error of 6%.

The variation may come from a slight difference in the geometry of the coils between the model and the prototype. Alternatively, the remanence of the permanent magnet could diverge slightly from the value given by the manufacturer. The same could apply to the magnetic characteristics of the stator yoke. This could also be an axial misalignment of the coils in the motor. Nevertheless, the discrepancy is low enough to experimentally validate the model.

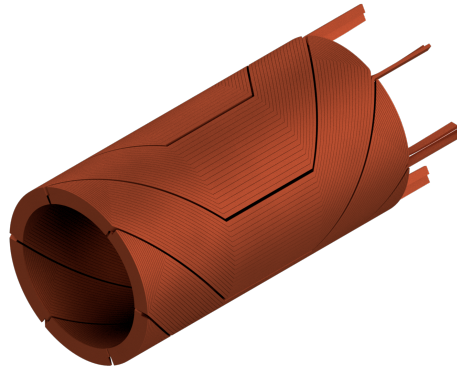
As a result, the global motor constant deduced from the measured values is  $k_{m\, meas} = 27.8$  mNm/ $\sqrt{W}$ , that is an error of -9.6% compared to the theoretical model of Winding 1 (see Table 7.2).

Figure 7.9 – Experimental validation of the coil torque constant for one coil  $k'_t$  with respect to the rotational speed.

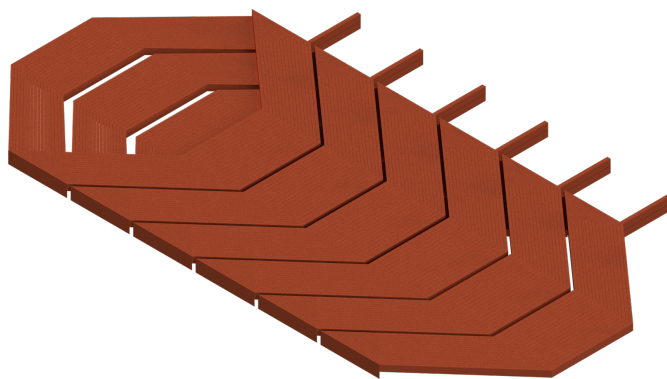
### 7.6 Implementation in rotating and linear machines

Figure 7.10a illustrates the new winding topology for rotating machines with output terminals all on the same side. The advantage of the proposed topology is that it can also be adapted to linear structures, as depicted in Figure 7.10b. Similarly to slotless rotating motors, slotless linear machines exist. The coils can be part of the moving part. In this case, the motors benefit from low mass moving parts and therefore a high dynamic (electrodynamics) compared to slotted ones [134].

The use of nonconstant wire sections at the location of end-windings entails the shortening of end-windings in the axial direction (reduction of the width of wires). It enables the extension of the central part of the coils to maximise the electromagnetic torque. This concept could even be implemented in slotted machines. As a result, by keeping the same external dimensions, the power density of the machine is increased.



(a) Rotating motor.



(b) Linear motor.

Figure 7.10 – Implementation of the new winding topology.

## 7.7 Conclusion

A new slotless winding has been presented in this chapter. The shape and topology derive from preliminary considerations on the creation of the electromagnetic torque, end-windings and nonconstant rectangular wire sections. This last point allows the maximisation of the filling factor. The shortening of end-windings in the axial direction (reduction of the width of wires) enables the extension of the central part of the coils to maximise the electromagnetic torque. This concept could even be implemented in slotted machines. In addition, the height of the wires (in the radial direction) at the location of the end-windings has been increased to reduce the resistance. All these facts result in a significant increase of the motor constant. Indeed, when compared to a classical slotless winding of the same available volume, the motor constant can be increased by 18% up to 24% [135].

The model relies on analytical equations for the computation of the torque constant for one coil and the resistance for one coil. Thus, it can be easily implemented in an optimisation process, which outputs results very quickly. The optimisation has shown that the opening angle  $\beta_c$  of segments ① and the one of end-windings  $\gamma_c$  have to be as large as possible. Consequently, once the number of turns is set, the only remaining quantity to be optimised is the axial distance  $z_{\text{bend}}$  where the bend of segments ② starts.

A 6-coil winding prototype has been manufactured to experimentally validate the model. The coils have been laser cut, isolated and rolled on a dedicated tool. The model of the resistance and the torque constant for one coil show an discrepancy of -6% and 6% respectively compared to measurements. This gives a difference of -9.6% on the theoretical value of the motor constant. These very good results enable the validation of the model presented.

Although the motor constant is used extensively by motor manufacturers, it is not simple to compare the obtained motor constant with other motors or other winding technologies. Indeed, different manufacturers do not always calculate it in the same way. If it is calculated for a sinusoidal excitation or a 120° power supply, the value is not the same. In addition, the volume of the motors and the windings have to be identical. Nevertheless, it has been demonstrated that the motor constant is relevant for the optimisation of windings, because it includes both the geometry of the winding and the magnetic characteristics of the motor.

The presented model could be implemented in a global and multiphysical optimisation of a motor similarly as in Chapter 5. The model for the computation of eddy current losses in rectangular section wires induced by the rotation of the permanent magnet developed in Section 4.4.3 could be added to the model in a multiobjective optimisation. Thus, the torque constant could be maximised and the aforementioned losses minimised.

Finally, more flexibility and more freedom is possible if one deems additive manufacturing and topological optimisation on windings [136] as the new revolutions for the design and manufacturing of electrical machines. It seems that more and more interest is being shown in this direction and that improvement in electrical machines will thrive in a near future.





## 8 Conclusion and outlook

The thesis has addressed the modelling, the design, the optimisation and the experimental validation of small scale very high speed motors. The challenge lies in the reduced dimensions of the motors and the very high speed, which severely constraints both mechanical and electrical aspects. Equally, slotless windings represent a substantial potential of improvement. This thesis comes out with an innovative slotless winding topology increasing the global performances of slotless machines.

Throughout the thesis, the emphasis has been on analytical modelling of very high speed slotless permanent magnet machines. Compared to numerical models, analytical models are preferred, as they bring more insight on the understanding of physical phenomena arising in the machines. Moreover, they are more suited for optimisation given their low computational effort. Finally, they are easily generalisable to any size of slotless permanent magnet machines. Therefore, a complete multiphysics set of both mechanical and electrical analytical models has been presented.

Thanks to these models, a multiphysics optimisation has been carried out. It gives an illustration of the use of the models previously presented by providing them a context: the design of small scale very high speed motors. Constraints on the speed, the mechanical power and the maximal size, combined to a genetic algorithm, result in designs. However, very high speed motors have a lower efficiency than low speed slotless permanent magnet motors. This was explained by the fact that losses do not decrease linearly with the size of the motor, illustrating the difficulty of miniaturised very high speed machines design. Nonetheless, they offer a higher power density leading to a reduction of the size and the weight.

The measurements performed on a small scale prototype up to 475 krpm have enabled the validation of most of the models. To the author's knowledge, it is one of the smallest and fastest electrical motor ever operated. By implementing an astute measurement technique to separate the losses components due to the rotation of the rotor, every of the 4 losses models has been validated and/or obtained independently. It turns out that measurements match the theoretical models very well.

Finally, a novel slotless winding topology has been proposed. The modelling of the topology is detailed and an optimisation outputs a design that has been manufactured. Tests have led to the validation of the theoretical model with high accuracy. Insights into the implementation in slotless rotating and linear machines have been given, as well as into the extension of the topology to slotted windings.

### 8.1 Original contributions

The main contributions brought by this thesis are summarised below:

- *Development and synthesis of slotless permanent magnet motor models*

A very complete set of multiphysics models for the design of slotless permanent magnet motors has been presented. The focus is on very high speed motors. Nevertheless, these models can be easily extended to lower speed motors. Most of them are analytical models and can be split into mechanical and electrical models. Given that the limitation of losses is of the utmost importance in very high speed motors, an emphasis on losses modelling has been made.

Notably, a 3D analytical rotor stresses model distinguishing between cylinder and disc shaped rotors and hollow and solid magnet rotors with the consideration of thermal stresses has been established. Similarly, an analytical model for the computation of induced eddy current losses by the magnetic field of the permanent magnet in rectangular conductors has been developed.

- *Study and comparison of 2 types of conductors and 2 types of magnet rotors for very high speed motors*

An optimisation using the aforementioned analytical models has been performed. The models have been used in the context of small scale very high speed slotless permanent magnet motors design. Several optimisation scenarios involving different rotational speeds have compared Litz-wire to rectangular wires and hollow to solid magnet rotors. With given constraints on the maximal external dimensions and the operating point, it has been observed that Litz-wire features less induced eddy current losses by the magnetic field of the permanent magnet. Nonetheless, at lower speed, Litz-wire does not allow small-scale motors to reach high torque density. The consequence is that more space is used for the winding, leading to a lower airgap and a lower radius of the rotor. When considering the manufacturing and cost aspects of Litz-wire, rectangular wires represent an interesting alternative for small scale very high speed slotless permanent magnet motors.

Similarly, hollow and solid magnet rotors have been compared. From both mechanical and electromagnetic points of view, solid magnet rotors provide better performances than hollow magnet rotors. Indeed, the hole in the magnet weakens the mechanical

strength and reduces its volume. As a result, for a given radius of the shaft, the external diameter of the magnet cannot be reduced as much as possible. This reduction is necessary for both the reduction of losses and to guarantee the mechanical strength of materials. Again, manufacturing considerations make hollow magnet rotors a suitable alternative.

- *Manufacturing of a small scale 400 krpm permanent magnet motor enabling the experimental validation of models*

A 400 krpm 40 W 12.7 mm diameter 28 mm length motor prototype has been manufactured and tested up to 475 krpm. To the author's knowledge, it is one of the smallest and fastest electrical motor ever operated. It has served to validate the models of resistance and inductance of the coils, back EMF constant, critical speeds and losses. With its restricted dimensions, it has also proved that the realisation of small scale very high speed slotless permanent magnet motors is possible.

- *Measurement technique enabling the separation of losses components*

The implementation of a measurement technique has enabled the insulation of the losses components due to the rotation of the rotor in very high speed permanent magnet machines with ball bearings. Thanks to a succession of 4 spin down tests with different configurations, the 4 losses components can be obtained separately. These are the windage losses, the ball bearing losses and the winding and iron losses due to the rotation of the permanent magnet. Therefore, an empirical windage losses model has been validated. In addition, the coefficients of the Jordan's model for the computation of iron losses in a widely used stator material in very high speed machines have been obtained and compared to existing coefficients in the literature review. It has been seen that results differ significantly between coefficients and thus they have to be used with care.

- *Modelling and manufacturing of a novel slotless winding topology*

An innovative slotless winding topology has been devised. The modelling has been validated both numerically with 3D FEM and experimentally with a prototype. Using non-constant wire sections and an optimised shape, the performances of a motor can be increased by up to 24%. The motor constant has been chosen as the evaluation criterion. It entails both the geometry of the winding and the magnetic characteristics of the motor. The main idea behind this novel topology is to reduce the axial width of end-windings and to extend the central part of the winding where the production of the electromagnetic torque is the highest. As a result, for a given external axial length, the power density of the motor is increased. Finally, the topology can be implemented in linear motors and also for slotted windings, following the same principle.

### 8.2 Outlook

This thesis opens perspectives on both theoretical and practical levels. Research can be pursued with some suggested avenues:

- *Acoustic analysis and noise reduction*

Very high speed motors are often operated in speed ranges that are very uncomfortable to the human ear ([2.5-5.5] kHz). Noise is the result of vibrations in the motor. The source of these vibrations may come from the unbalance of the rotor or the phases, the ball bearings, forces between the coils or currents modulation among others. It could be interesting to perform an acoustic analysis and determine the sources of noise. Later on, noise could be reduced using *active noise control* combined to a sensorless power converter.

- *Thermal modelling*

The thermal behaviour of the motor has only been considered indirectly by the minimisation of losses. The complexity lies in the thermal modelling of the airgap and the account of the third dimension. Such a model could be implemented in the optimisation loop giving constraints on the maximal allowed temperature in critical parts of the motor, such as the winding and the permanent magnet.

- *Integration in a system*

In order to be as general as possible, the motor has been isolated from its operating environment. Depending on the application, other design methodologies could be carried out. Other aspects, such as the noise, the mass, the bulk, the costs, the environment (temperature, atmosphere), the power converter and the mechanical load should be considered with a systemic approach.

- *Design and manufacturing of windings and motors*

As a result of the recent and fast development of additive manufacturing, the design and manufacturing of not only winding but also of the whole motor could be rethought. In combination with topology optimisation dedicated to electromagnetism, motors could be manufactured almost entirely with 3D printing: it is already the case, but considerable efforts remain to be made. Additive manufacturing entails previously unthinkable shapes and topologies which would increase the performances and the efficiency of electrical machines.

# A Kelvin functions

## A.1 Kelvin functions of the first kind

The *Kelvin functions* [137] are the solutions of the following differential equation

$$x^2 \frac{d^2 y}{dx^2} + x \frac{dy}{dx} - (jx^2 + \alpha^2)y = 0, \quad (\text{A.1})$$

where  $\alpha \in \mathbb{Z}$  and  $x \in \mathbb{R}^+$ . The Kelvin functions of the first kind of order  $\alpha$  are expressed in terms of the *Bessel functions*  $J$  of the first kind as follows

$$Ber_\alpha(x) = \Re \left\{ J_\alpha \left( x e^{\frac{j3\pi}{4}} \right) \right\}, \quad (\text{A.2})$$

$$Bei_\alpha(x) = \Im \left\{ J_\alpha \left( x e^{\frac{j3\pi}{4}} \right) \right\}, \quad (\text{A.3})$$

where  $J_\alpha$  is the Bessel function of the first kind of order  $\alpha$  and  $\Re$  and  $\Im$  are respectively the real and imaginary parts. For the zero-order, it is common to just denote  $Ber$  and  $Bei$ .

## A.2 Derivatives of Kelvin functions of the first kind

The derivative of Kelvin functions [138] of the first kind of order  $\alpha$  are

$$Ber'_\alpha(x) = \frac{Ber_{\alpha+1}(x) + Bei_{\alpha+1}(x)}{\sqrt{2}} + \frac{\alpha}{x} Ber_\alpha(x), \quad (\text{A.4})$$

$$Bei'_\alpha(x) = \frac{Bei_{\alpha+1}(x) - Ber_{\alpha+1}(x)}{\sqrt{2}} + \frac{\alpha}{x} Bei_\alpha(x). \quad (\text{A.5})$$



## B Calculation of the gradient of the potential

This appendix details the calculation of the gradient of the potential used in the analytical model for the computation of induced current density in a rectangular wire in Section 4.4.3.

The gradient of the potential  $\nabla V$  in (4.24) is calculated from the condition (4.27), that is

$$\int_{y_{wi} - \frac{w_w}{2}}^{y_{wo}} \int_{-\frac{w_w}{2}}^{\frac{w_w}{2}} \nabla V(z) + \frac{\partial A_{\delta z}(x, y)}{\partial t} dx dy = 0, \quad (B.1)$$

which considers the wire as an open-circuit conductor (without an external electrical potential). Given that  $\nabla V$  depends on  $z$  only, it is therefore constant on the  $x$ - $y$  plane and the previous equation becomes

$$\nabla V = -\frac{1}{w_w h_w} \int_{y_{wi} - \frac{w_w}{2}}^{y_{wo}} \int_{-\frac{w_w}{2}}^{\frac{w_w}{2}} \frac{\partial A_{\delta z}(x, y)}{\partial t} dx dy, \quad (B.2)$$

with

$$h_w = y_{wo} - y_{wi}, \quad (B.3)$$

being the height of the wire and  $w_w$  the width of the wire. With the help of (4.26), equation (B.2) is rewritten as

$$\nabla V = \frac{\Omega c_\delta}{w_w h_w} \int_{y_{wi} - \frac{w_w}{2}}^{y_{wo}} \int_{-\frac{w_w}{2}}^{\frac{w_w}{2}} \left( 1 + \frac{r_{yi}^2}{x^2 + y^2} \right) (x \cos(\Omega t) + y \sin(\Omega t)) dx dy. \quad (B.4)$$

## Appendix B. Calculation of the gradient of the potential

---

Integrating on  $x$ , and considering odd functions, gives

$$\begin{aligned}\nabla V &= \frac{\Omega c_\delta}{w_w h_w} \int_{y_{wi}}^{y_{wo}} \left[ x y \sin(\Omega t) + r_{yi}^2 \arctan\left(\frac{x}{y}\right) \sin(\Omega t) \right] \bigg|_{-\frac{w_w}{2}}^{\frac{w_w}{2}} dy \\ &= \frac{\Omega c_\delta}{w_w h_w} \int_{y_{wi}}^{y_{wo}} w_w y \sin(\Omega t) + 2 r_{yi}^2 \arctan\left(\frac{w_w}{2y}\right) \sin(\Omega t) dy.\end{aligned}\tag{B.5}$$

Integrating on  $y$  gives

$$\begin{aligned}\nabla V &= \frac{\Omega c_\delta}{w_w h_w} \left[ \frac{1}{2} w_w y^2 \sin(\Omega t) + 2 r_{yi}^2 \left( \frac{w_w}{4} \ln(w_w^2 + 4y^2) + y \arctan\left(\frac{w_w}{2y}\right) \right) \sin(\Omega t) \right] \bigg|_{y_{wi}}^{y_{wo}} \\ &= \frac{\Omega c_\delta \sin(\Omega t)}{w_w h_w} \left( \frac{1}{2} w_w (y_{wo}^2 - y_{wi}^2) + 2 r_{yi}^2 \left( \frac{w_w}{4} \ln \frac{w_w^2 + 4y_{wo}^2}{w_w^2 + 4y_{wi}^2} + y_{wo} \arctan \frac{w_w}{2y_{wo}} - y_{wi} \arctan \frac{w_w}{2y_{wi}} \right) \right).\end{aligned}\tag{B.6}$$

Finally, this gives the induced current density in a rectangular wire

$$J_z(x, y, t) = \sigma \Omega c_\delta \left( \left( 1 + \frac{r_{yi}^2}{x^2 + y^2} \right) (x \cos(\Omega t) + y \sin(\Omega t)) - c_w \sin(\Omega t) \right),\tag{B.7}$$

with

$$c_w = \frac{1}{w_w h_w} \left( \frac{1}{2} w_w (y_{wo}^2 - y_{wi}^2) + 2 r_{yi}^2 \left( \frac{w_w}{4} \ln \frac{w_w^2 + 4y_{wo}^2}{w_w^2 + 4y_{wi}^2} + y_{wo} \arctan \frac{w_w}{2y_{wo}} - y_{wi} \arctan \frac{w_w}{2y_{wi}} \right) \right),\tag{B.8}$$

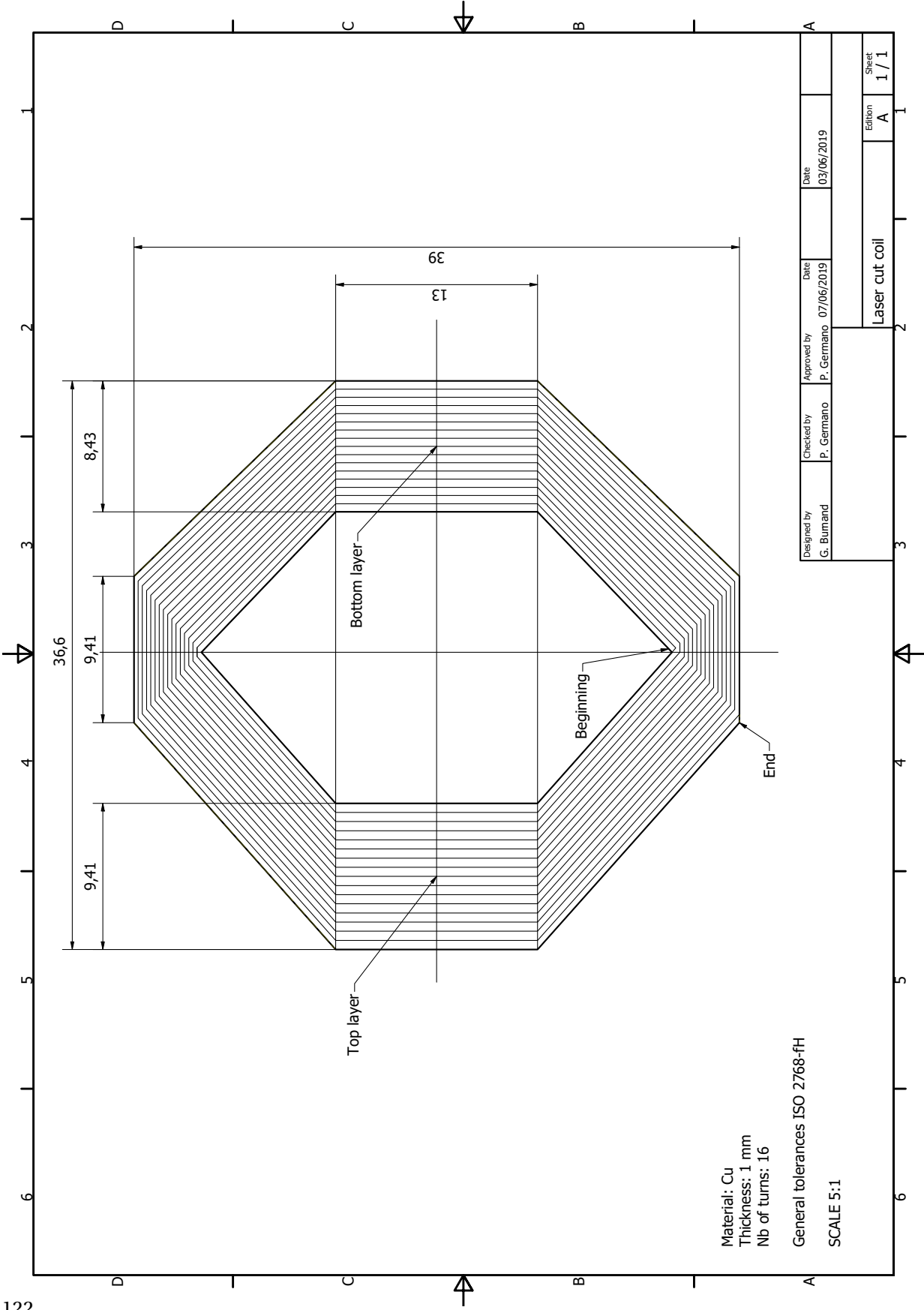
a constant depending on the geometry.



## **C Drawing of the laser-cutting coil**

On the next page, the drawing of the laser-cutting coil is detailed. It represents the path followed by the beam of the laser.

Appendix C. Drawing of the laser-cutting coil



# Nomenclature

## Acronyms

AM	Additive manufacturing
BLDC	Brushless DC
CAD	Computer-aided design
CTE	Coefficient of thermal expansion
EBM	Electron beam melting
EMF	Electromotive force
FEM	Finite element method
GA	Genetic algorithm
HM	Homopolar machines
HS	High speed
IM	Induction machines
LCR	Inductance capacitance resistance
MEMS	Microelectromechanical systems
PAM	Pulse amplitude modulation
PCB	Printed circuit board
PM	Permanent magnet
PMSM	Permanent magnet synchronous machines
PWM	Pulse width modulation
RMS	Root mean square
SLM	Selective laser melting

## Nomenclature

---

SRM	Switched reluctance machines
VHS	Very high speed
WEDM	Wire-cut electrical discharge machining

## Functions and mathematical objects

$Bei_\alpha$	Kelvin-imaginary function of the first kind of order $\alpha$
$Bei'_\alpha$	Derivative of Kelvin-imaginary function of the first kind of order $\alpha$
$Ber_\alpha$	Kelvin-real function of the first kind of order $\alpha$
$Ber'_\alpha$	Derivative of Kelvin-real function of the first kind of order $\alpha$
$G$	Function for the computation of eddy current losses in round conductors
$j$	Imaginary unit
$J_\alpha$	Bessel function of the first kind of order $\alpha$
$\Re$	Real part
$\Im$	Imaginary part
$\nabla$	Nabla or del operator

## Symbols

$A_z$	Axial component of the vector potential	[Wb/m]
$A_{\delta z}$	Axial component of the vector potential in the airgap	[Wb/m]
$\vec{A}$	Vector potential	[Wb/m]
$B_r$	Remanence of the permanent magnet	[T]
$B_r$	Radial component of the magnetic flux density	[T]
$B_{\text{sat}}$	Magnetic flux density saturation	[T]
$B_{\delta r}$	Radial component of the magnetic flux density in the airgap	[T]
$B_{\delta \varphi}$	Tangential component of the magnetic flux density in the airgap	[T]
$B_\varphi$	Tangential component of the magnetic flux density	[T]
$\hat{B}$	Peak magnetic flux density	[T]
$\hat{B}_w$	Peak magnetic flux density in a wire	[T]
$\hat{B}_y$	Peak magnetic flux density in the stator yoke	[T]

$\overline{B_{\delta\max}^2}$	Mean squared value of the peak magnetic flux density in the airgap	[T]
$\vec{B}$	Magnetic flux density vector	[T]
$\vec{B}_{\delta}$	Airgap magnetic flux density vector	[T]
$c$	Constant	
$c$	Coefficient	
$c$	Coefficient in Steinmetz's equation	[W/Hz <sup><math>\alpha</math></sup> /T <sup><math>\beta</math></sup> /m <sup>3</sup> ]
$c$	Coefficient of thermal expansion	[1/°C]
$c_{\text{bearings1}}$	Coefficient of regression for the model of ball bearing losses	[W/rad/s]
$c_{\text{bearings2}}$	Coefficient of regression for the model of ball bearing losses	[-]
$c_e$	Coefficient of thermal expansion of the enclosure	[1/°C]
$c_{\text{eddy}}$	Coefficient for eddy current losses in Jordans's equation	[W/Hz <sup>2</sup> /T <sup>2</sup> /m <sup>3</sup> ]
$c_f$	Friction coefficient	[-]
$c_{\text{hyst}}$	Coefficient for hysteresis losses in Jordans's equation	[W/Hz/T <sup>2</sup> /m <sup>3</sup> ]
$c_{\text{iron1}}$	Coefficient of regression for the model of iron losses	[W/rad/s/T <sup>2</sup> /m <sup>3</sup> ]
$c_{\text{iron2}}$	Coefficient of regression for the model of iron losses	[W/rad <sup>2</sup> /s <sup>2</sup> /T <sup>2</sup> /m <sup>3</sup> ]
$c_{i1}$	Integration constant for the model of mechanical stress with $i=s,m,e$	
$c_{i2}$	Integration constant for the model of mechanical stress with $i=s,m,e$	
$c_m$	Coefficient of thermal expansion of the magnet	[1/°C]
$c_s$	Coefficient of thermal expansion of the shaft	[1/°C]
$c_w$	Constant depending on the geometry of the wire	[m]
$c_{\delta}$	Constant depending on the geometry and the properties of the PM	[T]
$C$	Sutherland temperature	[K]
$C$	Sutherland temperature for air	110.4 [K]
$\mathbf{C}$	Damping matrix	[N s/m]
$d_{\text{mot}}$	Diameter of the motor	[m]
$d_{\text{strand}}$	Diameter of a strand in a Litz-wire	[m]
$d_w$	Diameter of a wire	[m]

## Nomenclature

---

$e$	Operating mechanical interference at the magnet-enclosure interface	[m]
$e_0$	Mechanical interference at standstill and room temperature	[m]
$e_w$	Insulation thickness of a wire	[m]
$E$	Young's modulus	[Pa]
$E_e$	Young's modulus of the enclosure	[Pa]
$E_m$	Young's modulus of the magnet	[Pa]
$E_s$	Young's modulus of the shaft	[Pa]
$\vec{E}$	Electric field vector	[V/m]
$f$	Electrical frequency	[Hz]
$f$	Natural frequency	[Hz]
$f_{1F}$	First forward critical frequency	[Hz]
$f_{2F}$	Second forward critical frequency	[Hz]
$\vec{f}$	Source vector	[N] or [Nm]
$\mathbf{G}$	Gyroscopic matrix	[kg m <sup>2</sup> /s]
$h_w$	Height of a wire	[m]
$h_{w\textcircled{I}}$	Height of a wire of segment I	[m]
$h_{w\textcircled{II}}$	Height of a wire of segment II	[m]
$h_{w\textcircled{III}}$	Height of a wire of segment III	[m]
$I$	Electric current	[A]
$I_l$	Line current	[A]
$I_{ph}$	Phase current	[A]
$J$	Current density	[A/m <sup>2</sup> ]
$J_{rot}$	Inertia of the rotor	[kg m <sup>2</sup> ]
$J_z$	Axial component of the current density	[A/m <sup>2</sup> ]
$\hat{J}$	Peak current density	[A/m <sup>2</sup> ]
$\vec{J}$	Current density vector	[A/m <sup>2</sup> ]
$k_e$	Back EMF constant	[V/rad/s]

$k_{e \text{ meas}}$	Measured back EMF constant	[V/rad/s]
$k'_e$	Back EMF constant for one coil	[V/rad/s]
$k_f$	Filling factor	[-]
$k_m$	Motor constant	[Nm/ $\sqrt{W}$ ]
$k_{m \text{ meas}}$	Measured motor constant	[Nm/ $\sqrt{W}$ ]
$k_s$	Stacking factor	[-]
$k_t$	Torque constant	[Nm/A]
$k'_{t \text{ meas}}$	Measured torque constant for one coil	[Nm/A]
$k'_t$	Torque constant for one coil	[Nm/A]
$k'_{t(I)B}$	Contribution of bottom layer segment I to the torque constant	[Nm/A]
$k'_{t(II)B}$	Contribution of bottom layer segment II to the torque constant	[Nm/A]
$k'_{t(I)T}$	Contribution of top layer segment I to the torque constant	[Nm/A]
$k'_{t(II)T}$	Contribution of top layer segment II to the torque constant	[Nm/A]
$k_w$	Winding factor	[-]
$\mathbf{K}$	Stiffness matrix	[N/m]
$L_c$	Axial length of a coil	[m]
$L_{\text{mot}}$	Axial length of the motor	[m]
$L_{\text{PM}}$	Axial length of the permanent magnet	[m]
$L_{\text{stat}}$	Axial length of the stator	[m]
$L_\delta$	Airgap axial length	[m]
$M$	Molar mass	[kg/mol]
$M_{\text{air}}$	Molar mass of air	0.0289647 [kg/mol]
$\mathbf{M}$	Mass and inertia matrix	[kg] or [kg m <sup>2</sup> ]
$N$	Rotational speed	[rpm]
$N_{\text{max}}$	Maximal rotational speed	[rpm]
$N_{\text{strand}}$	Number of strands in a Litz-wire	[-]
$N_t$	Number of turns per coil	[-]

## Nomenclature

---

$p$	Pole-pair number	[-]
$P$	Absolute pressure	[Pa]
$P_{\text{bearings}}$	Ball bearing losses	[W]
$P_{\text{el}}$	Electrical power	[W]
$P_{\text{em}}$	Electromagnetic power	[W]
$P_{\text{ironI}}$	Iron losses due to stator currents	[W]
$P_{\text{ironPM}}$	Iron losses due to the permanent magnet	[W]
$P'_{\text{iron}}$	Iron losses per unit volume	[W]
$P_{\text{Joule}}$	Joule losses in the winding	[W]
$P_{\text{Joule+skin}}$	Joule and skin effect losses in the winding	[W]
$P_{\text{mec}}$	Mechanical power	[W]
$P_{\text{prox}}$	Proximity effect losses in the winding	[W]
$P_{\text{rot}}$	Induced eddy current losses in the rotor	[W]
$P_{\text{skin}}$	Skin effect losses in the winding	[W]
$P_{\text{windage}}$	Windage losses	[W]
$P_{\text{winding}}$	Total winding losses	[W]
$P_{\text{windingPM}}$	Eddy current losses in the winding due to the permanent magnet	[W]
$P'_{\text{windingPM}}$	Eddy current losses in the winding due to the perm. magnet per unit length	[W]
$P'_{\text{wirePM}}$	Eddy current losses in a wire due to the permanent magnet per unit length	[W]
$r$	Radius	[m]
$r$	Radial cylindrical coordinate	[m]
$r_{\text{ci}}$	Inner radius of a coil	[m]
$r_{\text{co}}$	Outer radius of a coil	[m]
$r_{\text{ei}}$	Inner radius of the enclosure	[m]
$r_{\text{eo}}$	Outer radius of the enclosure	[m]
$r_{\text{mi}}$	Inner radius of the magnet	[m]
$r_{\text{mo}}$	Outer radius of the magnet	[m]



$r_{so}$	Outer radius of the shaft	[m]
$r_{\textcircled{B}}$	Radius at the centre of the bottom layer of a coil	[m]
$r_{\textcircled{T}}$	Radius at the centre of the top layer of a coil	[m]
$\bar{r}_c$	Mean radius of a coil	[m]
$R$	Ideal gas constant	8.3144621 [J/K/mol]
$R$	Resistance	[ $\Omega$ ]
$R'$	Resistance for one coil	[ $\Omega$ ]
$R'_{\text{meas}}$	Resistance for one coil	[ $\Omega$ ]
$R_{\text{ph}}$	Phase resistance	[ $\Omega$ ]
$R_{\text{ph-ph}}$	Phase-to-phase resistance	[ $\Omega$ ]
$R'_{\text{t(I)B}}$	Contribution of the bottom layer of segment I to the resistance	[ $\Omega$ ]
$R'_{\text{t(II)B}}$	Contribution of the bottom layer of segment II to the resistance	[ $\Omega$ ]
$R'_{\text{t(IT)}}$	Contribution of the top layer of segment I to the resistance for one coil	[ $\Omega$ ]
$R'_{\text{t(ITT)}}$	Contribution of the top layer of segment II to the resistance	[ $\Omega$ ]
$R'_{\text{t(III)}}$	Contribution of segment III to the resistance	[ $\Omega$ ]
$Re$	Couette-Reynolds number	[-]
$S_c$	Half the section of a coil	[m <sup>2</sup> ]
$S_w$	Section of a wire	[m <sup>2</sup> ]
$T$	Temperature	[°C] or [K]
$T$	Time period	[s]
$T'_{\text{em}}$	Electromagnetic torque for one coil	[Nm]
$T_{\text{em}}$	Electromagnetic torque	[Nm]
$T_{\text{mot}}$	Temperature of the motor	[°C] or [K]
$T_0$	Reference temperature for Sutherland's law	273.15 [K]
$\hat{T}'_{\text{em}}$	Peak electromagnetic torque for one coil	[Nm]
$Ta$	Taylor number	[-]
$u$	Instantaneous voltage	[V]

## Nomenclature

---

$u$	Mechanical displacement	[m]
$u_e^\Omega$	Mechanical displacement of the enclosure at speed $\Omega$	[m]
$u_{ei}^\Omega$	Mechanical displacement at the inner radius of the enclosure at speed $\Omega$	[m]
$u_m^\Omega$	Mechanical displacement of the magnet at speed $\Omega$	[m]
$u_{mo}^\Omega$	Mechanical displacement at the outer radius of the magnet at speed $\Omega$	[m]
$u_s$	Mechanical displacement of the shaft	[m]
$\vec{u}$	Mechanical displacement vector	[m] or [rad]
$U_{EMF}$	RMS back EMF voltage	[V]
$U_{EMFmax}$	Maximal RMS back EMF voltage	[V]
$^1U_{EMF}$	Fundamental of the RMS back EMF voltage	[V]
$V$	Electric scalar potential	[V]
$V_c$	Volume of one coil	[m <sup>3</sup> ]
$w_w$	Width of a wire	[m]
$w_{w\textcircled{I}}$	Width of a wire of segment I	[m]
$w_{w\textcircled{II}}$	Width of a wire of segment II	[m]
$w_{w\textcircled{III}}$	Width of a wire of segment III	[m]
$y_{wi}$	Inner distance of a wire	[m]
$y_{wo}$	Outer distance of a wire	[m]
$z$	Axial cylindrical coordinate	[m]
$z_{bend}$	Axial length where starts the bend of a coil	[m]
$z_{int}$	Axial coordinate where top and bottom layers of a coil intersect	[m]
$z_{n2}$	Axial coordinates of one of the extremities of segment II	[m]
$\alpha$	Coefficient in Steinmetz's equation for the frequency	[-]
$\alpha$	Phase of the voltage	[rad]
$\alpha_c$	Bend angle of a coil	[rad]
$\alpha_n$	Opening angle of the turn of index $n$	[rad]
$\alpha_1$	Small opening angle of a coil	[rad]

$\alpha_2$	Large opening angle of a coil	[rad]
$\beta$	Coefficient in Steinmetz's equation for the magnetic flux density	[-]
$\beta_c$	Opening angle of a coil	[rad]
$\gamma$	Relative penetration	[m]
$\gamma_c$	End-winding opening angle of a coil	[rad]
$\delta$	Mechanical airgap	[m]
$\delta_{\text{skin}}$	Skin depth of a conductor	[m]
$\Delta L$	Length difference	[m]
$\Delta T$	Temperature difference	[°C]
$\Delta z_n$	Difference of the axial coordinates of the extremities of segment II	[m]
$\Delta \varphi_n$	Difference of the tangential coordinates of the extremities of segment II	[rad]
$\varepsilon$	Mechanical strain	[-]
$\varepsilon_z$	Axial strain component	[-]
$\eta$	Efficiency	[-]
$\theta$	Mechanical angle of the rotor	[rad]
$\mu$	Dynamic viscosity	[Pa s]
$\mu$	Magnetic permeability	[H/m]
$\mu_r$	Relative permeability of the permanent magnet	[-]
$\mu_0$	Dynamic viscosity for air at temperature $T_0$	$17.16 \times 10^{-6}$ [kg/m/s]
$\nu$	Kinematic viscosity	[m <sup>2</sup> /s]
$\nu$	Poisson's ratio	[-]
$\nu_e$	Poisson's ratio of the enclosure	[-]
$\nu_m$	Poisson's ratio of the magnet	[-]
$\nu_s$	Poisson's ratio of the shaft	[-]
$\rho$	Electrical resistivity	[Ωm]
$\rho$	Density	[kg/m <sup>3</sup> ]
$\rho_e$	Density of the enclosure	[kg/m <sup>3</sup> ]

## Nomenclature

---

$\rho_m$	Density of the magnet	[kg/m <sup>3</sup> ]
$\rho_s$	Density of the shaft	[kg/m <sup>3</sup> ]
$\sigma$	Electrical conductivity	[S/m]
$\sigma$	Mechanical stress	[Pa]
$\sigma_c$	Contact stress at the magnet-enclosure interface	[Pa]
$\sigma_{er}$	Radial stress in the enclosure	[Pa]
$\sigma_{ev}$	Von Mises stress in the enclosure	[Pa]
$\sigma_{ey}$	Yield strength of the enclosure	[Pa]
$\sigma_{ez}$	Axial stress in the enclosure	[Pa]
$\sigma_{e\varphi}$	Tangential stress in the enclosure	[Pa]
$\sigma_{mr}$	Radial stress in the magnet	[Pa]
$\sigma_{mt}$	Ultimate tensile strength of the magnet	[Pa]
$\sigma_{mv}$	Von Mises stress in the magnet	[Pa]
$\sigma_{mz}$	Axial stress in the magnet	[Pa]
$\sigma_{m\varphi}$	Tangential stress in the magnet	[Pa]
$\sigma_r$	Radial stress component	[Pa]
$\sigma_{sr}$	Radial stress in the shaft	[Pa]
$\sigma_{sv}$	Von Mises stress in the shaft	[Pa]
$\sigma_{sy}$	Yield strength of the shaft	[Pa]
$\sigma_{sz}$	Axial stress in the shaft	[Pa]
$\sigma_{s\varphi}$	Tangential stress in the shaft	[Pa]
$\sigma_t$	Ultimate tensile strength	[Pa]
$\sigma_v$	Von Mises stress	[Pa]
$\sigma_y$	Yield strength	[Pa]
$\sigma_z$	Axial stress component	[Pa]
$\sigma_\varphi$	Tangential stress component	[Pa]
$\Sigma P$	Sum of losses	[W]

---

$\varphi$	Tangential cylindrical coordinate	[rad]
$\varphi_{n2}$	Tangential coordinates of one of the extremities of segment II	[rad]
$\varphi_{n1}$	Tangential coordinates of one of the extremities of segment II	[rad]
$\hat{\Phi}$	Peak magnetic flux	[Wb]
$^1\hat{\Phi}$	Fundamental of the peak magnetic flux	[Wb]
$\Psi$	Magnetic flux linkage	[Wb]
$\hat{\Psi}$	Peak magnetic flux linkage	[Wb]
$\omega$	Electrical angular frequency	[rad/s]
$\Omega$	Rotational speed	[rad/s]

### Superscripts

'	Derivative of Kelvin functions
'	For one coil
'	Per unit length
'	Per unit volume
*	Plane strain condition
$\Omega$	At rotational speed $\Omega$

### Subscripts

c	Coil, contact
e	Enclosure
em	Electromagnetic
el	Electrical
i	Inner
$i$	Rotor region
l	Line
m	Magnet
max	Maximal
meas	Measured

## Nomenclature

---

mec	Mechanical
mot	Motor
$n$	Turn index
o	Outer
ph	Phase
ph-ph	Phase-to-phase
PM	Permanent magnet
r	Remanence, relative
$r$	Radial cylindrical coordinate
rot	Rotor
s	Shaft
sat	Saturation
stat	Stator
t	Ultimate tensile
v	Von Mises
w	Wire
y	Yoke, yield
$z$	Axial cylindrical coordinate
$\delta$	Mechanical airgap
$\varphi$	Tangential cylindrical coordinate
ⓑ	Bottom layer
Ⓣ	Top layer
①	Segment I
②	Segment II
③	Segment III

# Bibliography

- [1] Aeristech Ltd. <http://www.aeristech.co.uk/>. [Online; accessed 4-September-2019].
- [2] Electromag SA. <https://www.electromagmotor.com/>. [Online; accessed 4-September-2019].
- [3] Pierre-Daniel Pfister. *Very high-speed slotless permanent-magnet motors: theory, design and validation*. PhD thesis, École Polytechnique Fédérale de Lausanne, Lausanne, 2010.
- [4] S. Jumayev, K. O. Boynov, J. J. H. Paulides, E. A. Lomonova, and J. Pyrhonen. Slotless PM Machines With Skewed Winding Shapes: 3-D Electromagnetic Semianalytical Model. *IEEE Transactions on Magnetics*, 52(11):1–12, November 2016.
- [5] Joanna Szydło. *High speed depth optical scanner*. PhD thesis, École Polytechnique Fédérale de Lausanne, Lausanne, 2000.
- [6] David Gerada, Abdeslam Mebarki, Neil L. Brown, Chris Gerada, Andrea Cavagnino, and Aldo Boglietti. High-Speed Electrical Machines: Technologies, Trends, and Developments. *IEEE Transactions on Industrial Electronics*, 61(6):2946–2959, June 2014.
- [7] W. Gruber, T. Hinterdorfer, H. Sima, A. Schulz, and J. Wassermann. Comparison of different motor-generator sets for long term storage flywheels. In *Power Electronics, Electrical Drives, Automation and Motion (SPEEDAM), 2014 International Symposium on*, pages 161–166. IEEE, 2014.
- [8] Jacek F. Gieras. *Advancements in electric machines*. Power systems. Springer, Dordrecht, 2008.
- [9] R. R. Moghaddam. High Speed Operation of Electrical Machines, a Review on Technology, Benefits and Challenges. In *Energy Conversion Congress and Exposition (ECCE)*. IEEE, 2014.
- [10] C. Zwyssig, J.W. Kolar, and S.D. Round. Megaspeed Drive Systems: Pushing Beyond 1 Million r/min. *IEEE/ASME Transactions on Mechatronics*, 14(5):564–574, October 2009.
- [11] Marcel Jufer. *Traité d'Électricité: Electromécanique*, volume IX. Presses Polytechniques et Universitaires Romandes, Lausanne, 3ème edition, 1995. OCLC: 33417205.

- [12] Aleksandar Borisavljevic. *Limits, Modeling and Design of High-Speed Permanent Magnet Machines*. Springer Theses. Springer Berlin Heidelberg, Berlin, Heidelberg, 2013.
- [13] M.A. Rahman, A. Chiba, and T. Fukao. Super High Speed Electrical Machines - Summary. In *Power Engineering Society General Meeting, 2004. IEEE*, pages 1272–1275 Vol.2, June 2004.
- [14] Ma Xiaohe, Su Rong, Tseng King Jet, Wang Shuai, Zhang Xiaolong, Viswanathan Vaiyapuri, Gajanayake Chandana, Gupta Amit, and Nadarajan Sivakumar. Review of high speed electrical machines in gas turbine electrical power generation. In *TENCON - Region 10 Conference*, pages 1–9. IEEE, 2015.
- [15] e+a Elektromaschinen und Antriebe AG. <https://www.eunda.ch/en/>. [Online; accessed 14-August-2019].
- [16] Portescap SA. <https://www.portescap.com/>. [Online; accessed 14-August-2019].
- [17] Maxon Motor AG. <https://www.maxongroup.com/>. [Online; accessed 14-August-2019].
- [18] IBAG Switzerland AG. <http://www.ibag.ch/en/>. [Online; accessed 14-August-2019].
- [19] Celeroton AG. <https://www.celeroton.com/en.html>. [Online; accessed 14-August-2019].
- [20] Air Bearings Limited. <http://www.airbearings.co.uk/en/>. [Online; accessed 14-August-2019].
- [21] Calnetix Technologies. <https://www.calnetix.com/>. [Online; accessed 14-August-2019].
- [22] HEIG-VD (Haute Ecole d’Ingénierie et de Gestion du Canton de Vaud), Institut de Conception, Matériaux, Emballage & Conditionnement (COMATEC). <http://comatec.heig-vd.ch>. [Online; accessed 14-August-2019].
- [23] P. Tsao, M. Senesky, and S.R. Sanders. An integrated flywheel energy storage system with homopolar inductor motor/generator and high-frequency drive. *IEEE Transactions on Industry Applications*, 39(6):1710–1725, November 2003.
- [24] Eric H. Maslen and Gerhard Schweitzer. *Magnetic Bearings*. Springer Berlin Heidelberg, Berlin, Heidelberg, 2009.
- [25] Akira Chiba. *Magnetic bearings and bearingless drives*. Elsevier/Newnes, Amsterdam London, 2005.
- [26] J. Schiffmann and D. Favrat. Integrated Design and Optimization of Gas Bearing Supported Rotors. *Journal of Mechanical Design*, 132(5):051007, 2010.
- [27] Karim Shalash and Jürg Schiffmann. On the manufacturing of compliant foil bearings. *Journal of Manufacturing Processes*, 25:357–368, January 2017.



- [28] Tedric A. Harris and Michael N. Kotzalas. *Rolling bearing analysis - Essential concepts of bearing technology*, volume 1. CRC/Taylor & Francis, Boca Raton, FL, 5th edition, 2007.
- [29] Allen Dowers. The pursuit of higher rotational speeds; developments in bearing design and materials. In *High Speed Bearings for Electrical Machines (Digest No: 1997/164)*, IEE Colloquium on, pages 5–1. IET, 1997.
- [30] Xiaofan Xie. Comparison of Bearings: For the Bearing Choosing of High-speed Spindle Design. *Dept. of Mechanical Engineering, University of Utah*, 2003.
- [31] C. Zwyssig, S. D. Round, and J. W. Kolar. Analytical and experimental investigation of a low torque, ultra-high speed drive system. In *Industry Applications Conference, 41st IAS Annual Meeting*, volume 3, pages 1507–1513. IEEE, 2006.
- [32] M. J. Provost. The More Electric Aero-engine : a general overview from an engine manufacturer. In *Power Electronics, Machines and Drives, 2002. International Conference on (Conf. Publ. No. 487)*, pages 246–251, 2002.
- [33] Guillaume Burnand and Yves Perriard. Very-High-Speed Miniaturized Permanent Magnet Motors: Design and Optimization. In *2019 IEEE Energy Conversion Congress and Exposition (ECCE)*, pages 5258–5264, Baltimore, MD, USA, September 2019. IEEE.
- [34] C. Zwyssig, M. Duerr, D. Hassler, and J. W. Kolar. An Ultra-High-Speed, 500000 rpm, 1 kW Electrical Drive System. In *Power Conversion Conference - Nagoya, 2007. PCC '07*, pages 1577 – 1583, April 2007.
- [35] J. Luomi, C. Zwyssig, A. Looser, and J.W. Kolar. Efficiency Optimization of a 100-W 500000-r/min Permanent-Magnet Machine Including Air-Friction Losses. *IEEE Transactions on Industry Applications*, 45(4):1368–1377, July 2009.
- [36] A. Zahedi and M.R. Movahhedy. Thermo-mechanical modeling of high speed spindles. *Scientia Iranica*, 19(2):282–293, April 2012.
- [37] P.-D. Pfister and Y. Perriard. Very-High-Speed Slotless Permanent-Magnet Motors: Analytical Modeling, Optimization, Design, and Torque Measurement Methods. *IEEE Transactions on Industrial Electronics*, 57(1):296–303, January 2010.
- [38] Juha Saari. *Thermal analysis of high speed induction machines*. PhD thesis, Helsinki University of Technology, Espoo, 1998.
- [39] A. B. Nachouane, A. Abdelli, G. Friedrich, and S. Vivier. Estimation of windage losses inside very narrow air gaps of high speed electrical machines without an internal ventilation using CFD methods. In *2016 XXII International Conference on Electrical Machines (ICEM)*, pages 2704–2710. IEEE, 2016.
- [40] Kevin Anderson, Jun Lin, and Alexander Wong. Experimental and Numerical Study of Windage Losses in the Narrow Gap Region of a High-Speed Electric Motor. *Fluids*, 3(1):22, March 2018.

- [41] N. Bianchi, S. Bolognani, and F. Luise. Potentials and Limits of High-Speed PM Motors. *IEEE Transactions on Industry Applications*, 40(6):1570–1578, November 2004.
- [42] Pierre-Daniel Pfister, Xin Yin, and Youtong Fang. Slotted Permanent-Magnet Machines: General Analytical Model of Magnetic Fields, Torque, Eddy Currents, and Permanent-Magnet Power Losses Including the Diffusion Effect. *IEEE Transactions on Magnetics*, 52(5):1–13, May 2016.
- [43] Kesavan Ramakrishnan, Mitrofan Curti, Damir Zarko, Gianpiero Mastinu, Johannes J. H. Paulides, and Elena A. Lomonova. Comparative analysis of various methods for modelling surface permanent magnet machines. *IET Electric Power Applications*, 11(4):540–547, April 2017.
- [44] A. Looser, T. Baumgartner, C. Zwyssig, and J. W. Kolar. Analysis and measurement of 3d torque and forces for permanent magnet motors with slotless windings. In *Energy Conversion Congress and Exposition (ECCE)*, pages 3792–3797. IEEE, 2010.
- [45] Juha Pyrhonen, Tapani Jokinen, and Valeria Hrabovcová. *Design of rotating electrical machines*. Wiley, Chichester, West Sussex, United Kingdom, 2nd edition, 2014.
- [46] B. D. Cullity and C. D. Graham. *Introduction to magnetic materials*. IEEE/Wiley, Hoboken, N.J, 2nd edition, 2009.
- [47] Marguerite Kudelski. *Analyse et conception de moteurs synchrones chemisés à commutation électronique*. PhD thesis, École Polytechnique Fédérale de Lausanne, Lausanne, Suisse, 1998.
- [48] Florian Louis Copt. *Integrated approach for auto-adaptive synchronous motor winding*. PhD thesis, École Polytechnique Fédérale de Lausanne, Lausanne, 2018.
- [49] A. Borisavljevic, S. Jumayev, and E. Lomonova. Toroidally-wound permanent magnet machines in high-speed applications. In *2014 International Conference on Electrical Machines (ICEM)*, pages 2588–2593, Berlin, Germany, September 2014. IEEE.
- [50] Mathias Lindner, Patrick Brauer, and Ralf Werner. Increasing the Torque Density of Permanent-Magnet Synchronous Machines using Innovative Materials and Winding Technologies. In *International Multi-Conference on Systems, Signals & Devices*, page 7, March 2012.
- [51] Patrick Brauer, Mathias Lindner, Thomas Studnitzky, Berd Kieback, Johannes Rudolph, Ralf Werner, and Gerd Krause. 3-D Screen Printing technology - Opportunities to use revolutionary materials and machine designs. In *2nd International Electric Drives Production Conference (EDPC)*, pages 1–5. IEEE, October 2012.
- [52] F. Lorenz, J. Rudolph, and Ralf Werner. Design of 3d Printed High Performance Windings for Switched Reluctance Machines. In *2018 XIII International Conference on Electrical Machines (ICEM)*, pages 2451–2457, Alexandroupoli, September 2018. IEEE.

- [53] Fabian Lorenz, Johannes Rudolph, and Ralf Werner. High Temperature Operation and Increased Cooling Capabilities of Switched Reluctance Machines using 3d Printed Ceramic Insulated Coils. In *2018 IEEE Transportation Electrification Conference and Expo (ITEC)*, pages 400–405, Long Beach, CA, USA, June 2018. IEEE.
- [54] Bruno Dehez, François Baudart, Miroslav Markovic, and Yves Perriard. Theoretical and Experimental Investigation of Flex-PCB Air-Gap Windings in Slotless BLDC Machines. *IEEE Transactions on Industry Applications*, 50(5):3153–3160, September 2014.
- [55] Bruno Dehez, François Baudart, and Yves Perriard. Analysis of a new topology of flexible PCB winding for slotless BLDC machines. In *International Electric Machines and Drives Conference (IEMDC)*. IEEE, May 2017.
- [56] Hyun-Seok Hong, Huai-Cong Liu, Soo-Young Cho, Ju Lee, and Chang-Sung Jin. Design of High-End Synchronous Reluctance Motor Using 3-D Printing Technology. *IEEE Transactions on Magnetics*, 53(6):1–5, June 2017.
- [57] Yi Yan, Jim Moss, Khai D. T. Ngo, Yunhui Mei, and Guo-Quan Lu. Additive Manufacturing of Toroid Inductor for Power Electronics Applications. *IEEE Transactions on Industry Applications*, 53(6):5709–5714, November 2017.
- [58] D.A. Ramirez, L.E. Murr, E. Martinez, D.H. Hernandez, J.L. Martinez, B.I. Machado, F. Medina, P. Frigola, and R.B. Wicker. Novel precipitate–microstructural architecture developed in the fabrication of solid copper components by additive manufacturing using electron beam melting. *Acta Materialia*, 59(10):4088–4099, June 2011.
- [59] P Frigola, O.A. Harryson, T.J. Horn, H.A. West, R.L. Aman, J.M. Rigsbee, D.A. Ramirez, L.E. Murr, F. Medina, R.B. Wicker, and E. Rodriguez. Fabricating Copper Components with Electron Beam Melting. *Advanced Materials & Processes*, 172(7):20–24, June 2014.
- [60] M. Dressler, T. Studnitzky, and B. Kieback. Additive manufacturing using 3-D screen printing. In *International Conference on Electromagnetics in Advanced Applications (ICEAA)*, pages 476–478. IEEE, September 2017.
- [61] S. Debnath, S. Kunar, S. S. Anasane, and B. Bhattacharyya. Non-traditional Micromachining Processes: Opportunities and Challenges. In Golam Kibria, B. Bhattacharyya, and J. Paulo Davim, editors, *Non-traditional Micromachining Processes*, pages 1–59. Springer International Publishing, Cham, 2017.
- [62] Rene Larssonneur. *Design and Control of Active Magnetic Bearing Systems for High Speed Rotation*. PhD thesis, Swiss Federal Institute of Technology Zurich, 1990.
- [63] Christof Zwyssig. *An Ultra-High-Speed Electrical Drive System*. PhD thesis, ETH Zurich, 2008.
- [64] Aleksandar Borisavljevic. *Limits, modeling and design of high-speed permanent magnet machines*. PhD thesis, Delft University, Delft, 2011.

- [65] A. Binder, T. Schneider, and M. Klohr. Fixation of buried and surface-mounted magnets in high-speed permanent-magnet synchronous machines. *IEEE Transactions on Industry Applications*, 42(4):1031–1037, July 2006.
- [66] Fengge Zhang, Guanghui Du, Tianyu Wang, Guangwei Liu, and Wenping Cao. Rotor retaining sleeve design for a 1.12-MW high-speed PM machine. *IEEE Transactions on Industry Applications*, 51(5):3675–3685, 2015.
- [67] Simon Barrans and Levi Mallin. Mechanical Design of Rotors with Surface Mounted Permanent Magnets. In Adel El-Shahat, editor, *Electric Machines for Smart Grids Applications - Design, Simulation and Control*. IntechOpen, December 2018.
- [68] Wenjie Cheng, Zhikai Deng, Ling Xiao, Bin Zhong, and Bo Zhang. Strength analytical solution to ultra-high-speed permanent magnet rotor considering temperature gradient and segmental permanent magnet effect. *Advances in Mechanical Engineering*, 11(4):168781401984203, April 2019.
- [69] André Bazergui. *Résistance des matériaux*. Presses internationales Polytechnique, Montréal, troisième édition, 2002.
- [70] Guillaume Burnand, Douglas Martins Araujo, and Yves Perriard. Very-high-speed permanent magnet motors: Mechanical rotor stresses analytical model. In *IEEE International Electric Machines and Drives Conference (IEMDC)*, pages 1–7. IEEE, May 2017.
- [71] Lin Hua, Xunpeng Qin, Huajie Mao, and Yumin Zhao. Plastic deformation and yield criterion for compressible sintered powder materials. *Journal of Materials Processing Technology*, 180(1-3):174–178, December 2006.
- [72] G. Genta. *Dynamics of rotating systems*. Mechanical engineering. Springer, New York, 2005.
- [73] Jean-Marc Pagnet. *Equilibrage des rotors rigides et flexibles*. Ed. Techniques Ingénieur, 1997.
- [74] Yukio Ishida and Toshio Yamamoto. *Linear and nonlinear rotordynamics: a modern treatment with applications*. Wiley-VCH, Weinheim, 2nd enlarged and improved edition, 2012. OCLC: ocn822958263.
- [75] Grégoire Dormond. *Modal Identification and Modeling of Bearings for Very High-Speed Rotors*. PhD thesis, École Polytechnique Fédérale de Lausanne, Lausanne, 2010.
- [76] Erik Swanson, Chris D. Powell, and Sorin Weissman. A practical review of rotating machinery critical speeds and modes. *Sound and vibration*, 39(5):16–17, 2005.
- [77] Peter R. N Childs. *Rotating flow*. Elsevier, Amsterdam, Boston, 2011.
- [78] David S. Adebayo. *Annular flows and their interaction with a cylindrical probe*. PhD thesis, University of Leicester, 2012.

- 
- [79] J. W. Daily and R. E. Nece. Chamber Dimension Effects on Induced Flow and Frictional Resistance of Enclosed Rotating Disks. *Journal of Basic Engineering*, 82(1):217, 1960.
- [80] Yutaka Yamada. Torque resistance of a flow between rotating co-axial cylinders having axial flow. *Bulletin of JSME*, 5(20):634–642, 1962.
- [81] Manfred Mack. *Luftreibungsverluste bei elektrischen Maschinen kleiner Baugrösse*. PhD thesis, Universität Stuttgart (FH), Stuttgart, 1967.
- [82] James E. Vrancik. *Prediction of windage power loss in alternators*. National Aeronautics and Space Administration (NASA), 1968.
- [83] E. Bilgen and R. Boulos. Functional Dependence of Torque Coefficient of Coaxial Cylinders on Gap Width and Reynolds Numbers. *Journal of Fluids Engineering*, 95(1):122, 1973.
- [84] M.N. Awad and W.J. Martin. Windage loss reduction study for TFTR pulse generator. In *17th IEEE/NPSS Symposium Fusion Engineering*, volume 2, pages 1125–1128, San Diego, CA, USA, 1998. IEEE.
- [85] Guillaume Burnand, Douglas Martins Araujo, Christian Koechli, and Yves Perriard. Validation by measurements of a windage losses model for very-high-speed machines. In *20th International Conference on Electrical Machines and Systems (ICEMS)*, pages 1–4. IEEE, August 2017.
- [86] Jonathan Demierre, Antonio Rubino, and Jürg Schiffmann. Modeling and Experimental Investigation of an Oil-Free Microcompressor-Turbine Unit for an Organic Rankine Cycle Driven Heat Pump. *Journal of Engineering for Gas Turbines and Power*, 137(3):032602, 2015.
- [87] William Sutherland. The viscosity of gases and molecular force. *The London, Edinburgh, and Dublin Philosophical Magazine and Journal of Science*, 36(223):507–531, December 1893.
- [88] Bernd Bossmanns and Jay F. Tu. A Power Flow Model for High Speed Motorized Spindles—Heat Generation Characterization. *Journal of Manufacturing Science and Engineering*, 123(3):494, 2001.
- [89] Co Huynh, Liping Zheng, and Dipjyoti Acharya. Losses in High Speed Permanent Magnet Machines Used in Microturbine Applications. *Journal of Engineering for Gas Turbines and Power*, 131(2):022301, 2009.
- [90] J. Lammeraner and M. Štafl. *Eddy currents*. International scientific series. CRC Press, 1966.
- [91] Richard L. Stoll. *The analysis of eddy currents*. Monographs in electrical and electronic engineering. Clarendon Press, Oxford, 1974.

- [92] J. A. Tegopoulos and E. E. Kriezis. *Eddy currents in linear conducting media*, volume 16 of *Studies in electrical and electronic engineering*. Elsevier, Amsterdam ; New York, 1985.
- [93] J. A. Ferreira. *Electromagnetic modelling of power electronic converters*. The Kluwer international in engineering and computer science. Power electronics and power systems. Kluwer Academic, Boston, 1989.
- [94] Chas.P. Steinmetz. On the law of hysteresis. *Proceedings of the IEEE*, 72(2):197–221, 1984.
- [95] Andreas Krings and Juliette Soulard. Overview and Comparison of Iron Loss Models for Electrical Machines. *Journal of Electrical Engineering*, 10(3):162–169, 2010.
- [96] Z.Q. Zhu, K. Ng, N. Schofield, and D. Howe. Improved analytical modelling of rotor eddy current loss in brushless machines equipped with surface-mounted permanent magnets. *IEEE Proceedings - Electric Power Applications*, 151(6):641, 2004.
- [97] Patrick Ragot. *Modélisation analytique multiphysique pour la conception optimale de moteurs synchrones à aimants permanents*. PhD thesis, École Polytechnique Fédérale de Lausanne, Lausanne, 2008.
- [98] S. Jumayev, K.O. Boynov, E.A. Lomonova, and J. Pyrhonen. High-speed Slotless Permanent Magnet Machines: modelling and design frameworks. In *2018 International Power Electronics Conference (IPEC-Niigata 2018 -ECCE Asia)*, pages 161–168, Niigata, May 2018. IEEE.
- [99] Guillaume François, François Baudart, François Henrotte, and Bruno Dehez. Numerical Investigation of Eddy Current Losses in Airgap PCB Windings of Slotless BLDC Motors. In *21st International Conference on Electrical Machines and Systems (ICEMS)*, pages 1–7. IEEE, October 2018.
- [100] Olivier De La Barriere, Carlo Appino, F. Fiorillo, Carlo Ragusa, Michel Lécrivain, L. Rocchino, H. Ben Ahmed, Mohamed Gabsi, Frédéric Mazaleyrat, and Martino Lobue. Characterization and prediction of magnetic losses in Soft Magnetic Composites under distorted induction waveform. *IEEE Transactions on Magnetics*, 49(4):1318–1326, 2013.
- [101] Daniel Eggers, Simon Steentjes, and Kay Hameyer. Advanced Iron-Loss Estimation for Nonlinear Material Behavior. *IEEE Transactions on Magnetics*, 48(11):3021–3024, November 2012.
- [102] A Schoppa and J Schneider. Influence of the manufacturing process on the magnetic properties of non-oriented electrical steels. *Journal of Magnetism and Magnetic Materials*, page 5, 2000.
- [103] Jonathan Juergens, Bernd Ponick, Oliver Winter, and Antonio Fricasse. Influences of iron loss coefficients estimation on the prediction of iron losses for variable speed motors. In *2015 IEEE International Electric Machines & Drives Conference (IEMDC)*, pages 1254–1259, Coeur d’Alene, ID, May 2015. IEEE.

- 
- [104] Giselher Herzer. Modern soft magnets: Amorphous and nanocrystalline materials. *Acta Materialia*, 61(3):718–734, February 2013.
- [105] Fang Deng and T.W. Nehl. Analytical modeling of eddy-current losses caused by pulse-width-modulation switching in permanent-magnet brushless direct-current motors. *IEEE Transactions on Magnetics*, 34(5):3728–3736, September 1998.
- [106] M. Markovic and Y. Perriard. Analytical Solution for Rotor Eddy-Current Losses in a Slot-less Permanent-Magnet Motor: The Case of Current Sheet Excitation. *IEEE Transactions on Magnetics*, 44(3):386–393, March 2008.
- [107] Jiabin Wang, K Atallah, R Chin, W M Arshad, and H Lendenmann. Rotor Eddy-Current Loss in Permanent-Magnet Brushless AC Machines. *IEEE Transactions on Magnetics*, 46(7):2701–2707, July 2010.
- [108] S. Jumayev, J. J. H. Paulides, K. O. Boynov, J. Pyrhonen, and E. A. Lomonova. 3-D Analytical Model of Helical Winding PM Machines Including Rotor Eddy Currents. *IEEE Transactions on Magnetics*, 52(5):1–8, May 2016.
- [109] Wei Wu, J.B. Dunlop, S.J. Collocott, and B.A. Kalan. Design optimization of a switched reluctance motor by electromagnetic and thermal finite-element analysis. *IEEE Transactions on Magnetics*, 39(5):3334–3336, September 2003.
- [110] Do-Kwan Hong, Tae-Woo Lee, and Yeon-Ho Jeong. Design and Experimental Validation of a High-Speed Electric Turbocharger Motor Considering Variation of the L/D Ratio. *IEEE Transactions on Magnetics*, 54(11):1–4, November 2018.
- [111] Jianning Dong, Yunkai Huang, Long Jin, Heyun Lin, and Hui Yang. Thermal Optimization of a High-Speed Permanent Magnet Motor. *IEEE Transactions on Magnetics*, 50(2):749–752, February 2014.
- [112] Yun Le and Kun Wang. Design and Optimization Method of Magnetic Bearing for High-Speed Motor Considering Eddy Current Effects. *IEEE/ASME Transactions on Mechatronics*, 21(4):2061–2072, August 2016.
- [113] Tsarafidy Raminosoa, Benjamin Blunier, Daniel Fodorean, and Abdellatif Miraoui. Design and Optimization of a Switched Reluctance Motor Driving a Compressor for a PEM Fuel-Cell System for Automotive Applications. *IEEE Transactions on Industrial Electronics*, 57(9):2988–2997, September 2010.
- [114] Yun Le, Jiancheng Fang, and Kun Wang. Design and Optimization of a Radial Magnetic Bearing for High-Speed Motor With Flexible Rotor. *IEEE Transactions on Magnetics*, 51(6):1–13, June 2015.
- [115] Yuanwen Li, Changsheng Zhu, Lijian Wu, and Yuting Zheng. Multi-Objective Optimal Design of High-Speed Surface-Mounted Permanent Magnet Synchronous Motor for Magnetically Levitated Flywheel Energy Storage System. *IEEE Transactions on Magnetics*, pages 1–8, 2019.

## Bibliography

---

- [116] Li Liu, Wenxin Liu, and David A. Cartes. Particle swarm optimization-based parameter identification applied to permanent magnet synchronous motors. *Engineering Applications of Artificial Intelligence*, 21(7):1092–1100, October 2008.
- [117] Metglas, Technical Bulletin of Magnetic Alloy 2605SA1. <https://www.metglas.com/>. [Online; accessed 22-July-2019].
- [118] Christof Zwyssig, Simon D. Round, and Johann W. Kolar. An Ultrahigh-Speed, Low Power Electrical Drive System. *IEEE Transactions on Industrial Electronics*, 55(2):577–585, 2008.
- [119] Guillaume Burnand, Adrien Thabuis, Douglas Martins Araujo, and Yves Perriard. Novel optimized shape and topology for slotless windings in BLDC machines. *IEEE Transactions on Industry Applications*, pages 1–1, 2019.
- [120] Elektrisola, Technical Basics and Calculation. <https://www.elektrisola.com/home.html>. [Online; accessed 19-July-2019].
- [121] Sebastiano Merzaghi. *Analyse et mise en oeuvre d'un moteur électromagnétique micro-fabriqu  *. PhD thesis,   cole Polytechnique F  d  rale de Lausanne, Lausanne, 2010.
- [122] R. Timothy Marler and Jasbir S. Arora. The weighted sum method for multi-objective optimization: new insights. *Structural and Multidisciplinary Optimization*, 41(6):853–862, June 2010.
- [123] H. Mitterhofer, D. Andessner, and W. Amrhein. Analytical and experimental loss examination of a high speed bearingless drive. In *International Symposium on Power Electronics Power Electronics, Electrical Drives, Automation and Motion*, pages 146–151, Sorrento, Italy, June 2012. IEEE.
- [124] Hubert Mitterhofer, Wolfgang Gruber, and Wolfgang Amrhein. On the High Speed Capacity of Bearingless Drives. *IEEE Transactions on Industrial Electronics*, 61(6):3119–3126, June 2014.
- [125] Daniel Steinert, Ivana Kovacevic-Badstubner, Thomas Nussbaumer, and Johann W. Kolar. Loss investigation of slotless bearingless disk drives. In *2015 IEEE Energy Conversion Congress and Exposition (ECCE)*, pages 4418–4424, Montreal, QC, Canada, September 2015. IEEE.
- [126] Pascal Puentener, Marcel Schuck, Daniel Steinert, Thomas Nussbaumer, and Johann Walter Kolar. A 150 000-r/min Bearingless Slice Motor. *IEEE/ASME Transactions on Mechatronics*, 23(6):2963–2967, December 2018.
- [127] Do-Kwan Hong, Dae-Suk Joo, Byung-Chul Woo, Dae-Hyun Koo, and Chan-Woo Ahn. Unbalance Response Analysis and Experimental Validation of an Ultra High Speed Motor-Generator for Microturbine Generators Considering Balancing. *Sensors*, 14(9):16117–16127, August 2014.



- 
- [128] J.D. Ede, Z.Q. Zhu, and D. Howe. Rotor resonances of high-speed permanent-magnet brushless machines. *IEEE Transactions on Industry Applications*, 38(6):1542–1548, November 2002.
- [129] Leif Svensson, Kenneth Frogner, Peter Jeppsson, Tord Cedell, and Mats Andersson. Soft magnetic moldable composites: Properties and applications. *Journal of Magnetism and Magnetic Materials*, 324(18):2717–2722, September 2012.
- [130] Md. Rabiul Islam, Youguang Guo, and Jianguo Zhu. A High-Frequency Link Multilevel Cascaded Medium-Voltage Converter for Direct Grid Integration of Renewable Energy Systems. *IEEE Transactions on Power Electronics*, 29(8):4167–4182, August 2014.
- [131] Guillaume Burnand and Yves Perriard. Very-High-Speed Miniaturized Permanent Magnet Motors: Modeling and Experimental Validation. In *2019 IEEE Energy Conversion Congress and Exposition (ECCE)*, pages 5251–5257, Baltimore, MD, USA, September 2019. IEEE.
- [132] Duane C. Hanselman. *Brushless permanent magnet motor design*. The Writers' Collective, Cranston, R.I, 2nd edition, 2003.
- [133] Jean Chatelain. *Traité d'Electricité: Machines Electriques*, volume X. Presses Polytechniques et Universitaires Romandes, Lausanne, 2ème edition, 1983.
- [134] Jacek F Gieras, Zbigniew J Piech, and Bronislaw Tomczuk. *Linear Synchronous Motors: Transportation and Automation Systems*. CRC Press, Boca Raton, 2nd edition, 2012. OCLC: 992448755.
- [135] Guillaume Burnand, Douglas Martins Araujo, and Yves Perriard. Optimization of shape and topology for slotless windings in BLDC machines. In *21st International Conference on Electrical Machines and Systems (ICEMS)*, pages 1–6. IEEE, October 2018.
- [136] Adrien Thabuis, Xiaoto Ren, Guillaume Burnand, and Yves Perriard. Density-Based Topology Optimization of Conductor Paths for Windings in Slotted Electrical Machines. In *22nd International Conference on Electrical Machines and Systems (ICEMS)*, pages 1–6. IEEE, August 2019.
- [137] Alexander Apelblat. Integral representation of Kelvin functions and their derivatives with respect to the order. *ZAMP Zeitschrift für angewandte Mathematik und Physik*, 42(5):708–714, September 1991.
- [138] Milton Abramowitz and Irene A Stegun. *Handbook of mathematical functions with formulas, graphs, and mathematical tables*. Dover Publications, New York, 1972.



# Curriculum Vitae

**Guillaume BURNAND**

Born on March 27, 1989

Swiss citizen

guillaume.burnand@gmail.com

## Education and qualifications

2016 - 2020	PhD in Microengineering at the Integrated Actuators Laboratory (LAI), École Polytechnique Fédérale de Lausanne, Switzerland
2014 - 2016	Master of Science in Electrical and Electronic Engineering, École Polytechnique Fédérale de Lausanne, Switzerland
2013 - 2014	HES-EPF pathway École Polytechnique Fédérale de Lausanne, Switzerland
2010 - 2013	Bachelor of Science in Electrical Engineering, Haute École d'Ingénierie et de Gestion du Canton de Vaud, Switzerland
2005 - 2009	Apprenticeship of electrician and mechanics, Bobst SA, Switzerland

## Patent

1. **Guillaume Burnand**, Douglas Martins Araujo, and Yves Perriard, Electrical machines winding. CH20180001134, 2018.

### Publications

#### Journal papers

1. **Guillaume Burnand**, Adrien Thabius, Douglas Martins Araujo and Yves Perriard. Novel optimized shape and topology for slotless windings in BLDC machines. In *IEEE Transactions on Industry Applications*, 2019.
2. Submitted: **Guillaume Burnand**, Camilo Hernandez Mejia and Yves Perriard. Small-Scale Very-High-Speed Slotless Permanent Magnet Motors: Part I - Modeling and Experimental Validation. In *IEEE Transactions on Industry Applications*.
3. Submitted: **Guillaume Burnand** and Yves Perriard. Small-Scale Very-High-Speed Slotless Permanent Magnet Motors: Part II - Design and Optimization. In *IEEE Transactions on Industry Applications*.

#### Conference papers

1. **Guillaume Burnand** and Yves Perriard. Very-High-Speed Miniaturized Permanent Magnet Motors: Modeling and Experimental Validation. In *2019 IEEE Energy Conversion Congress and Exposition (ECCE)*, pages 1–7. IEEE, October 2019.
2. **Guillaume Burnand** and Yves Perriard. Very-High-Speed Miniaturized Permanent Magnet Motors: Design and Optimization. In *2019 IEEE Energy Conversion Congress and Exposition (ECCE)*, pages 1–7. IEEE, October 2019.
3. Adrien Thabius, Xiaotao Ren, **Guillaume Burnand** and Yves Perriard. Density-Based Topology Optimization of Conductor Paths for Windings in Slotted Electrical Machines. In *22nd International Conference on Electrical Machines and Systems (ICEMS)*, pages 1–6. IEEE, August 2019.
4. **Guillaume Burnand**, Douglas Martins Araujo, and Yves Perriard. Optimization of shape and topology for slotless windings in BLDC machines. In *21st International Conference on Electrical Machines and Systems (ICEMS)*, pages 1–6. IEEE, October 2018.
5. **Guillaume Burnand**, Douglas Martins Araujo, Christian Koechli, and Yves Perriard. Validation by measurements of a windage losses model for very-high-speed machines. In *20th International Conference on Electrical Machines and Systems (ICEMS)*, pages 1–4. IEEE, August 2017.
6. **Guillaume Burnand**, Douglas Martins Araujo, and Yves Perriard. Very-high-speed permanent magnet motors: Mechanical rotor stresses analytical model. In *IEEE International Electric Machines and Drives Conference (IEMDC)*, pages 1–7. IEEE, May 2017.

---